Ultrafast Carrier Dynamics in $CsPbBr_3$ Perovskite Nanocubes and Nanoplatelets: Time-resolved TeraHertz Spectroscopy Study

A Dissertation

submitted in partial fulfilment of the requirements

for the degree of

Doctor of Philosophy

by

Yettapu Gurivireddy

(ID: 20123158)

THz Spectroscopy Lab

Department of Chemistry

Indian Institute of Science Education and Research-Pune

2019

IISER PUNE

भारतीय विज्ञान शिक्षा एवं अनुसंधान संस्थान, पुणे
INDIAN INSTITUTE OF SCIENCE EDUCATION AND RESEARCH (IISER) PUNE
(An Autonomous Institution of Ministry of Human Resource Development, Govt. of India)
Dr. Homi Bhabha Road, Pune - 411008.

DECLARATION

I declare that this written submission represents my ideas in my own words and wherever other's ideas have been included; I have adequately cited and referenced the original sources. I also declare that I have adhered to all principles of academic honesty and integrity and have not misrepresented or fabricated or falsified any idea / data / fact / source in my submission. I understand that violation of the above will cause for disciplinary action by the Institute and can also evoke penal action from the sources which have thus not been properly cited or from whom proper permission has not been taken when needed.

Mr. Yettapu Gurivireddy

Date: 17th January 2019

(ID: 20123158)

भारतीय विज्ञान शिक्षा एवं अनुसंधान संस्थान, पुणे
INDIAN INSTITUTE OF SCIENCE EDUCATION AND RESEARCH (IISER) PUNE
(An Autonomous Institution of Ministry of Human Resource Development, Govt. of India)
Dr. Homi Bhabha Road, Pune - 411008.

Dr. Pankaj Mandal
Associate Professor
Department of Chemistry,
IISER Pune

CERTIFICATE

Certified that the work incorporated in the thesis entitled "***Ultrafast Carrier Dynamics in $CsPbBr_3$ Perovskite Nanocubes and Nanoplatelets: Time-resolved TeraHertz Spectroscopy Study***" submitted by **Mr. Yettapu Gurivireddy** was carried out by the candidate, under my supervision. The work presented here or any part of it has not been included in any other thesis submitted previously for the award of any degree or diploma from any other university or institution.

Dr. Pankaj Mandal

Date: 17th January 2019

(Research Supervisor)

Acknowledgements

First and foremost I would like to acknowledge my supervisor Dr. Pankaj Mandal for his guidance and backing me throughout my Ph. D. The patience acquired from him made me align the THz setup several times without compromising the quality of the signal.

I am also thankful to my research advisory committee members Dr. Sayan Bagchi and Dr. Angshuman Nag for their valuable suggestions during annual RAC meetings. I wish to thank former director Prof. K. N. Ganesh and present director Prof. Jayant B. Udgaonkar and Prof. M. Jayakannan, Chair, department of chemistry, for supporting us in various situations.

I would also like to thank my labmates Sohini, Avinash, Sneha, Shabnum, Aman, Rapti and Mayank for their direct and indirect contribution and support in fulfilment of my Ph. D. My special thanks first goes to Sohini, without her help in alignment of the optics, THz generation, and detection wouldn’t have been possible and later goes to Avinash who helped me a lot during alignment and data measurement. Of course, I am thankful to Sneha and Shabnum for their well-timed help in correcting my thesis.

I would like to acknowledge my collaborators from Dr. Angshuman Nag group, Abhishek, Vikash, Wasim, Jagadeesh and from Dr. Prasenjit Ghosh group, Debnath. Without their collaboration and discussion, the work embedded and ideas implemented in the thesis could not have become reality.

I am also thankful to IISER-Pune for providing the state of art facilities and UGC for fellowship. Playing cricket with Nanosoldiers team and rarely winning matches and celebrating “Ugadi” with Telugu fraternity along with our guests, gives a memory which needs to be cherished. I am extremely thankful to my M. Sc. batchmates, University of Hyderabad, and my family members for helping me unconditionally during my Ph. D.

Last but not least, I wish to thank all the people who helped and supported me without my knowledge directly or indirectly in fulfilment of my Ph. D.

Synopsis

The main objective of my thesis is to generate and detect ultra-short THz radiation, whose spectral bandwidth is greater than 15 THz and use it as spectroscopic tool to probe phonon resonances and charge carrier dynamics in ultrafast timescales (picosecond to sub-picosecond), in all inorganic $CsPbBr_3$ perovskite nanocubes, which are in weak confinement regime and nanoplatelets, which are in strong confinement regime. In time-domain THz spectroscopy, THz electric field is measured and its Fourier transformation gives amplitude and phase, unlike conventional methods where intensity is measured. From amplitude and phase, one can obtain complex conductivity, without any electrical connection to nanocrystals (NCs). Since THz probe energies are in milli-electron-Volts (meVs) and timescales are in the picosecond (ps), one can easily detect phonon (lattice vibrations) resonances and their variance with confinement. One can also probe carrier dynamics in NCs, where charge carrier recombination takes place in picosecond timescales.

Chapter 1. ***Introduction to Perovskite Nanocrystals and THz spectroscopy***

In this chapter, we briefly discussed the importance of THz spectroscopy, especially its capability in distinguishing various photogenerated species. We further discuss the quantum confinement in semiconductor NCs, the limitations of semiconductor NCs for their use in real devices, the importance of organic-inorganic lead halide perovskites, photoluminescence properties of all-inorganic $CsPbX_3$ NCs, defect tolerance that is intrinsic to lead-halide perovskites, various recombination mechanisms occurring in semiconductor NCs, and two-photon absorption in semiconductor NCs.

Chapter 2. ***Experimental Procedure and Data Analysis***

In this chapter, we described how we have built the time-domain and time-resolved THz spectrophotometers. We use air plasma as the ultra-broadband THz generating medium and detect the pulsed THz light using air-biased coherent detection (ABCD) scheme. The THz spectral bandwidth obtained in our laboratory is often >15 THz. Further, we reported the analysis procedure used in this thesis to obtain optical constants, such as the complex refractive index, complex dielectric constant and complex conductivity. A brief discussion on effective medium theories is also presented, which are required to get the response of pure NCs from the response of NC solutions. Further, we briefly discussed appropriate conductivity models, which are required to fit the transient conductivity spectra thereby one can obtain the carrier density and mobility.

Chapter 3. ***Terahertz Conductivity within Colloidal $CsPbBr_3$ Perovskite Nanocrystals***

Colloidal $CsPbX_3$ NCs are known to exhibit exceptional photophysical properties such as high photoluminescence (PL) quantum yield (QY), low threshold fluence lasing capability, reduced PL blinking and so on. The mechanism behind such amazing properties is still lacking and understanding them in detail is of paramount importance for their better utilization in real devices. In this chapter, we studied the nature of the phonon modes and the charge carrier dynamics in colloidal $CsPbBr_3$ NCs. The origin of phonon mode, which occurs at 3.4 THz, was assigned from DFT calculations and major contribution comes from the anti-symmetric apical Pb-Br stretching mode and one in-plane Br-Pb-Br bending mode. In solution processed tiny NCs, a large density of surface defects is expected because of the large surface to volume ratio. Thus, high fluorescence QY is counterintuitive. We establish a 3-fold free carrier recombination mechanism, namely nonradiative Auger, bimolecular electron-hole recombination, and inefficient trap-assisted recombination. Our results confirm a negligible influence of surface defects, which in turn results in high charge carrier mobilities and longer diffusion lengths. From initial decay dynamics, the exciton dissociation time constant found to be 5-6 ps. Strong exciton-phonon coupling with softer modes probably redshift the phonon resonance.

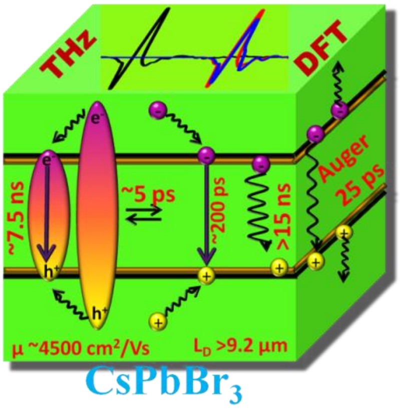

Figure 1. Schematic showing various recombination channels present in colloidal $CsPbBr_3$ NCs. Inefficient trap-assisted recombination results in high charge carrier mobilities and diffusion lengths.

Publication from this chapter:

Yettapu, G. R.; Talukdar, D.; Debnath T.; Sarkar, S.; Swarnkar, A.; Nag, A.;* Ghosh, P.;* Mandal, P.* THz conductivity within colloidal $CsPbBr_3$ perovskite nanocrystals: Remarkably high carrier mobilities and large diffusion lengths. *Nano Lett.* **2016**, *16*, 4838-4848.

Chapter 4. *Carrier Dynamics in $CsPbBr_3$ Nanocrystal Film: Comparison between Single and Two-Photon Pumping*

In this chapter, we studied the charge carrier dynamics in $CsPbBr_3$ nanocrystal film. Most optoelectronic devices such as a field-effect transistor, photoresistor, light emitting diodes, and photovoltaics use film as an active layer. In the film, carriers may undergo scattering from grain boundaries and hence transport properties can be altered. In the case of the film, phonon peak is slightly red-shifted compared to the solution due to less stiffening of the bonds. The increased size of cubes in the film decreases surface to volume ratio and reduces the stiffening of the bonds. The carrier dynamics under single and two-photon absorption vary significantly due to the occupancy of different initial excited states under one and two-photon excitation. We observe the evidence of large to intermediate polaron formation which reduces the mobilities and diffusion lengths more than an order of magnitude compared to those observed for single nanocrystal probed in the colloidal dispersion.

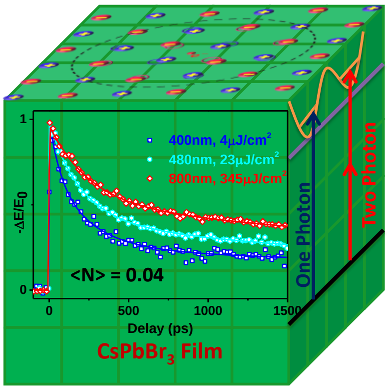

Figure 2. Schematic showing THz transients are different under single and two-photon absorption in $CsPbBr_3$ NCs film. Large to intermediate polaron limits charge carrier mobilities and diffusion lengths.

Publication from this chapter:

<u>Yettapu, G. R.</u>; Ravi, V.K.; Nag, A.; Mandal, P.* Carrier dynamics in $CsPbBr_3$ perovskite film: comparison between single and two-photon pumping. (*Manuscript under preparation*)

Chapter 5. *Ultrafast Carrier Dynamics in Quasi-Two-Dimensional $CsPbBr_3$ Nanoplatelets*

In this chapter, we studied quantum confinement effects on carrier dynamics in $CsPbBr_3$ nanoplatelets (NPLs). In confinement regime, one would expect the carrier dynamics to be faster going from five monolayers (5-MLs) to three monolayers (3-MLs) NPLs, where the probability of the overlap between electron and hole wave functions increases. Inspired by the previous reports, where the authors claimed that the exciton dynamics are independent of the extent of confinement, we studied carrier dynamics with TRTS in picosecond to nanosecond temporal resolution range. Our study clearly shows that photogenerated species being excitons, most (greater than 80 %) carrier population decays within 300 ps. The THz absorption spectrum has an extra phonon peak at ~ 4.2 THz which is independent of the confinement. We attribute this feature to in-plane lattice vibrations. The phonon peak, which redshifts with the extent of confinement, is due to lattice expansion and we attribute it to the out-of-plane lattice vibrations. Strong confinement curtails the mobilities and diffusion lengths; however, these properties can be modulated with stacking several NPLs.

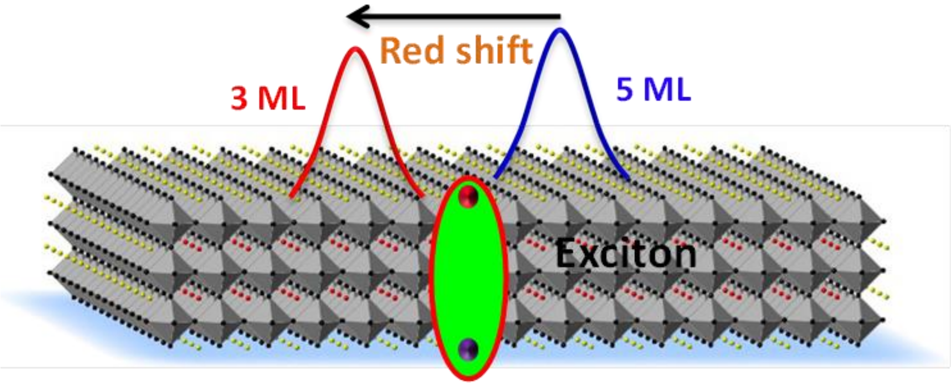

Figure 3. Schematic showing phonon resonance redshifted going from 5-ML to 3-ML. The THz kinetics are very fast in NPLs compared to that in nanocubes because of the quantum confinement effect.

Publication from this chapter:

Yettapu, G. R.; Mir, W.; Rao, M. J.; Nag, A; Mandal, P.* Effect of confinement on carrier dynamics in $CsPbBr_3$ perovskite nanoplatelets. (*Manuscript under preparation*)

Contents

Glossary of Acronyms

ABCD : Air biased coherent detection

ATC : Asymmetric transient current

BZ : Brillouin zone

CBM : Conduction band minimum

$CsPbBr_3$: Cesium lead bromide

DFPT : Density functional perturbation theory

DFT : Density functional theory

DS : Drude-Smith

EMA/T : Effective medium approach/theory

EO : Electro-optic

fs : femtosecond

FWM : Four wave mixing

FWHM : Full width at half maximum

GGA : Generalized gradient approximation

HDPE : High density polyethylene

HMN : 2,2,4,4,6,8,8-heptamethyl nonane

HOIP : Hybrid organic inorganic perovskite

HRTEM : High resolution Transmission Electron Microscope

HVM : High voltage modulator

IR : Infrared

KE : Kinetic energy

LASER : Light Amplification by Spontaneous Emission of Radiation

LED : Light emitting diode

LS : Light source

meV : milli electron volt

ML	: Monolayer
mm	: millimetre
ms	: millisecond
NC	: Nanocrystal
nm	: nanometre
NPL	: Nanoplatelet
ns	: nanosecond
OD	: Optical density
OPA	: Optical parametric amplifier
OPA (1PA)	: One photon absorption
OPTP	: Optical pump-THz probe
PBE	: Perdew-Burke-Ernzerhof
PC	: Photoconductivity
PL	: Photoluminescence
PMT	: Photomultiplier tube
PS	: Polystyrene
PSKT	: Perovskite
ps	: picosecond
QY	: Quantum yield
SEM	: Scanning electron microscope
SHG	: Second harmonic generation
SOI	: Spin orbit interaction
SOC	: Spin orbit coupling
TAS	: Transient absorption spectroscopy
TDS	: Time Domain Spectroscopy
TFISH	: Terahertz field induced second harmonic
THz	: Terahertz

TOF	: Time of flight
TPA (2PA)	: Two photon absorption
TPX	: polymethyl pentene
TRMC	: Time resolved microwave conductivity
TR-OKE	: Time-resolved optical Kerr effect
TRPL	: Time Resolved Photoluminescence
TRTS	: Time Resolved THz Spectroscopy
UV-vis	: Ultraviolet-visible
VBM	: Valence band maximum
vdW	: van der Waals
μm	: micrometre
μs	: microsecond

Chapter 1

Introduction to Perovskite Nanocrystals and Terahertz Spectroscopy

1.1 Perovskites and Organic-Inorganic Lead Halide Perovskites:

Perovskite is the calcium titanium oxide ($CaTiO_3$) mineral named after Russian mineralogist Lev Perovski. Perovskites have general stoichiometry $ABX_{3-x}Y_x$, where A and B are respectively mono and divalent cations (A: $CH_3NH_3^+$, $HC(NH_2)_2^+$, Cs^+ and B: Pb^{2+}), and X and Y are halide anions (X, Y: Cl^-, Br^- and I^-). The B cation forms octahedron, BX_6 configuration, and A cation is coordinated by 12 neighbouring X atoms and forms cuboctahedron. Perovskite materials based photovoltaics have been explored as an alternative to Si-based solar cells due to the ease of synthesis and cost-effectiveness. The first photovoltaic cell based on organic-inorganic metal halide perovskite as sensitizer was first reported in 2009 by Kojima *et al.* with a power conversion efficiency (PCE) of 3.8%.[1] Within a short span of time the efficiency has been increased to >22.7%.[2] Further, it was demonstrated that by using tandem architectures, concentrator configuration, and hot carrier extraction, the efficiency can exceed Shockley-Queisser limit.[3-6] The success of the perovskite photovoltaics has been attributed to strong absorption in the visible region, low exciton binding energies, low trap densities and better transport properties (high mobilities and long diffusion lengths).[7-18] Further understanding as about the carrier recombination, fundamental upper limits to charge carrier mobilities, accurate determination of photoexcited species (excitons vs. free carriers vs. polarons) and correlation with optoelectronic, photovoltaic applications is evolving. Various spectroscopic techniques, which include transient photoluminescence spectroscopy (TRPL), transient absorption spectroscopy (TAS), THz and microwave conductivity spectroscopy and optical Kerr effect spectroscopy (OKE), are being used to study the fundamental physics behind their outstanding performances.[11,15,19-24] However, this material greatly suffers from the degradation in environmental humidity and temperature conditions. Organic-inorganic metal halide perovskites under these conditions dissociate to volatile gases and also form hydrates.[25-27]

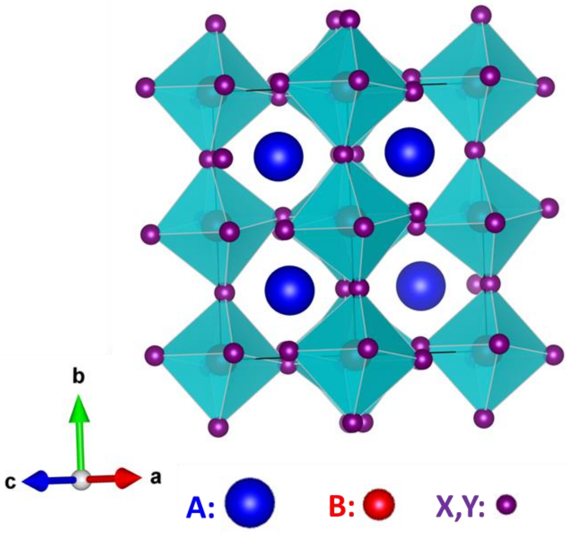

Figure 1.1: Crystal structure of perovskite of generic formula ABX_3, where mostly A is $CH_3NH_3^+$, $HC(NH_2)_2^+$ and Cs^+ , B is Pb^{2+}, Sn^{2+}, and X, Y are halide (Cl^-, Br^- and I^-) ions.

The possible solution to this stability problem was obtained by replacing the volatile organic cation ($CH_3NH_3^+$, $HC(NH_2)_2^+$) with an inorganic cation such as Cs^+.[28-30] Although the stability issue was partly solved, these new class of perovskites, especially α-$CsPbI_3$ that has suitable band gap for photovoltaic applications, are highly temperature dependent and easily undergo phase transitions.[31] This limits their potential application in photovoltaics. However, $CsPbBr_3$, not quite suitable to get higher PCE due to undesirable bandgap,[31-33] is relatively stable at room temperature and exhibits exceptional photophysical properties as well as optoelectronic applications as discussed below.

1.2 All-Inorganic Lead Halide Perovskite Nanocrystals:

The bulk all-inorganic caesium lead halide ($CsPbX_3$) perovskites were synthesized in the early 1890s but their crystal structure and photoconductivity were measured later 1950s by Muller.[34] All-inorganic caesium lead halide colloidal NCs were first synthesized by Kovalenko and co-workers. These NCs exhibit PLQY as high as 90%, PL tunability across the entire visible range and reduced emission bandwidth (12-42 nm) by composition modulation, as shown in Figure 1.2.[35] Although the bandgap can be tuned in the quantum confinement regime by varying size, the precise variation across the entire visible range can be achieved by modulation of halide composition.[35-38] These exceptional photophysical properties allow researchers to demonstrate various optoelectronic applications such as wavelength tunable phosphors, high colour purity LEDs, low-threshold lasers, single photon sources and high energy radiation detectors.[35,39-45] Further, reduced fluorescence blinking, tenuous self-absorption and Förster resonance energy transfer have been revealed in these materials.[46,47] One would anticipate that low trap density is responsible for the above-mentioned properties. However, this is counter-intuitive in case of small NCs. One would expect a high density of trap states due to the high surface to volume ratio. Traps or defects are detrimental for above-mentioned PL based optoelectronic as well as photovoltaic applications. Recently, TRPL and TRTS studies were employed to probe the excited states and showed that the primary recombination mechanisms involved in these NCs are monomolecular trap-assisted, bi-molecular and tri-molecular Auger recombination, see Figure 1.6 in section 1.5. These studies show that defects states lie near or within the CB and VB and are inefficient in nature i.e. defect tolerant (see section below).[48,49] Generally for regular semiconductor NCs the traps lie deep in the band gap. Simple post-synthetic modification of the surface of these NCs with thiocyanate, which removes excess lead atoms, yields near unity PLQY. This indicates that mostly shallow trap states are present in these NCs.[50]

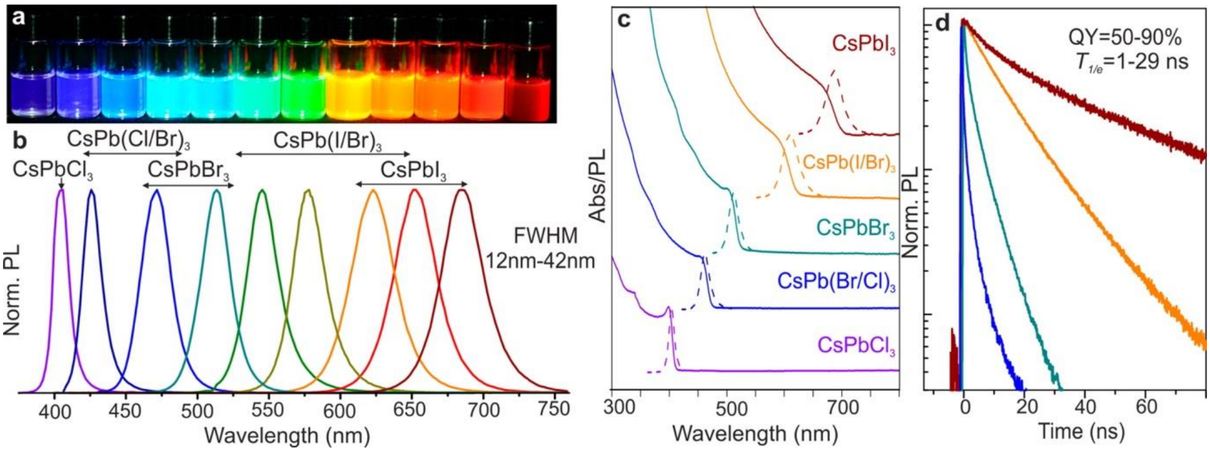

Figure 1.2: Images of colloidal $CsPbBr_3$ NCs dispersed in toluene under UV lamp a), their PL spectra across the visible range with narrow full width at half maximum (FWHM) b), absorption c) and time-resolved PL decays d). Adapted from ref 35. © 2015, American Chemical Society.

1.3 Semiconductor Nanocrystals (Quantum dots) and Quantum Confinement:

Semiconductor nanocrystalline materials possess an intermediate energy band gap (E_g) compared with molecular clusters and bulk material. The band gap can be tuned by varying the size (r) of nanocrystal (NC), when the size is below the exciton Bohr radius and is inversely related to the size of the NC. This regime is called quantum confinement regime, where the excited carriers feel the confinement due to the physical boundary of NCs. As a result of confinement, in addition to the bandgap variation, the continuum electronic energy states, present in bulk material, also become discrete as shown in Figure 1.3.A. Further, density of states vary from bulk semiconductor to quantum dot as shown in Figure 1.3.B .[51] This fascinating phenomenon allowed these NCs to be used in various applications such as field effect transistors, light emitting diodes, solar cells and so on.[52-54]

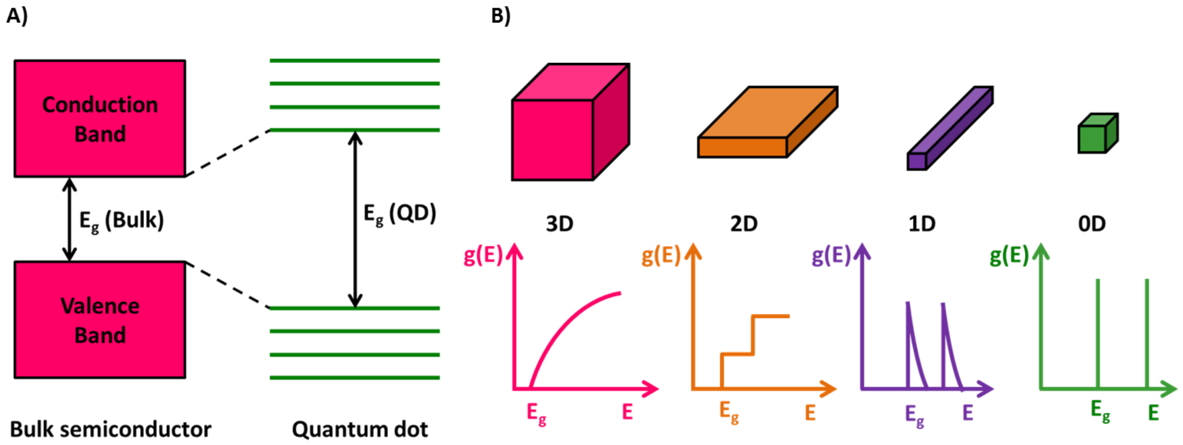

Figure 1.3: A) Schematic representation of band diagram for bulk semiconductor and a quantum dot. The bulk semiconductor has closely spaced energy levels whereas quantum dot has discrete energy levels. B) The generic shape of the density of states for various dimensional semiconducting nanostructures.

However, having possessed high surface to volume ratio, these NCs contain relatively more atoms on the surface which are not coordinated. The energy of the non-bonding orbitals, also called dangling bonds, from these undercoordinated surface atoms, lie within the bandgap and act as traps for charge carriers (see Figure 1.4). These traps are known to act as recombination centers, where recombination takes place non-radiatively and are detrimental for the above-mentioned applications.[54,55] Complete passivation of the surface is difficult due to the bulkiness and/or inherent defects present in the surface ligands.[56-58] One way to mitigate this problem is by passivating the surface of the NC, called core, with a shell of higher bandgap material.[59,60] However, shell hinders the extraction and transportation of charge carriers generated from the core and thereby reducing their maximum utility in optoelectronics.

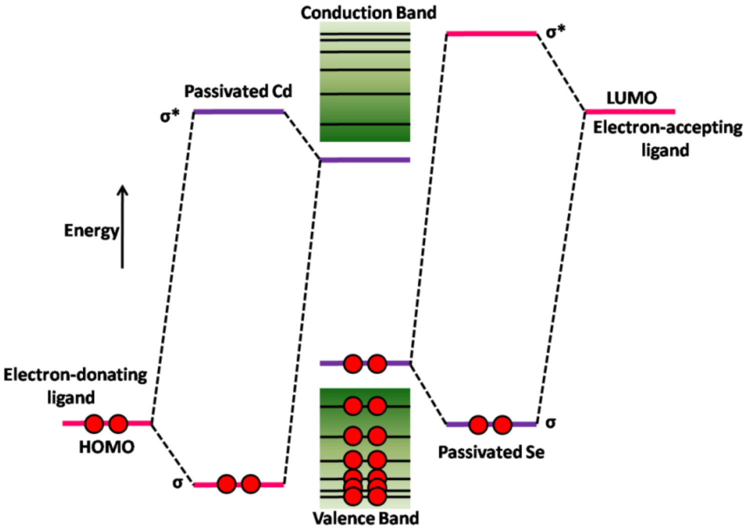

Figure 1.4: Simplified molecular orbital diagram of typical CdSe quantum dot. Energies of electronic states (Purple lines) from under-coordinate Cd and Se surface atoms lie in between valence band maximum and conduction band minimum of QD. These electronic states act as traps for electrons and holes and hamper the efficiency of QD-based devices. When surface atoms bond with surface ligands they form molecular orbitals σ and σ*. The strong interaction between them pushes these molecular orbitals outside the bandgap and makes the QD trap-free. Adapted from the ref 56. © 2016, Springer Nature.

1.4 Electronic Structure and Origin of Defect Tolerance in Perovskites:

Nanocrystals, whose emission properties are not affected by defects, though their surface states are not completely passivated, can be called as defect tolerant materials. The origin of the defect tolerance comes purely from their inherent electronic band structure. The schematic representations of molecular orbital diagrams for II-VI semiconductors and organic or inorganic lead halide perovskite are shown in Figure 1.5. The valence band maximum (VBM) in perovskites is constituted by hybridisation of Pb (6s) and X (np) orbitals and main contribution is from X np orbitals and anti-bonding in nature, whereas conduction band minimum (CBM) is formed by hybridisation of Pb (6p) and X (np) orbitals and main contribution is from Pb (6s) orbitals and antibonding in nature. Although the orbital contribution to CBM is debated in the literature, some reports based on first principle calculations suggested CBM is formed exclusively from Pb (6p) orbitals.[61] Few reports based on DFT calculations along with experimental reports, such as cyclic voltammetry study, show that X (np) orbital contribution to the CBM is small and systematic across the halide composition but its contribution cannot be neglected.[62-64] Lead (Pb) being heavy, relativistic spin-orbit interactions increases the bandwidth of CBM thereby making the vacancies/defects states resonant with CB, whereas antibonding nature of VBM makes vacancies/defects to be resonant with VB.[64] Generally, surface states are nonbonding in nature and arise in between VB and CB, which are bonding and antibonding in nature, respectively. Since VBM and CBM is formed from the antibonding orbitals, it is very less likely that nonbonding orbitals are formed within the band gap, instead, they are lying close to or resonant with CBM/VBM.[64-66] This lack of bonding-antibonding interactions between conduction and valence bands makes these perovskites defect tolerant and maintain good electronic quality despite the presence of defects.[66] In contrast, in conventional II-VI or III-VI semiconductors the VBM is formed from bonding orbitals and CBM is formed from antibonding orbitals. Due to this kind of electronic structure, these semiconductors form shallow or deep traps within the bandgap that arises from dangling (broken) bonds and cation or anion vacancies. Although A-site cation acts as the counterion for charge balance and contributes less to the frontier orbitals that constitute the bandgap, it greatly affects octahedral tilting thereby changes the band gap.[67] It was shown that as the cation size increases the tilting of octahedron decreases thereby increasing the metal p contribution at CBM. Greater metal contribution increases the spin-orbit coupling, which in turn reduces the band gap.[68,69] This was justified by recently synthesized $FAPbI_3$ NCs, (FA is larger cation compared with Cs, MA) where they could dismantle red wall and accessed emission in red and infra-red spectral region.[70]

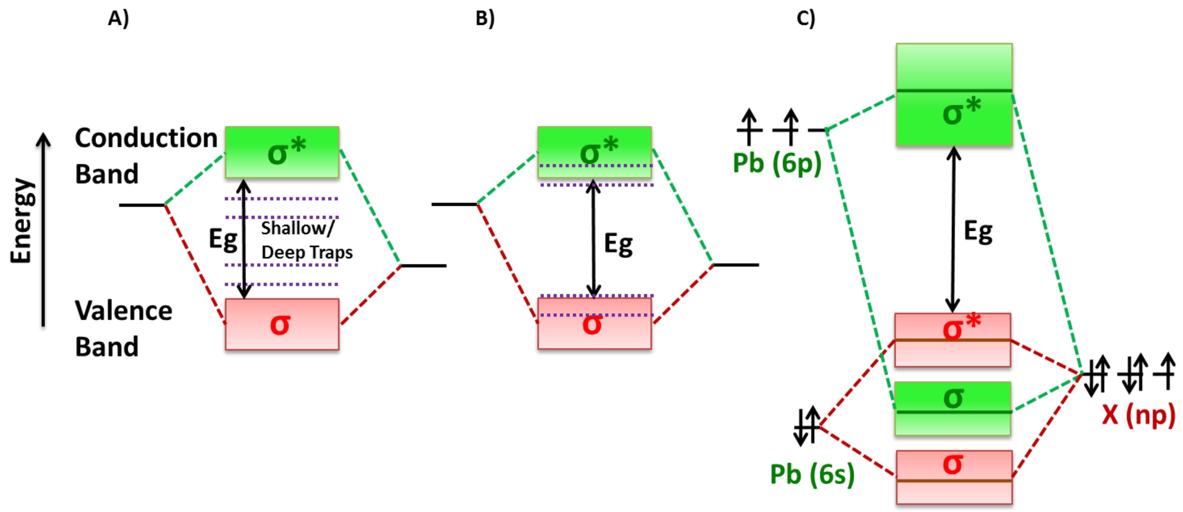

Figure 1.5: Comparison of the band diagrams for II-VI semiconductors A) and for Perovskite C). B) and A) show defect tolerant and intolerant nature, respectively. Figure C adapted from ref 64. © 2015, Materials Research Society.

1.5 Recombination Processes in NCs:

If the pump photon energy is greater than the bandgap (E_g), it creates charge carriers such as hot electrons and holes, excitons (bound electron-hole pairs), free electrons and free holes and so on. These excited charge carriers undergo different recombination processes and reach to the ground state.[20] There are three primary recombination mechanisms reported in the literature, as shown in Figure 1.6. They are 1. Monomolecular recombination, where the single carrier (either electron or hole) participates in recombination and it is mostly nonradiative and carriers are immobilized when they get trapped in defect states. The trap-assisted recombination is fluence independent i.e.$-\frac{dn}{dt} = k_1 n$, where k_1 is mono molecular rate constant and n is the carrier density. 2. In bi-molecular recombination, two carriers participate in recombination. The recombination rate depends on the overlap of electron wave function in the conduction band and the hole wave function in the valence band. This process is fluence dependent i.e. $-\frac{dn}{dt} = k_2 n^2$, where k_2 is bi-molecular rate constant and 2 represents two particles, an electron and a hole. 3. Tri-molecular recombination, also called Auger recombination, a three body collision process, where electron and hole recombine and the energy is simultaneously transferred to the third particle (either electron or hole) and overall energy is conserved.[71] This process is very strongly fluence dependent. i.e.$-\frac{dn}{dt} = k_3 n^3$, where k_3 is the tri-molecular rate constant. Here the three particles involved in the recombination process are an electron, a hole and the third particle may be either an electron or a hole. The overall recombination rate, which involves above three processes, can be written as follows

$$-\frac{dn}{dt} = k_1 n + k_2 n^2 + k_3 n^3 \qquad (1.1)$$

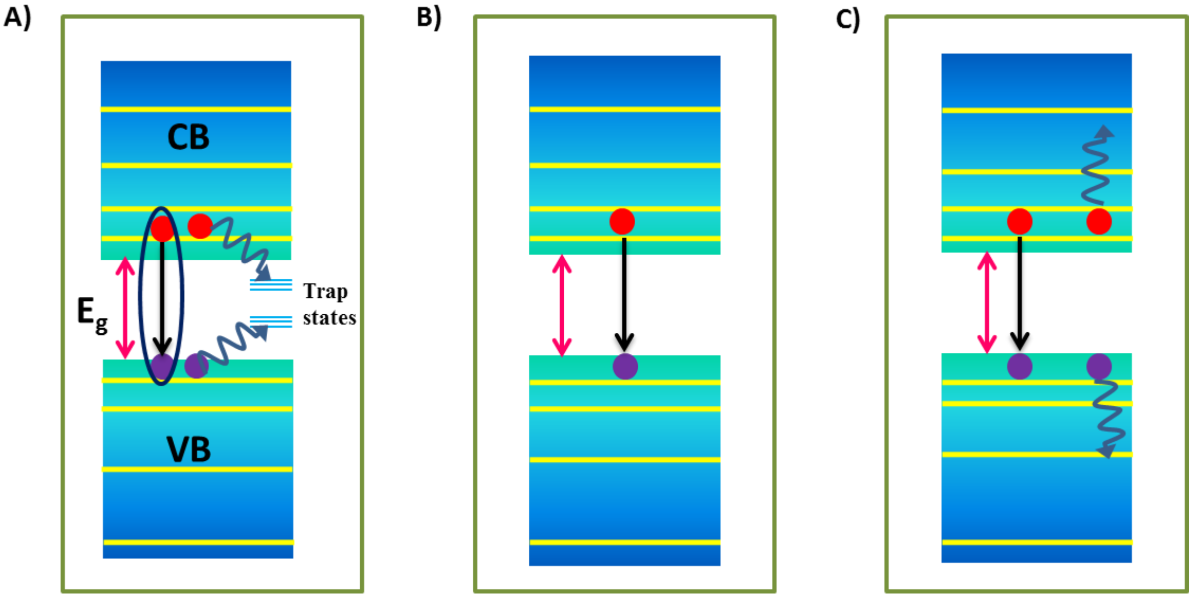

Figure 1.6: Schematic of recombination processes occurring in semiconductor NCs A) Mono molecular (exciton or trap-assisted) recombination B) Bi-molecular recombination C) Tri-molecular (Auger) recombination

1.6 Two-Photon absorption in NCs:

In the Two-Photon absorption (TPA) process, shown in Figure 1.7, a charge carrier makes the transition between the valence band to conduction band through simultaneous absorption of two photons, given the single photon energy is less than the band gap of the semiconductor. TPA has certain advantages over one photon absorption (OPA). Two-photon absorption can be used to achieve high skin depth and high spatial resolution with little damage to the sample.[72] One also can fabricate efficient frequency up-converted lasers, where phase-matching conditions are relaxed.[73]

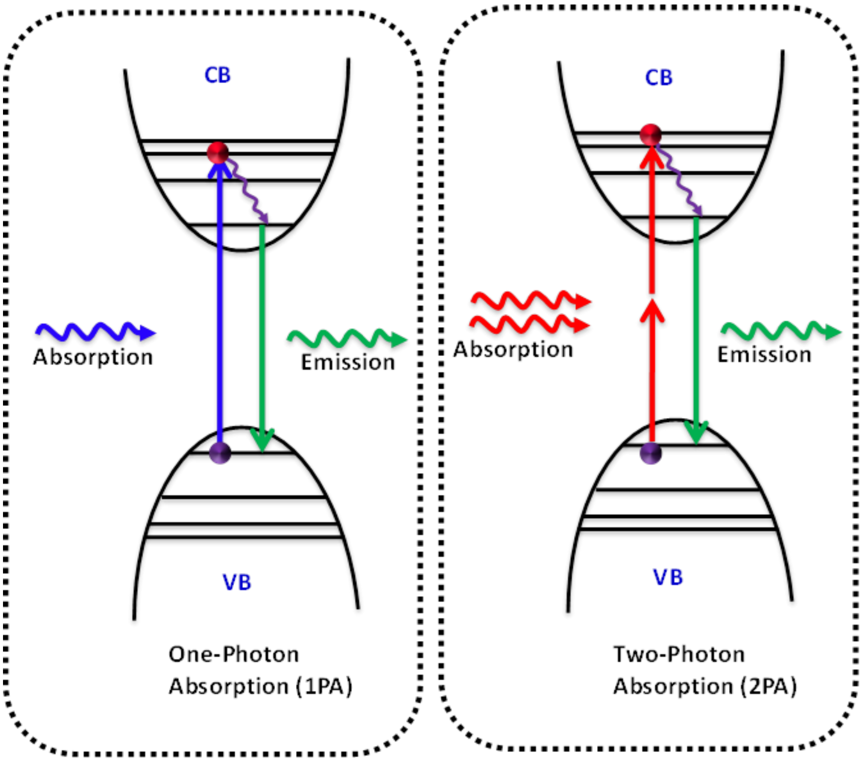

Figure 1.7. Schematic of one and two-photon absorptions processes in semiconducting NCs.

TPA is a nonlinear process and depends on the square of the intensity of the light. The attenuation of light through the sample of thickness l, under no linear absorption, can be written as[74]

$$\frac{-dI}{dl} = \beta I^2 \qquad (1.2)$$

where β is the two-photon absorption coefficient. Integrating the above equation between right limits leads to the following expression for transmittance (T) for TPA,

$$T = \frac{I}{I_0} = \frac{1}{1 + \beta I_0 L} \qquad (1.3)$$

where I_0, and I are incident and transmitted intensities of the light, respectively, and L is the total pathlength. The β can be experimentally determined by measuring the incident and transmitted intensity through the sample of thickness L.

1.7 Terahertz Spectroscopy:

Terahertz (THz) radiation lies between microwave and infrared radiation in the electromagnetic spectrum. This has been referred to as the THz gap due to lack of sensitive generators and detectors. One THz is related to other units as

$$1 \text{ THz} = 10^{12} \text{ Hz} = 1 \text{ ps} = 300 \text{ μm} = 33.3 \text{ cm}^{-1} = 4.14 \text{ meV}$$

The low energy or frequencies of the THz photons enables the investigation of collective vibrational motions in the condensed phase, generally lower in energy than observed in the infrared region, and rotational or torsional motions in molecules, higher in energy than observed in microwave region.[75-77] The see-through nature of THz light to the packaging materials such as plastic, paper, leather and wood, enables non-destructive inspection of mail envelops at post offices and luggage at airports.[78] The non-invasive and non-ionising nature of THz has found potential applications in detection of explosives and illicit drugs,[78-81] biomolecules,[82-88] biomedicine,[89,90] pharmaceuticals and bio-imaging.[91-94] Most of these applications are based on table-top laser sources and use a photoconductive antenna and nonlinear optical processes for generation and detection of THz.[95-102] Also, THz spectroscopy has been used to study carrier dynamics and phonon resonances in various bulk and nanostructured semiconducting materials since carrier scattering times and phonon energies fall within the THz regime.[77,102-107]

With the development of ultrafast lasers (less than 35 fs duration) it is possible to generate a THz spectrum of bandwidth greater than 30 THz.[108] Unlike other spectroscopic techniques, which measure only intensity, THz spectroscopy measures THz electric field. Fourier transformation of the electric field results in amplitude and phase of each of spectral component that makes up the THz pulse. Amplitude ratios obtained from sample and reference enables one to measure the absorbance of the sample, whereas phase difference enables measurement of refractive index. Together one can obtain the complex dielectric function and complex conductivity, without the need for Kramers-Kronig relations.[77,107]

Understanding the nature of photogenerated charge carriers in semiconductor nanocrystals (NCs) is important because they provide the basis for many device applications. The continuous development in technologies mainly focuses to reduce the physical size of devices and hence use NCs as building blocks. The efficiency of any such device depends on the transport properties of charge carriers in these NCs. The transport mechanism in these NCs is short range and recombination of charge carriers occurs in picosecond to sub-picosecond timescale. Time-resolved THz spectroscopy has emerged as a new spectroscopic tool over the past decade, which uses contact-free and non-invasive THz probe. It is ideal for probing carrier evolution and transient conductivity in picosecond time resolution in these nanomaterials.[77,107]

1.8 Time-Resolved THz spectroscopy:

In pump-probe spectroscopy experiments, (see Figure 1.8), initially, the optical pulse (pump) with relatively higher intensity excites the sample and another pulse (probe) at certain delay (τ) measures the photoinduced changes, as a function of pump-probe delay. Although all-optical pump-probe experiments provide excellent time resolution, they only probe the carrier kinetics from the particular state. At longer wavelengths, free carrier absorption feature can be detected, but they cannot provide any information on transport properties. Further, other spectroscopic techniques such as time of flight or time-resolved microwave conductivity can measure transport properties but their temporal resolution is limited to the nanosecond.[109] The carrier mobilities obtained for the same material with different techniques vary hugely due to the inherent difficulties, such as connecting micro-meter sized wires to nanometer-sized particles, involved in these methods. On the contrary, TRTS does not use any such electrical contacts, can circumvent some of the difficulties, and can get consensus in mobilities and diffusion lengths. However, extraction of conductivity and analysis is not so trivial in this method.[23]

TRTS is a subset of pump-probe technique. It provides unique information which cannot be obtained from other spectroscopic techniques. TRTS is a non-contact technique measures transient photoconductivity with sub-picosecond temporal resolution.[77,102-104,107] In TRTS experiment, a pump pulse excites the sample above band gap and creates carriers, such as free electrons and holes, bound electron-hole pairs (excitons), trions, and polarons.[107,110-114] Subsequently, the THz probe pulse interacts with these charge carriers and their response is manifested in the conductivity and (dielectric) susceptibility spectrum. The nature of the response to the THz probe depends on the nature of the photogenerated carriers. The conductivity spectra for various photogenerated species are given in Figure 1.9. When the THz field interacts with free carriers, momentum gets transferred, so that carriers are accelerated and can travel long distances. Free carriers follow Drude conductivity i.e. the real part of the conductivity is maximum at zero (DC limit) frequency and the imaginary part is positive (see Figure 1.9 C). This is the typical signature of free carriers present in the system. Carriers can be localized due to backscattering from interfaces or due to defects.[114] In these cases, the real part of the conductivity increases with increasing THz frequency and the imaginary part is negative and decreases with increasing THz frequency[114,115] (Figure 1.9 D). If the photogenerated species are excitons, the THz response is very different. THz photons cannot resonantly interact with excitons because the intra-excitonic transition energy (10-100 meV) is much higher than the single THz photon energy (1 THz = 4 meV). Instead, it polarizes the exciton wave function which is manifested as real and spectrally flat susceptibility and zero imaginary susceptibility (real conductivity).[111] Further, TRTS provides information of scattering mechanisms which limit the charge carrier transport, such as electron-phonon scattering or impurity scattering.[116] Generally two kinds of experiments are carried out in TRTS. One is the pump scan, where a single point on THz waveform, mostly peak point due to signal strength, is measured after photoexcitation as a function of pump-probe delay, which gives an average response of the material. The second one is the probe scan, where the complete THz waveform is recorded at certain pump-probe delays. This experimental approach provides the frequency dependent conductivity.[77,94,102]

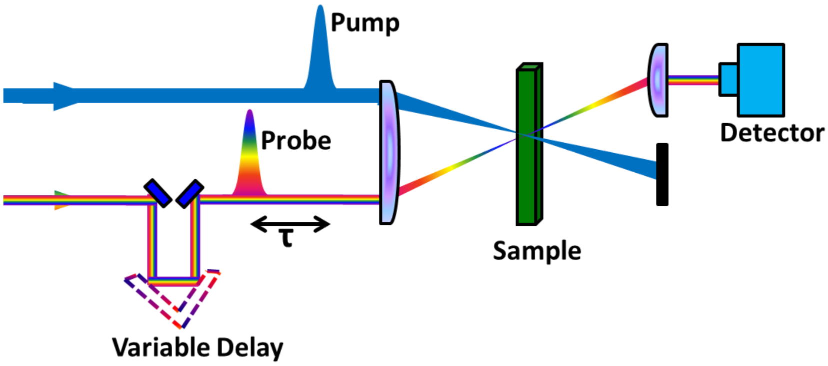

Figure 1.8: Schematic of pump-probe setup. Pump and probe wavelengths can vary from deep UV to far-infrared in the electromagnetic spectrum. The delay between them can be varied by a variable delay stage.

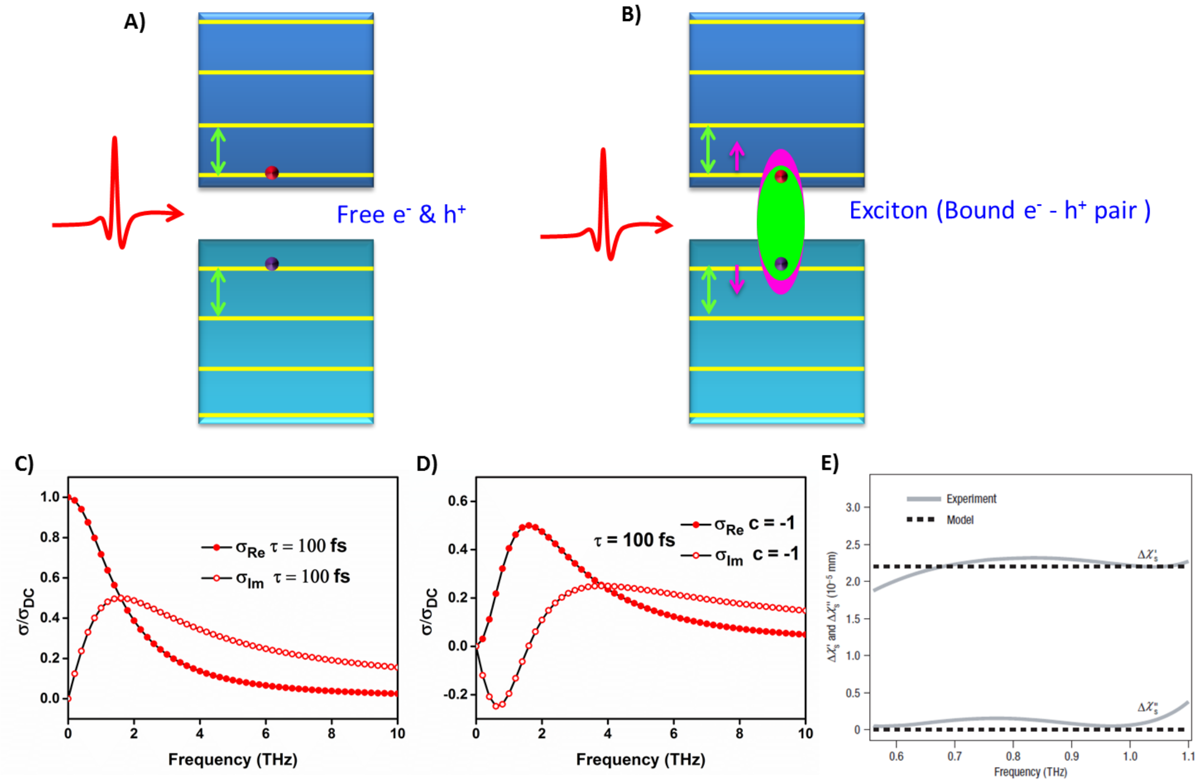

Figure 1.9: Photo-generated charge carriers above band edge. A) Free electrons and holes and B) Excitons. Conductivity spectra of free carriers C), localized carriers D), and Excitons E). Figure E adapted from the ref 111. © 2006, Springer Nature.

1.9 Scope and organization of the Thesis:

As mentioned above, all-inorganic $CsPbX_3$ perovskite NCs exhibit exceptional photophysical properties. All these properties are occurring from the excited state. Hence, one needs to understand how the charge carriers behave in an excited state. Herein, we use home-built time-domain and time-resolved THz spectroscopy as a tool to study the origin of phonons and charge carrier dynamics. From our time-resolved studies, we also determine the transport properties, such as mobilities and diffusion lengths. The thesis primarily focuses on studying carrier dynamics and phonon modes $CsPbBr_3$ NCs in colloidal dispersion and spin-cast films. Further, our study was extended to see the effects of quantum confinement on phonon resonance and the carrier dynamics in $CsPbBr_3$ nanoplatelets.

In chapter 2, I described how we have built time-domain and time-resolved THz spectrometers. We use air plasma as the ultra-broadband THz generating medium. Air-biased coherent detection (ABCD) scheme was used for coherent detection of the THz light. The THz spectral bandwidth obtained in our laboratory was >15 THz. Further, I reported the analysis procedure of the time-domain and time-resolved data. Also, the conductivity models used in our study have been discussed in detail.

In chapter 3, we studied the nature of the phonon modes and free carrier dynamics in colloidal $CsPbBr_3$ NCs. In solution processed tiny NCs, a large density of surface defects is expected because of the large surface to volume ratio. Thus, high fluorescence QY is counterintuitive. Our results confirm a negligible influence of surface defects, which in turn results in high charge carrier mobilities and longer diffusion lengths. The origin of phonon mode was assigned from DFT calculations and major contribution comes from the anti-symmetric apical Pb-Br stretching mode and one in-plane Br-Pb-Br bending mode. From initial decay dynamics, the exciton dissociation time constant found to be 5-6 ps. Strong exciton-phonon coupling with softer modes redshifts the phonon resonance.

In chapter 4, our study was extended to probe the carrier dynamics in the film. Most optoelectronic devices such as a field-effect transistor, photoresistor, and light emitting diodes and photovoltaic devices use film as an active layer. In the film, carriers undergo scattering from grain boundaries and hence transport properties can be altered. Phonon peak in the film is slightly redshifted due to less stiffening of the bonds. The increased size of cubes in film decreases surface to volume ratio and reduces the stiffening of the bonds. The carrier dynamics under single and two-photon absorption vary significantly due to the occupancy of different initial excited states. Large to intermediate polaron reduces the mobilities and diffusion lengths more than an order compared to the solution.

In chapter 5, we studied confinement effects on carrier dynamics in $CsPbBr_3$ NPLs. In the confinement regime, one would expect carrier dynamics to be faster when we go from five monolayers (5-MLs) to three monolayers (3-MLs), where the probability of the overlap between the electron and hole wave functions increases significantly. Surprised by the claims of the previous reports that the exciton dynamics is independent of the extent of confinement, we studied the carrier dynamics in NPLs with different thickness using TRTS in the picosecond to nanosecond temporal resolution range. Our study clearly showed that photogenerated species being excitons, a major (greater than 80 %) carrier population decays within 300 ps. The THz absorption spectrum has an extra phonon peak at ~ 4.2 THz that is independent of confinement. We attribute this phonon feature to the in-plane lattice vibrations. The phonon peak, which redshifts due to lattice expansion when we go from 5 ML to 3 ML, is attributed to out-of-plane lattice vibrations. Strong confinement curtails mobilities and diffusion lengths.

Finally, I conclude my work in chapter 6 and give the impression that TDS and TRTS can be successfully used to probe phonon resonances and charge carrier dynamics in these all-inorganic $CsPbBr_3$ perovskite nanocubes and nanoplatelets. The inefficient trap-assisted recombination makes the cubic NCs more suitable for various optoelectronic devices. Although mobilities and diffusion lengths are reduced in film, the values are on par with various other perovskites, indicates the NC film can be used as an active layer in photovoltaic applications. By taking the advantage of fast recombination, one can use $CsPbBr_3$ nanoplatelets in light emitting applications.

1.10 References

(1) Kojima, A.; Teshima, K.; Shirai, Y.; Miyasaka, T. *J. Am. Chem. Soc.* **2009**, *131*, 6050.
(2) Chart, N. E. *https://www.nrel.gov/pv/assets/images/efficiency-chart.png* **2018**.
(3) Shockley, W.; Queisser, H. J. *J. Appl. Phys.* **1961**, *32*, 510.
(4) Eperon, G. E.; Leijtens, T.; Bush, K. A.; Prasanna, R.; Green, T.; Wang, J. T.-W.; McMeekin, D. P.; Volonakis, G.; Milot, R. L.; May, R.; Palmstrom, A.; Slotcavage, D. J.; Belisle, R. A.; Patel, J. B.; Parrott, E. S.; Sutton, R. J.; Ma, W.; Moghadam, F.; Conings, B.; Babayigit, A.; Boyen, H.-G.; Bent, S.; Giustino, F.; Herz, L. M.; Johnston, M. B.; McGehee, M. D.; Snaith, H. J. *Science* **2016**.
(5) Anaya, M.; Lozano, G.; Calvo, M. E.; Míguez, H. *Joule*, *1*, 769.
(6) Werner, J.; Barraud, L.; Walter, A.; Bräuninger, M.; Sahli, F.; Sacchetto, D.; Tétreault, N.; Paviet-Salomon, B.; Moon, S.-J.; Allebé, C.; Despeisse, M.; Nicolay, S.; De Wolf, S.; Niesen, B.; Ballif, C. *ACS Energy Lett.* **2016**, *1*, 474.
(7) Brenner, T. M.; Egger, D. A.; Kronik, L.; Hodes, G.; Cahen, D. *Nat. Rev. Mater.* **2016**, *1*, 15007.
(8) Xing, G.; Mathews, N.; Sun, S.; Lim, S. S.; Lam, Y. M.; Grätzel, M.; Mhaisalkar, S.; Sum, T. C. *Science* **2013**, *342*, 344.
(9) Stranks, S. D.; Eperon, G. E.; Grancini, G.; Menelaou, C.; Alcocer, M. J. P.; Leijtens, T.; Herz, L. M.; Petrozza, A.; Snaith, H. J. *Science* **2013**, *342*, 341.
(10) Even, J.; Pedesseau, L.; Katan, C. *J. Phys. Chem. C* **2014**, *118*, 11566.
(11) D'Innocenzo, V.; Grancini, G.; Alcocer, M. J. P.; Kandada, A. R. S.; Stranks, S. D.; Lee, M. M.; Lanzani, G.; Snaith, H. J.; Petrozza, A. *Nat. Commun.* **2014**, *5*, 3586.
(12) Yang, W. S.; Noh, J. H.; Jeon, N. J.; Kim, Y. C.; Ryu, S.; Seo, J.; Seok, S. I. *Science* **2015**, *348*, 1234.

(13) Wang, H.; Kim, D. H. *Chem. Soc. Rev.* **2017**, *46*, 5204.
(14) Lee, M. M.; Teuscher, J.; Miyasaka, T.; Murakami, T. N.; Snaith, H. J. *Science* **2012**, *338*, 643.
(15) Manser, J. S.; Christians, J. A.; Kamat, P. V. *Chem. Rev.* **2016**, *116*, 12956.
(16) Stoumpos, C. C.; Kanatzidis, M. G. *Adv. Mater.* **2016**, *28*, 5778.
(17) Miyata, A.; Mitioglu, A.; Plochocka, P.; Portugall, O.; Wang, J. T.-W.; Stranks, S. D.; Snaith, H. J.; Nicholas, R. J. *Nat. Phys.* **2015**, *11*, 582.
(18) Shi, D.; Adinolfi, V.; Comin, R.; Yuan, M.; Alarousu, E.; Buin, A.; Chen, Y.; Hoogland, S.; Rothenberger, A.; Katsiev, K.; Losovyj, Y.; Zhang, X.; Dowben, P. A.; Mohammed, O. F.; Sargent, E. H.; Bakr, O. M. *Science* **2015**, *347*, 519.
(19) Johnston, M. B.; Herz, L. M. *Acc. Chem. Res.* **2016**, *49*, 146.
(20) Herz, L. M. *Annu. Rev. Phys. Chem.* **2016**, *67*, 65.
(21) Miyata, K.; Meggiolaro, D.; Trinh, M. T.; Joshi, P. P.; Mosconi, E.; Jones, S. C.; De Angelis, F.; Zhu, X. Y. *Sci. Adv.* **2017**, *3*.
(22) Yamada, Y.; Nakamura, T.; Endo, M.; Wakamiya, A.; Kanemitsu, Y. *J. Am. Chem. Soc.* **2014**, *136*, 11610.
(23) Herz, L. M. *ACS Energy Lett.* **2017**, *2*, 1539.
(24) Ponseca, C. S.; Savenije, T. J.; Abdellah, M.; Zheng, K.; Yartsev, A.; Pascher, T.; Harlang, T.; Chabera, P.; Pullerits, T.; Stepanov, A.; Wolf, J.-P.; Sundström, V. *J. Am. Chem. Soc.* **2014**, *136*, 5189.
(25) Juarez-Perez, E. J.; Hawash, Z.; Raga, S. R.; Ono, L. K.; Qi, Y. *Energy Environ. Sci.* **2016**, *9*, 3406.
(26) Nenon, D. P.; Christians, J. A.; Wheeler, L. M.; Blackburn, J. L.; Sanehira, E. M.; Dou, B.; Olsen, M. L.; Zhu, K.; Berry, J. J.; Luther, J. M. *Energy Environ. Sci.* **2016**, *9*, 2072.
(27) Manser, J. S.; Saidaminov, M. I.; Christians, J. A.; Bakr, O. M.; Kamat, P. V. *Acc. Chem. Res.* **2016**, *49*, 330.
(28) Kulbak, M.; Cahen, D.; Hodes, G. *J. Phys. Chem. Lett.* **2015**, *6*, 2452.
(29) Kulbak, M.; Gupta, S.; Kedem, N.; Levine, I.; Bendikov, T.; Hodes, G.; Cahen, D. *J. Phys. Chem. Lett.* **2016**, *7*, 167.
(30) Beal, R. E.; Slotcavage, D. J.; Leijtens, T.; Bowring, A. R.; Belisle, R. A.; Nguyen, W. H.; Burkhard, G. F.; Hoke, E. T.; McGehee, M. D. *J. Phys. Chem. Lett.* **2016**, *7*, 746.
(31) Swarnkar, A.; Marshall, A. R.; Sanehira, E. M.; Chernomordik, B. D.; Moore, D. T.; Christians, J. A.; Chakrabarti, T.; Luther, J. M. *Science* **2016**, *354*, 92.
(32) Liang, J.; Wang, C.; Wang, Y.; Xu, Z.; Lu, Z.; Ma, Y.; Zhu, H.; Hu, Y.; Xiao, C.; Yi, X.; Zhu, G.; Lv, H.; Ma, L.; Chen, T.; Tie, Z.; Jin, Z.; Liu, J. *J. Am. Chem. Soc.* **2016**, *138*, 15829.
(33) Liang, J.; Zhao, P.; Wang, C.; Wang, Y.; Hu, Y.; Zhu, G.; Ma, L.; Liu, J.; Jin, Z. *J. Am. Chem. Soc.* **2017**, *139*, 14009.
(34) MØLler, C. K. *Nature* **1958**, *182*, 1436.
(35) Protesescu, L.; Yakunin, S.; Bodnarchuk, M. I.; Krieg, F.; Caputo, R.; Hendon, C. H.; Yang, R. X.; Walsh, A.; Kovalenko, M. V. *Nano Lett.* **2015**, *15*, 3692.
(36) Lin, J.; Gomez, L.; de Weerd, C.; Fujiwara, Y.; Gregorkiewicz, T.; Suenaga, K. *Nano Lett.* **2016**, *16*, 7198.
(37) Akkerman, Q. A.; D'Innocenzo, V.; Accornero, S.; Scarpellini, A.; Petrozza, A.; Prato, M.; Manna, L. *J. Am. Chem. Soc.* **2015**, *137*, 10276.
(38) Zhang, D.; Yang, Y.; Bekenstein, Y.; Yu, Y.; Gibson, N. A.; Wong, A. B.; Eaton, S. W.; Kornienko, N.; Kong, Q.; Lai, M. *J. Am. Chem. Soc.* **2016**, *138*, 7236.
(39) Zhang, X.; Lin, H.; Huang, H.; Reckmeier, C.; Zhang, Y.; Choy, W. C. H.; Rogach, A. L. *Nano Lett.* **2016**, *16*, 1415.

(40) Yakunin, S.; Protesescu, L.; Krieg, F.; Bodnarchuk, M. I.; Nedelcu, G.; Humer, M.; De Luca, G.; Fiebig, M.; Heiss, W.; Kovalenko, M. V. *Nat. Commun.* **2015**, *6*, 8056.
(41) Wang, Y.; Li, X.; Song, J.; Xiao, L.; Zeng, H.; Sun, H. *Adv. Mater.* **2015**, *27*, 7101.
(42) Yakunin, S.; Sytnyk, M.; Kriegner, D.; Shrestha, S.; Richter, M.; Matt, G. J.; Azimi, H.; Brabec, C. J.; Stangl, J.; Kovalenko, M. V.; Heiss, W. *Nat. photon.* **2015**, *9*, 444.
(43) Ramasamy, P.; Lim, D.-H.; Kim, B.; Lee, S.-H.; Lee, M.-S.; Lee, J.-S. *Chem. Commun.* **2016**, *52*, 2067.
(44) Park, Y.-S.; Guo, S.; Makarov, N. S.; Klimov, V. I. *ACS Nano* **2015**, *9*, 10386.
(45) Wang, Y.; Sun, H. *Small Methods*, 1700252.
(46) Swarnkar, A.; Chulliyil, R.; Ravi, V. K.; Irfanullah, M.; Chowdhury, A.; Nag, A. *Angew. Chem. Int. Ed.* **2015**, *54*, 15424.
(47) Seth, S.; Mondal, N.; Patra, S.; Samanta, A. *J. Phys. Chem. Lett.* **2016**, *7*, 266.
(48) Yettapu, G. R.; Talukdar, D.; Sarkar, S.; Swarnkar, A.; Nag, A.; Ghosh, P.; Mandal, P. *Nano Lett.* **2016**, *16*, 4838.
(49) Mondal, N.; Samanta, A. *Nanoscale* **2017**, *9*, 1878.
(50) Koscher, B. A.; Swabeck, J. K.; Bronstein, N. D.; Alivisatos, A. P. *J. Am. Chem. Soc.* **2017**, *139*, 6566.
(51) Klimov, V. I. *Nanocrystal Quantum Dots, Second Edition*; CRC Press

2010.
(52) Talapin, D. V.; Lee, J.-S.; Kovalenko, M. V.; Shevchenko, E. V. *Chem. Rev.* **2010**, *110*, 389.
(53) Kagan, C. R.; Lifshitz, E.; Sargent, E. H.; Talapin, D. V. *Science* **2016**, *353*.
(54) Pietryga, J. M.; Park, Y.-S.; Lim, J.; Fidler, A. F.; Bae, W. K.; Brovelli, S.; Klimov, V. I. *Chem. Rev.* **2016**, *116*, 10513.
(55) Smith, A. M.; Nie, S. *Acc. Chem. Res.* **2010**, *43*, 190.
(56) Boles, M. A.; Ling, D.; Hyeon, T.; Talapin, D. V. *Nat. Mater.* **2016**, *15*, 141.
(57) Aldana, J.; Wang, Y. A.; Peng, X. *J. Am. Chem. Soc.* **2001**, *123*, 8844.
(58) Munro, A. M.; Jen-La Plante, I.; Ng, M. S.; Ginger, D. S. *J. Phys. Chem. C* **2007**, *111*, 6220.
(59) Hines, M. A.; Guyot-Sionnest, P. *J. Phys. Chem.* **1996**, *100*, 468.
(60) Chen, O.; Zhao, J.; Chauhan, V. P.; Cui, J.; Wong, C.; Harris, D. K.; Wei, H.; Han, H.-S.; Fukumura, D.; Jain, R. K.; Bawendi, M. G. *Nat. Mater.* **2013**, *12*, 445.
(61) Filippetti, A.; Mattoni, A. *Phys. Rev. B* **2014**, *89*, 125203.
(62) Umebayashi, T.; Asai, K.; Kondo, T.; Nakao, A. *Phys. Rev. B* **2003**, *67*, 155405.
(63) Ravi, V. K.; Markad, G. B.; Nag, A. *ACS Energy Lett.* **2016**, *1*, 665.
(64) Brandt, R. E.; Stevanović, V.; Ginley, D. S.; Buonassisi, T. *MRS Commun.* **2015**, *5*, 265.
(65) Guo, Y.; Wang, Q.; Saidi, W. A. *J. Phys. Chem. C* **2017**, *121*, 1715.
(66) Kang, J.; Wang, L.-W. *J. Phys. Chem. Lett.* **2017**, *8*, 489.
(67) Knutson, J. L.; Martin, J. D.; Mitzi, D. B. *Inorg. Chem.* **2005**, *44*, 4699.
(68) Amat, A.; Mosconi, E.; Ronca, E.; Quarti, C.; Umari, P.; Nazeeruddin, M. K.; Grätzel, M.; De Angelis, F. *Nano Lett.* **2014**, *14*, 3608.
(69) Filip, M. R.; Eperon, G. E.; Snaith, H. J.; Giustino, F. **2014**, *5*, 5757.
(70) Protesescu, L.; Yakunin, S.; Kumar, S.; Bär, J.; Bertolotti, F.; Masciocchi, N.; Guagliardi, A.; Grotevent, M.; Shorubalko, I.; Bodnarchuk, M. I.; Shih, C.-J.; Kovalenko, M. V. *ACS Nano* **2017**, *11*, 3119.
(71) Beattie, A. R.; Landsberg, P. T. *Proc. R. Soc. Lond. A Math. Phys. Sci.* **1959**, *249*, 16.
(72) He, G. S.; Tan, L.-S.; Zheng, Q.; Prasad, P. N. *Chem. Rev.* **2008**, *108*, 1245.

(73) Xu, Y.; Chen, Q.; Zhang, C.; Wang, R.; Wu, H.; Zhang, X.; Xing, G.; Yu, W. W.; Wang, X.; Zhang, Y. *J. Am. Chem. Soc.* **2016**, *138*, 3761.
(74) He, G. S.; Tan, L.-S.; Zheng, Q.; Prasad, P. N. *Chemical Reviews* **2008**, *108*, 1245.
(75) Ueno, Y.; Ajito, K. *Anal. Sci.* **2008**, *24*, 185.
(76) McIntosh, A. I.; Yang, B.; Goldup, S. M.; Watkinson, M.; Donnan, R. S. *Chem. Soc. Rev.* **2012**, *41*, 2072.
(77) Schmuttenmaer, C. A. *Chem. Rev.* **2004**, *104*, 1759.
(78) Kemp, M. C.; Taday, P. F.; Cole, B. E.; Cluff, J. A.; Fitzgerald, A. J.; Tribe, W. R.; 6 ed.; Vol. 5070, p 44.
(79) Lu, J. y.; Chen, L. j.; Kao, T. f.; Chang, H. h.; Chen, H. w.; Liu, A. s.; Chen, Y. c.; Wu, R. b.; Liu, W. s.; Chyi, J. i.; Sun, C. k. *IEEE Photonic. Tech. L.* **2006**, *18*, 2254.
(80) Foltynowicz, R. J.; Allman, R. E.; Zuckerman, E. *Chem. Phys. Lett.* **2006**, *431*, 34.
(81) Melinger, J. S.; Laman, N.; Grischkowsky, D. *Appl. Phys. Lett.* **2008**, *93*, 011102.
(82) Markelz, A. G. *IEEE J. Sel. Top Quantum Electron.* **2008**, *14*, 180.
(83) Son, J.-H. *J. Appl. Phys.* **2009**, *105*, 102033.
(84) Siegel, P. H. *IEEE Trans. Microw. Theory Tech.* **2004**, *52*, 2438.
(85) Laman, N.; Harsha, S. S.; Grischkowsky, D.; Melinger, J. S. *Biophys. J.* **2008**, *94*, 1010.
(86) Heyden, M.; Bründermann, E.; Heugen, U.; Niehues, G.; Leitner, D. M.; Havenith, M. *J. Am. Chem. Soc.* **2008**, *130*, 5773.
(87) Walther, M.; Plochocka, P.; Fischer, B.; Helm, H.; Uhd Jepsen, P. *Biopolymers* **2002**, *67*, 310.
(88) Wang, W.-N.; Li, H.-Q.; Zhang, Y.; Zhang, C.-L. *Acta Phys. Chim. Sin.* **2009**, *25*, 2074.
(89) Png, G. M.; Choi, J. W.; Ng, B. W.; Mickan, S. P.; Abbott, D.; Zhang, X. C. *Phys. Med. Biol.* **2008**, *53*, 3501.
(90) Stanley, S.; Shengyang, H.; Yi-Xiang, J. W.; Jun, Y.; Anil, T. A.; Yuan-ting, Z.; Emma, P.-M. *Phys. Med. Biol.* **2010**, *55*, 7587.
(91) Zeitler, J. A.; Gladden, L. F. *Eur. J. Pharm. Biopharm.* **2009**, *71*, 2.
(92) McGoverin, C. M.; Rades, T.; Gordon, K. C. *J. Pharm. Sci.* **2008**, *97*, 4598.
(93) Zeitler, J. A.; Taday, P. F.; Newnham, D. A.; Pepper, M.; Gordon, K. C.; Rades, T. *J. Pharm. Pharmacol.* **2007**, *59*, 209.
(94) Jepsen, P. U.; Cooke, D. G.; Koch, M. *Laser Photonics Rev.* **2011**, *5*, 124.
(95) Smith, P. R.; Auston, D. H.; Nuss, M. C. *IEEE J. Quantum Electron.* **1988**, *24*, 255.
(96) Fattinger, C.; Grischkowsky, D. *Appl. Phys. Lett.* **1989**, *54*, 490.
(97) Auston, D. H.; Nuss, M. C. *IEEE J. Quantum Electron.* **1988**, *24*, 184.
(98) van Exter, M.; Fattinger, C.; Grischkowsky, D. *Appl. Phys. Lett.* **1989**, *55*, 337.
(99) Nahata, A.; Weling, A. S.; Heinz, T. F. *Appl. Phys. Lett.* **1996**, *69*, 2321.
(100) Gallot, G.; Grischkowsky, D. *J. Opt. Soc. Am. B* **1999**, *16*, 1204.
(101) Blanchard, F.; Razzari, L.; Bandulet, H. C.; Sharma, G.; Morandotti, R.; Kieffer, J. C.; Ozaki, T.; Reid, M.; Tiedje, H. F.; Haugen, H. K.; Hegmann, F. A. *Opt. Express* **2007**, *15*, 13212.
(102) Baxter, J. B.; Guglietta, G. W. *Anal. Chem.* **2011**, *83*, 4342.
(103) Němec, H.; Kužel, P.; Sundström, V. *J. Photoch. Photobio. A.* **2010**, *215*, 123.
(104) Lloyd-Hughes, J.; Jeon, T.-I. *J. Infrared Millim. Terahertz Waves* **2012**, *33*, 871.
(105) Mandal, P. K.; Chikan, V. *Nano Lett.* **2007**, *7*, 2521.
(106) Guglietta, G. W.; Diroll, B. T.; Gaulding, E. A.; Fordham, J. L.; Li, S.; Murray, C. B.; Baxter, J. B. *ACS Nano* **2015**, *9*, 1820.
(107) Ulbricht, R.; Hendry, E.; Shan, J.; Heinz, T. F.; Bonn, M. *Rev. Mod. Phys.* **2011**, *83*, 543.
(108) Ho, I. C.; Guo, X.; Zhang, X. C. *Opt. Express* **2010**, *18*, 2872.

(109) Savenije, T. J.; Kroeze, J. E.; Wienk, M. M.; Kroon, J. M.; Warman, J. M. *Phys. Rev. B* **2004**, *69*, 155205.
(110) Lui, C. H.; Frenzel, A. J.; Pilon, D. V.; Lee, Y. H.; Ling, X.; Akselrod, G. M.; Kong, J.; Gedik, N. *Phys. Rev. Lett.* **2014**, *113*, 166801.
(111) Wang, F.; Shan, J.; Islam, M. A.; Herman, I. P.; Bonn, M.; Heinz, T. F. *Nat. Mater.* **2006**, *5*, 861.
(112) Ziwritsch, M.; Müller, S.; Hempel, H.; Unold, T.; Abdi, F. F.; van de Krol, R.; Friedrich, D.; Eichberger, R. *ACS Energy Lett.* **2016**, *1*, 888.
(113) Butler, K. T.; Dringoli, B. J.; Zhou, L.; Rao, P. M.; Walsh, A.; Titova, L. V. *J. Mater. Chem. A* **2016**, *4*, 18516.
(114) Smith, N. V. *Phys. Rev. B* **2001**, *64*, 155106.
(115) Nienhuys, H.-K.; Sundström, V. *Appl. Phys. Lett.* **2005**, *87*, 012101.
(116) Karakus, M.; Jensen, S. A.; D'Angelo, F.; Turchinovich, D.; Bonn, M.; Cánovas, E. *J. Phys. Chem. Lett.* **2015**, *6*, 4991.

Chapter 2

Experimental Procedures and Data Analysis

2.1 Introduction:

In this chapter, broadband THz (>15 THz) generation from air and detection with air-biased coherent detection, optical pump-THz probe setup, analysis for obtaining optical constants such as refractive index, dielectric function, conductivity and mobility, effective medium theories, and conductivity models are described. The THz bandwidth is limited only by optical pulse duration unlike electro-optic (EO) sampling method, where THz bandwidth is limited by damage threshold and phonon absorption of the crystal. Effective medium theories are discussed to obtain the response solely from NCs. The conductivity models discussed here are employed in the forthcoming chapters to fit the conductivity spectra thereby deriving the carrier density and mobility.

2.2 Time-Domain THz spectroscopy:

2.2.1 THz-TDS set-up:

The schematic of our experimental setup to generate THz light from air plasma and detect it with air biased coherent detection (ABCD) method is shown in Figure 2.1.[1-3] A ultrafast regenerative amplifier (Spitfire Pro XP, Spectra-Physics) seeded by a femtosecond oscillator (Tsunami, Spectra-Physics) generates pulses of 50 fs (FWHM), 800 nm central wavelength at 1 kHz repetition rate. The laser beam is split into two equal parts by using a beam splitter (BS 1). One part is utilized to generate and detect THz radiation and the other part is fed into an optical parametric amplifier (OPA) to generate the optical pump pulses of varying wavelengths.

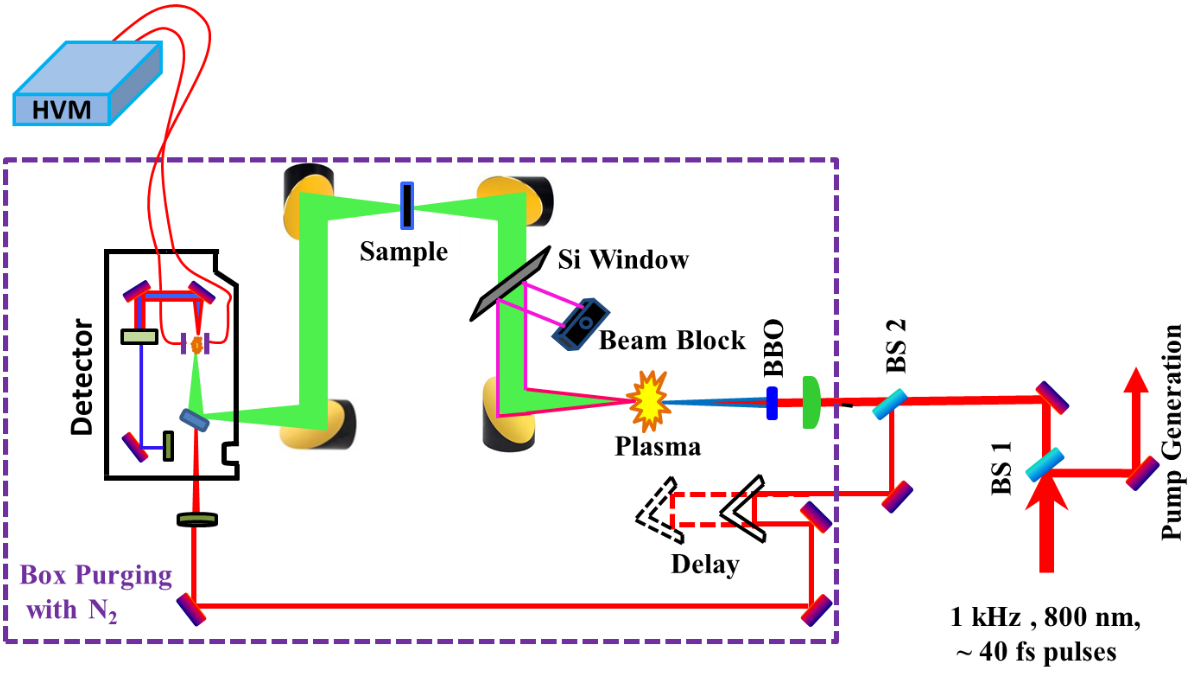

Figure 2.1: Experimental setup for Time-domain THz spectroscopy. THz radiation is generated by air plasma and detected by air biased coherent detection (ABCD) method.

The first part is again split into two beams by using another beam splitter, shown as BS 2 (R:T = 8:92) in the schematic. The transmitted beam (ω) passes through the BBO (Type 1 beta barium borate) crystal that creates the second harmonic (2ω). A plano-convex lens placed between the BBO and BS2 focuses the fundamental (ω) and the second harmonic (2ω) in the ambient air to create a strong plasma. The plasma gives THz radiation along with other electromagnetic radiations. The THz radiation, filtered out by high-resistivity float-zone Silicon filter, is collimated and focused to a spot size of ~1 mm diameter on to the sample with the first pair of off-axis parabolic mirrors. The THz radiation transmitted through the sample is re-collimated and focused between two electrodes by another set of parabolic mirrors. The reflected beam from the BS 2, called probe or gate beam which is reflected further by the retro reflector kept on a delay line (50 mm) is also focused between the electrodes. An AC voltage of 1.5 kV on each electrode from high voltage modulator (HVM) is applied. The modulation frequency of HVM is kept at half (500 Hz) the laser repetition rate and synchronised with laser repetition rate. The bias field supplied by the electrodes acts as a local oscillator (LO) and together with THz and fundamental (800 nm) gate beam generate the second harmonic (400 nm) of the gate beam. The second harmonic signal is filtered from the residual fundamental beam with band pass filter and detected by a photomultiplier tube (PMT). The PMT current is amplified using a current preamplifier whrere the photocurrent signal converts into a slowly varying voltage signal. This signal is fed into the lock-in amplifier referenced at the frequency of the LO. The amplitude is proportional to THz electric field strength. The lock-in amplifier signal is recorded as the time delay between the gate beam and THz beam, is varied by scanning the optical delay stage (shown as "Delay" in the schematic).

2.2.2 Broadband THz generation from air plasma:

The first demonstration of THz wave generation from plasma started in the early 90s by focusing the fundamental beam into gases.[4,5] However, the realizations of intense THz waves were possible only when both the fundamental and the second harmonic beams were focussed into air.[6-8] The mechanism of the generation of THz radiation in gas plasma is not completely understood. There are two models which can explain the nonlinear optical processes occurring in gaseous media. They are four-wave mixing (FWM) model,[1,6] and asymmetric transient current (ATC) model.[9,10] In four-wave mixing process, the difference between a photon of energy $2\omega + \Omega_{THz}$ and the sum of energies of two photons (ω), yields THz radiation. The four-wave mixing process can be represented as

$$\Omega_{THz} = (2\omega + \Omega_{THz}) - \omega - \omega \qquad (2.1)$$

The generated THz field amplitude is proportional to the intensity of the fundamental (ω) and to the square root of the second harmonic (2ω) beams,

$$E_{THz} \propto \chi^{(3)} \sqrt{I_{2\omega}}\, I_{\omega} \cos(\varphi) \qquad (2.2)$$

where φ is the phase difference between fundamental and second harmonic waves. The optimal THz field is obtained when the polarizations of fundamental, second harmonic and THz waves are parallel in the FWM process.

According to the transient current model, a current surge is generated when the bound electrons are stripped off from atoms in the asymmetric field created by the mixing of second harmonic and fundamental waves. This current surge can produce an electromagnetic pulse at THz frequencies. The efficiency of THz generation varies in these two models depending on the phase difference between the fundamental and second harmonic beams. In FWM approximation, THz efficiency reaches its peak when the phase difference is zero. On the other hand, it is highest when the relative phase is π/2, in the case of ATC model.

2.2.3 Air biased coherent detection (ABCD) of THz:

Broadband THz detection using air as the sensor was first demonstrated in 2006 and subsequently, field strength was increased by using external bias as a local oscillator.[2,3] The principle behind the sensing of broadband THz radiation is to measure the THz field induced second harmonic (TFISH) through the third-order nonlinear process. The THz induced second harmonic electric field amplitude can be written as

$$E_{2\omega}^{THz} \propto \chi^{(3)} E_{\omega} E_{\omega} E_{THz} \tag{2.3}$$

where $\chi^{(3)}$ is third order nonlinear susceptibility of air, $E_{2\omega}^{THz}, E_{\omega}$, and E_{THz} are the electric field amplitude of the second harmonic, fundamental, and THz waves respectively. Since $E_{2\omega}^{THz} \propto E_{THz}$ the intensity is related to $I_{2\omega}^{THz} \propto I_{THz}$. The phase information is lost, i.e. the measurement is incoherent. The voltage supplied by the electrodes acts as a local oscillator and its second harmonic contribution towards total second harmonic amplitude is $E_{2\omega}^{LO}$. Thus, the total second harmonic from LO and THz induced SH components can be written as

$$I_{2\omega} \propto (E_{2\omega})^2 = (E_{2\omega}^{THz} + E_{2\omega}^{LO})^2 \tag{2.4}$$

$$= (E_{2\omega}^{THz})^2 + 2\,(E_{2\omega}^{THz} E_{2\omega}^{LO} \cos\varphi) + (E_{2\omega}^{LO})^2 \tag{2.5}$$

where φ is the phase difference between $E_{2\omega}^{THz}$ and $E_{2\omega}^{LO}$. The above equation can be written as

$$= \left(\chi^{(3)} I_{\omega}\right)^2 I_{THz} + 2\,\chi^{(3)} I_{\omega} E_{2\omega}^{LO} E_{THz} \cos\varphi + (E_{2\omega}^{LO})^2. \tag{2.6}$$

The second term which is proportional to E_{THz} is the key for the coherent detection. By modulating THz wave, one can remove the third term, DC component originated from LO, by using a lock-in amplifier. The second term dominates when the probe intensity is above the plasma threshold. Thus, the THz detection becomes coherent.

We have employed ABCD successfully and are able to detect broadband THz pulse (up to 15 THz), see Figure 2.2., which will enable us to study probe processes taking place in this wide frequency range.

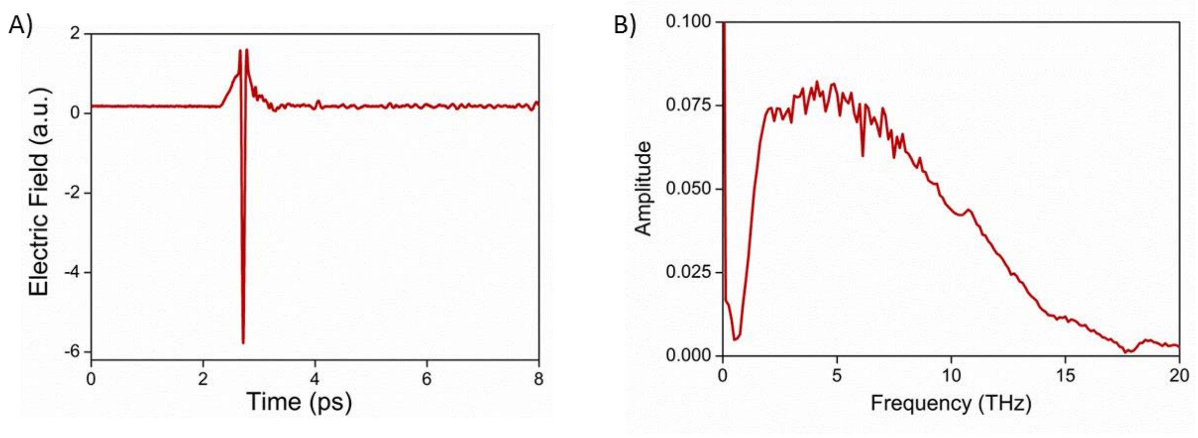

Figure 2.2: Time domain THz waveform and its amplitude spectrum detected using our spectrometer.

2.3 Optical Pump-THz probe spectroscopy:

The experimental set-up for time-resolved THz spectroscopy (TRTS), also known as optical pump THz probe spectroscopy (OPTS) is shown in Figure 2.3. For the time-resolved THz study, an ultrafast pump beam generated from the OPA excites the sample prior to the arrival of a THz probe pulse. The delay between the optical pump and THz probe beam is varied by scanning the 300 mm long delay stage, marked as Delay 3 in Figure 2.3. A variable neutral density filter, placed in the pump path, controls the pump power. The pump beam is chopped using a mechanical chopper rotating at a frequency of 333 Hz. At this frequency, every third pulse of the pump beam is allowed to reach the sample. The pump beam passes through a hole in the off-axis parabolic mirror (PM2) and becomes collinear with the THz beam. The pump beam diameter on to the sample is ~ 3.5 mm, 3.5 times greater than the THz beam diameter to guarantee uniform sample excitation. The optical pump and THz probe diameters were measured by the knife-edge technique. We used a black polyethylene (transparent to the THz probe) sheet to block the pump light transmitted through the sample from reaching out to the PMT.

The pump-probe experiment is carried out using double lock-in technique in which the pump-induced change in THz transmission ($-\Delta E(t_p)$) and the corresponding THz transmission through the non-photoexcited sample ($E_0(t_p)$) are recorded simultaneously.[5] This ensures to keep the effect of laser fluctuation to the minimum. The signal from the current preamplifier is split and sent to two separate lock-in amplifiers. The THz probe beam is modulated at 500 Hz and this frequency acts as the reference for one lock-in amplifier. The reference frequency for the second lock-in amplifier is 333 Hz, the frequency at which the optical pump beam is modulated. To minimize the crosstalk between the signals measured at 500 Hz and 333 Hz, the frequencies are not harmonic with respect to each other.

The pump-induced signal can be collected in two ways. a) Frequency averaged experiments are performed by varying the delay between the optical pump and THz probe by scanning the 300 mm long stage (Delay 3) after fixing the 50 mm stage (Delay 1 or Delay 2) at peak THz field (t_{max}). The photoinduced change in THz field amplitude, $\Delta E(t_{max}, t_p)$, is recorded as a function of delay between the THz probe and the optical pump pulses, t_p. This provides the temporal evolution of the photoexcited sample. b) Frequency resolved experiments which are performed by scanning the 50 mm stage (Delay 1 or Delay 2) at a fixed pump-probe delay (Delay 3), yield the pump induced changes in THz waveform, $\Delta E(t, t_p)$, at a fixed pump-probe delay (t_p).

To avoid THz absorption by water vapour, the entire experimental setup is enclosed in a transparent box and purged continuously with N_2 or dry air.

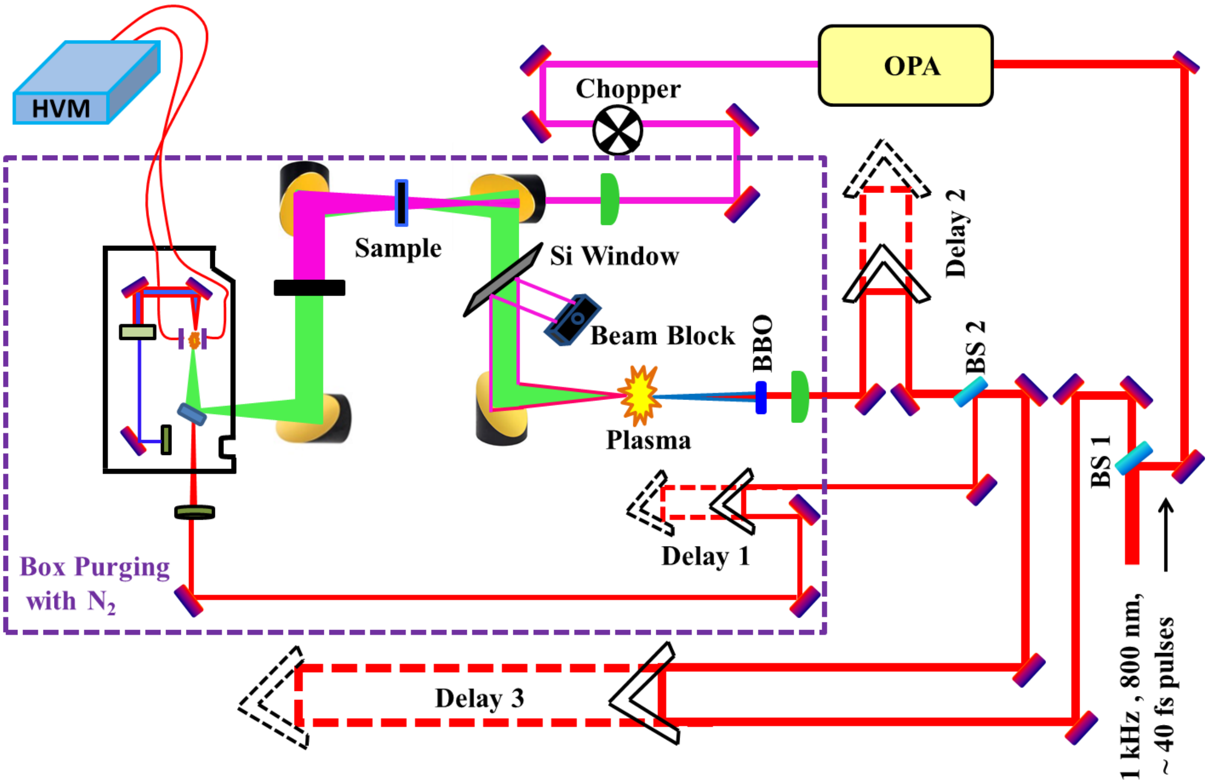

Figure 2.3: Complete experimental setup for time-resolved THz spectroscopy.

2.4 Data Analysis:

2.4.1 Analysis of steady state (THz-TDS) experiments:

If the electric field of the THz pulses in time domain transmitted through the sample and reference are $E_S(t)$ and $E_R(t)$, respectively, then their Fourier transforms, $E_S(\omega)$, $E_R(\omega)$ in the frequency domain are:

$$E_S(\omega) = E_0(\omega)T_S(\omega) \tag{2.7}$$

$$E_R(\omega) = E_0(\omega)T_R(\omega) \tag{2.8}$$

where $T(\omega)$ is the transmission function which is obtained from the Fresnel coefficients and propagation coefficients.

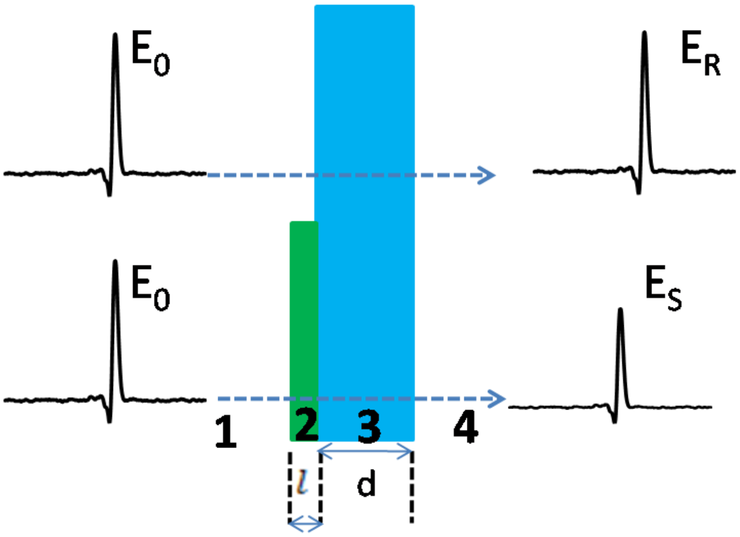

Figure 2.4: Schematic of the sample deposited on the substrate and the electric fields passing through the substrate and sample are represented as E_R and E_S.

For Sample: $T_S(\omega) = t_{12}p_2(l)p_3(d)t_{23}t_{34}$ (2.9)

For Reference: $T_R(\omega) = t_{13}p_1(l)p_3(d)t_{34}$ (2.10)

Where t is Fresnel coefficient at normal incidence and p is the propagation coefficient and are given by

$$t_{xy} = \frac{2\tilde{n}_x}{\tilde{n}_x + \tilde{n}_y} \tag{2.11}$$

$$p_x(l) = e^{i\tilde{n}_x l\omega/c}\,;\omega = 2\pi\nu \tag{2.12}$$

By dividing Equations (2.7) by Equation (2.8), we will have Transmission function as

$$T(\omega) = \frac{E_S(\omega)}{E_R(\omega)} = \frac{t_{12}p_2(l)t_{23}}{t_{13}p_1(l)} \tag{2.13}$$

$$T(\omega) = \frac{2\tilde{n}_2(\tilde{n}_1 + \tilde{n}_3)}{(\tilde{n}_1 + \tilde{n}_2)(\tilde{n}_2 + \tilde{n}_3)} e^{i(\tilde{n}_2 - \tilde{n}_1)l\omega/c} \tag{2.14}$$

Under the assumption of very less THz light absorption by the sample,

$$\tilde{n}_x = n_x + ik_x; k_x \cong 0, \tilde{n}_x = n_x \tag{2.15}$$

Next, by separating the real and imaginary parts and comparing with the measured transmission function,

$$T_{meas}(\omega) = |R(\omega)|e^{i\Delta\phi} \qquad (2.16)$$

we obtain

$$n_2 = n_1 + \frac{c}{l\omega}\Delta\phi \qquad (2.17)$$

$$k_2 = -\frac{c}{l\omega}\ln[\eta(\nu)|R(\omega)|]\,;\ \eta(\nu) = \frac{(n_1+n_2)(n_2+n_3)}{2n_2(n_1+n_3)} \qquad (2.18)$$

Since the extinction coefficient (k) and absorption coefficient (α) are related as $k = \frac{\alpha c}{2\omega}$, the absorption coefficient is given by

$$\alpha_2 = -\frac{2}{l}\ln[\eta(\nu)|R(\omega)|] \qquad (2.19)$$

Absorbance (A) of the sample = Absorption coefficient $*$ thickness.

Generally, Fabry-Perot modes (or Etalon effect) arise from multiple reflections at interfaces. If the sample is thick and strongly absorbing, one can cut off the time domain data till first echo and can obtain refractive index and absorption coefficients. This is till acceptable in the literature. However, in case of low absorbing materials one cannot cut the time domain data, instead one need to add the multiple reflection terms such as Frenel coefficients and propagation coefficients to the equation 2.13. This will remove artificial periodic modulations and errors in the optical constants.

The multiple reflection term included THz electric field through the sample is given by

$$E_R(\omega) = E_0(\omega)t_{12}p_2(l)p_3(d)t_{23}t_{34}\sum_j (r_{23}p_2^2(l)r_{21})^j$$

Where j indicates the number of reflections. Reflection term (r_{xy}) is given by

$$r_{xy} = \frac{n_x - n_y}{n_x + n_y}$$

From the given refractive index (n) and extinction coefficient, the complex refractive index can be written as

$$\tilde{n} = n_2 + ik_2 \quad (2.20)$$

The dielectric function is related to complex refractive index as

$$\tilde{\varepsilon} = \varepsilon_1 + i\,\varepsilon_2 = \tilde{n}^2 \quad (2.21)$$

where $\varepsilon_1 = {n_2}^2 - {k_2}^2$ and $\varepsilon_2 = 2n_2k_2$.

The dielectric function obtained for NC solution is an effective function for the solution comprising the solutes (NCs) and the solvent entities. The individual solute (NC) dielectric function can be obtained using an appropriate effective medium theory (see effective medium theory section).

The complex conductivity can be obtained from the dielectric function as follows[11]

$$\tilde{\sigma} = -2\pi i\nu\varepsilon_0\tilde{\varepsilon} \quad (2.22)$$

2.4.2 Transient photoconductivity of NC solution:

The pump-induced change in photoconductivity, Δσ, of NCs dispersed in HMN solvent placed between the two TPX windows, under the condition that $\Delta n \ll 1$, is expressed as[12,13]

$$\Delta\hat{\sigma}(\omega) = -2i\omega\varepsilon_0 n_2 \Delta\hat{n} \quad (2.23),$$

where n_2 is the refractive index of the NCs solution and Δn is given by

$$\Delta\hat{n} = \left[\frac{i\omega l}{c} - \frac{n_2 - n_1}{n_2(n_2+n_1)} + MR\right]^{-1} \frac{\Delta E_{out}(\omega)}{E_{out}(\omega)} \quad (2.24).$$

Here, *l* is the path length of the sample, n_1 is the refractive index of the TPX window (n_1= 1.524), n_2 is the refractive index of the NCs solution (n_2=1.61), MR is multiple reflection term (here MR= 0) and $\Delta E(\omega)$, $E(\omega)$ are respectively pump-induced and pump-off Fourier transforms of transmitted THz electric fields.

The pump-induced change in dielectric function of the NC solution obtained from the conductivity spectrum (calculated from Eq. 2.23) is

$$\Delta\hat{\varepsilon}(\omega) = i\Delta\hat{\sigma}(\omega)/\omega\varepsilon_0 \qquad (2.25).$$

The effective dielectric constant of the photoexcited NCs can be calculated from the effective dielectric constant of the non-photoexcited NCs and pump induced change in dielectric constant of NCs solution using the following equation:

$$\hat{\varepsilon}_{eff}{}^{np} + \Delta\hat{\varepsilon} = \hat{\varepsilon}_{eff}{}^{pe} \qquad (2.26)$$

After calculating $\hat{\varepsilon}_{eff}{}^{pe}$ using Eq. 2.26 and using this value in Eq. 2.35 (effective medium theory), the intrinsic dielectric constant of the photoexcited NCs can be calculated ($\varepsilon_i{}^{pe}$). The difference between $\varepsilon_i{}^{pe}$ and $\varepsilon_i{}^{np}$ (intrinsic dielectric constant of the non-photoexcited NCs) is given by,

$$\Delta\hat{\varepsilon}_i{}^{pe} = \hat{\varepsilon}_i{}^{pe} - \hat{\varepsilon}_i{}^{np} \qquad (2.27)$$

which is the pump-induced change in dielectric constant of NCs. The pump induced conductivity ($\Delta\sigma_{ind}$) of NCs can be calculated from $\Delta\hat{\varepsilon}_i{}^{pe}$ using Eq. 2.25.

In the above calculation for the THz conductivity of NCs, it is assumed that the entire sample (thickness d) gets photoexcited. But the actual THz conductivity should be calculated for the thickness (skin depth δ) of the photoexcited sample. So it must be corrected by a factor of d/δ if d > δ. Thus the real photo induced THz conductivity of NCs is given by,[14]

$$\Delta\sigma = \frac{d}{\delta}\,\Delta\sigma_{ind} \qquad (2.28).$$

In Chapter 3, for 480 and 504 nm pump, sample thickness was less than the corresponding skin depths. Hence, multiplication of the conductivity with the scaling factor (d/δ) was not required. However, in the case of 400 nm, the skin depth (δ = 546 µm) was less than the sample thickness (d = 950 µm), so conductivity was multiplied with 1.74 ($\frac{d}{\delta}$ = 1.74).

2.4.3 THz Peak conductivity and mobilities for the film:

The peak conductivities can be calculated from the observed peak THz transients, under the condition of d << λ, by using the following relation[15,16]

$$\Delta\sigma(t_p) = \frac{\varepsilon_0 c}{d}(n_a + n_b)\frac{-\Delta E(t_p)}{E_0(t_p)} \qquad (2.29)$$

where n_a, n_b are refractive indices of media on either of the sample, ε_0 is the permittivity of free space, c is the speed of light and d is the thickness of the photoexcited sample.

The initial mobilities can be obtained by normalizing the peak conductivities with carrier density (N_0). In the linear excitation regime, assuming that each absorbed photon results in one electron-hole pair ($\varphi = 1$), the mobility is given by

$$\mu \cong \frac{\Delta\sigma}{qN_0} \qquad (2.30),$$

where N_0 is the total carrier density ($N_0 = \varphi.2N_{Ph}$) and q is the elementary charge. However, as the value of the photon to the free carrier conversion ratio (φ) is not known, this method yields an effective mobility ($\varphi\mu$) rather than the actual mobility (μ). The density of absorbed photon (N_{ph}) is calculated as: $N_{ph} = (F_l\ (1 - 10^{-OD_\lambda}\ ))/\delta h\nu$; where F_l is the incident photon flux, $(1 - 10^{-OD_\lambda})$ is the fraction of the pump light absorbed by the sample, δ is the penetration depth, and $h\nu$ is the energy of a single photon. This gives the upper limit of N_{ph} as we are ignoring reflection and scattering losses in our experiments.

To obtain the frequency-resolved conductivity spectra complete THz waveforms were collected at each pump-probe delay (τ_p). Again, Equation 2.29 was used to get the conductivity spectra, where $-\Delta E(t_p)$ and $E_0(t_p)$are the Fourier transforms of the recorded photoinduced change in the THz waveform and the reference THz waveform, respectively. This frequency resolved conductivity were fitted to the appropriate conductivity models to determine several important parameters such as carrier density (N_0), mobility (μ) etc. at each pump-probe delay (τ_p).

2.5 Effective Medium Theories (EMTs):

THz-TDS and OPTP experiments measure macroscopic permittivity/conductivity of composite systems, particles embedded in host materials, as shown in Figure 2.5. We use appropriate effective medium theory (EMT) approach to determine the intrinsic dielectric response of the particles of our interest (NCs in this thesis work). In the case of nanoparticle composites, the scattering effects are neglected since the wavelength of THz probe light (1 THz = 300 μm) is greater than the length scale of the nanoparticles (1 nm = 10^{-9} m).[17]

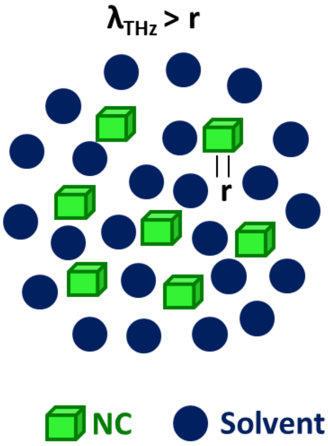

Figure 2.5: The effective dielectric function of NC composite (ε), scattering effects are negligible as the wavelength of THz is larger than the size of NC.

Though there are several EMTs in the literature,[17,18] the most used ones are Maxwell-Garnett (MG) and Bruggemann.[19,20]

2.5.1 Maxwell-Garnett theory:

In MG theory, the experimentally observed effective dielectric function (ε) is related to the dielectric functions of the host (ε_h) and the inclusion (ε_P) materials as:

$$\frac{\varepsilon-\varepsilon_h}{\varepsilon+K\varepsilon_h}=f\,\frac{\varepsilon_P-\varepsilon_h}{\varepsilon_P+K\varepsilon_h} \tag{2.31}$$

where f is the volume fraction of the inclusions and K is the geometry factor.

This also can be rearranged for nanoparticles as

$$\varepsilon_P = \frac{(f\varepsilon_h\,\varepsilon + K\varepsilon\varepsilon_h - K{\varepsilon_h}^2 + fK{\varepsilon_h}^2)}{(fK\varepsilon + f\varepsilon + \varepsilon_h - \varepsilon)} \tag{2.32}$$

MG theory has its own limitations. It is not applicable when there is charge transport occurring between the NCs. However, it is very less likely that charge transport will take place in NCs because the NCs are capped with insulating capping ligands and are surrounded by non-conducting host medium. It is also not applicable for concentrated solutions. In case of large filling fractions and the large dielectric contrast between the constituents, the Bruggemann theory is applicable.

2.5.2 Bruggeman effective medium theory:

In Bruggeman theory, the experimentally observed effective dielectric function (ε) is related to the dielectric functions of the host (ε_h) and the inclusion (ε_P) materials as:

$$f\,\frac{\varepsilon_P - \varepsilon}{\varepsilon_P + K\varepsilon} = (f-1)\,\frac{\varepsilon_h - \varepsilon}{\varepsilon_h + K\varepsilon} \tag{2.33}$$

The above Equation (2.33) can be rearranged for nanoparticles as

$$\varepsilon_P = \frac{(f\varepsilon_h\,\varepsilon + Kf\varepsilon\varepsilon_h - K\varepsilon\varepsilon_h + K\varepsilon^2)}{(fK\varepsilon + f\varepsilon + \varepsilon_h - \varepsilon)} \tag{2.34}$$

Here f is the volume fraction and K is the geometric factor. For spherical particles K=2 and K=1 for long cylinders whose axis is perpendicular to the THz electric field.

However, these methods require the geometric factor of the constituent particles. At very low filling fractions (f is very low) linear effective medium approximation is more successful in obtaining the individual nanoparticles properties and is given by[21-23]

$$\varepsilon = f\varepsilon_p + (1-f)\varepsilon_h \tag{2.35}$$

We have used simple linear effective medium theory for determining the intrinsic properties of the individual NC from their solution data.

2.6 Conductivity Models:

Carriers generated in TRTS experiments possess typical signatures in frequency-resolved conductivity spectrum. Time evolution of transport properties such as mobility and carrier density is only possible when this frequency resolved spectra fit with appropriate conductivity model. Herein, I present a brief discussion of different conductivity models which are used in our work.

2.6.1 Drude model:

The response of free charge carriers generated upon photo-excitation can be described by the simple Drude model, proposed by Paul Drude in 1900.[11,24] The equation of motion for plasma of free charge carriers coupled with the alternating electric field, $E(t) = E_0 e^{-i\omega t}$, can be written as

$$m\frac{d^2\boldsymbol{r}}{dt^2} + m\gamma\frac{d\boldsymbol{r}}{dt} = -eE(t) \qquad (2.36)$$

Where $\boldsymbol{r}$ is the average displacement of charge carriers, m is the effective mass of the charge carriers, γ is the scattering rate (inverse of scattering time, τ) and e is the electronic charge. For a given carrier density N, the frequency dependent conductivity can be derived from the Equation 2.36 as

$$\hat{\sigma}(\omega) = \frac{\varepsilon_0 \omega_p^2 \tau}{1 - i\omega\tau} = \frac{\sigma_{DC}}{1 - i\omega\tau} \qquad (2.37)$$

By fitting experimental conductivity to the Equation 2.37, one can calculate the carrier density (N) and mobility (μ) from the plasma frequency (ω_p) and scattering time (τ) as follows

$$N = \frac{\varepsilon_0 \omega_p^2 m}{e^2} \qquad (2.38)$$

$$\mu = \frac{e\tau}{m} \qquad (2.39)$$

Although this model did not include electron-electron and electron-lattice scatterings, it was successfully employed to derive the carrier density and mobilities in the case of bulk and quantum confined semiconductors.[11,25-29] However, this model cannot be applied 1) when there is a distribution of scattering times present,[30] 2) disordered materials,[14,23] and 3) when carriers are localized due to trap states or from backscattering from the surface.[31-36]

2.6.2 Drude-Smith model:

A modification to the Drude conductivity model based on impulse current and Poisson statistics, by incorporating persistence of velocity constant, c_n, was proposed by smith and is given by[31]

$$\hat{\sigma}(\omega) = \frac{\varepsilon_0 \omega_p^2 \tau}{1 - i\omega\tau}\left[1 + \sum_{n=1}^{\infty} \frac{c_n}{(1 - i\omega\tau)^n}\right] \tag{2.40}$$

In practice, the Equation is truncated to the first scattering event. Here c_n represents the fraction of electrons having the initial velocity after nth collision. This model has been successfully employed to understand the nature of conductivity in materials where localization of charge carriers takes place due to the presence of defects or grain boundaries and disorder,[32,37,38] such as in perovskites.[14,23] However, this model has undergone some criticism for not being physical i.e. in micro meter size particle the backscattering of carriers from the surface is negligible since carrier diffusion length is on picoseconds, so one would not expect Drude-Smith behaviour.[39]

2.6.3 Lorentz oscillator model:

The resonance features in the conductivity spectrum may originate due to the various phenomenon and can be modeled by the Lorentz oscillator model.[39] The equation of motion for a charged particle in an electric filed subjected to restoring force takes the form of the simple damped harmonic oscillator and is given by the following expression.

$$m\frac{d^2\boldsymbol{r}}{dt^2} + m\gamma\frac{d\boldsymbol{r}}{dt} + m\omega_0^2\boldsymbol{r} = -eE(t) \tag{2.41}$$

The conductivity derived from solving this equation will be

$$\hat{\sigma}(\omega) = \frac{\varepsilon_0 \omega_p^2 \tau\omega}{\omega - i\tau(\omega^2 - \omega_0^2)} \tag{2.42}$$

where ω_0 is the oscillator resonance frequency and $1/\tau$ $(=\gamma)$ is the linewidth of the resonance. This model has been successful in explaining the plasmon resonance in micro sized particles, nanowires and phonon resonances in nanocrystals.[39-42] The exemplary plots, for all these three models at various scattering times, at various C values and at resonance frequency at 10 THz, are given in Figure 2.6.

It is also a common practice in literature to use superposition of conductivity models to understand the nature of conductivity spectrum in THz region.[41-44]

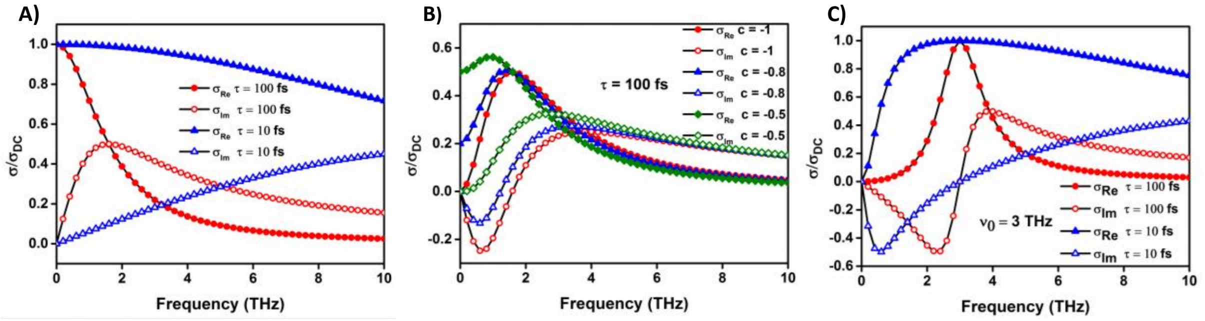

Figure 2.6: Exemplary plots of Drude model at scattering times of 100 fs and 10 fs (A), Drude-Smith model at various C values (B) and Lorentz-oscillator model at 100 fs and 10 fs and at resonance frequency 3 THz (C).

2.7 References:

(1) Xie, X.; Dai, J.; Zhang, X. C. *Phys. Rev. Lett.* **2006**, *96*, 075005.
(2) Dai, J.; Xie, X.; Zhang, X. C. *Phys. Rev. Lett.* **2006**, *97*, 103903.
(3) Karpowicz, N.; Dai, J.; Lu, X.; Chen, Y.; Yamaguchi, M.; Zhao, H.; Zhang, X. C.; Zhang, L.; Zhang, C.; Price-Gallagher, M.; Fletcher, C.; Mamer, O.; Lesimple, A.; Johnson, K. *Appl. Phys. Lett.* **2008**, *92*, 011131.
(4) Hamster, H.; Sullivan, A.; Gordon, S.; White, W.; Falcone, R. W. *Phys. Rev. Lett.* **1993**, *71*, 2725.
(5) Hamster, H.; Sullivan, A.; Gordon, S.; Falcone, R. W. *Phys. Rev. E* **1994**, *49*, 671.
(6) Cook, D. J.; Hochstrasser, R. M. *Opt. Lett.* **2000**, *25*, 1210.
(7) Kress, M.; Löffler, T.; Eden, S.; Thomson, M.; Roskos, H. G. *Opt. Lett.* **2004**, *29*, 1120.
(8) Bartel, T.; Gaal, P.; Reimann, K.; Woerner, M.; Elsaesser, T. *Opt. Lett.* **2005**, *30*, 2805.
(9) Kim, K. Y.; Taylor, A. J.; Glownia, J. H.; Rodriguez, G. *Nat. Photon.* **2008**, *2*, 605.
(10) Kim, K. Y.; Glownia, J. H.; Taylor, A. J.; Rodriguez, G. *Opt. Express* **2007**, *15*, 4577.
(11) Ulbricht, R.; Hendry, E.; Shan, J.; Heinz, T. F.; Bonn, M. *Rev. Mod. Phys.* **2011**, *83*, 543.
(12) Knoesel, E.; Bonn, M.; Shan, J.; Wang, F.; Heinz, T. F. *J. Chem. Phys.* **2004**, *121*, 394.
(13) Knoesel, E.; Bonn, M.; Shan, J.; Heinz, T. F. *Phys. Rev. Lett.* **2001**, *86*, 340.

(14) La-o-vorakiat, C.; Salim, T.; Kadro, J.; Khuc, M.-T.; Haselsberger, R.; Cheng, L.; Xia, H.; Gurzadyan, G. G.; Su, H.; Lam, Y. M.; Marcus, R. A.; Michel-Beyerle, M.-E.; Chia, E. E. M. *Nat. Commun.* **2015**, *6*, 7903.
(15) Nienhuys, H.-K.; Sundström, V. *Phys. Rev. B* **2005**, *71*, 235110.
(16) Jepsen, P. U.; Cooke, D. G.; Koch, M. *Laser Photonics Rev.* **2011**, *5*, 124.
(17) Scheller, M.; Jansen, C.; Koch, M. In *Recent Optical and Photonic Technologies*; Kim, K. Y., Ed.; InTech: Rijeka, 2010, p Ch. 12.
(18) Kužel, P.; Němec, H. *J. Phys. D: Appl. Phys.* **2014**, *47*, 374005.
(19) Garnett, J. C. M. *Philosophical Transactions of the Royal Society of London. Series A,* **1904**, *203*, 385.
(20) Bruggeman, D. A. G. *Annalen der Physik* **1935**, *416*, 636.
(21) Han, J.; Zhang, W.; Chen, W.; Thamizhmani, L.; Azad, A. K.; Zhu, Z. *J. Phys. Chem. B* **2006**, *110*, 1989.
(22) Mandal, P. K.; Chikan, V. *Nano Lett.* **2007**, *7*, 2521.
(23) Yettapu, G. R.; Talukdar, D.; Sarkar, S.; Swarnkar, A.; Nag, A.; Ghosh, P.; Mandal, P. *Nano Lett.* **2016**, *16*, 4838.
(24) W., A. N.; David, M. N. *Solid state physics*; Thomson, 1976.
(25) Karakus, M.; Jensen, S. A.; D'Angelo, F.; Turchinovich, D.; Bonn, M.; Cánovas, E. *J. Phys. Chem. Lett.* **2015**, *6*, 4991.
(26) Wehrenfennig, C.; Liu, M.; Snaith, H. J.; Johnston, M. B.; Herz, L. M. *Energy Environ. Sci.* **2014**, *7*, 2269.
(27) Beard, M. C.; Turner, G. M.; Schmuttenmaer, C. A. *Nano Lett.* **2002**, *2*, 983.
(28) Rehman, W.; Milot, R. L.; Eperon, G. E.; Wehrenfennig, C.; Boland, J. L.; Snaith, H. J.; Johnston, M. B.; Herz, L. M. *Adv. Mater.* **2015**, *27*, 7938.
(29) Wehrenfennig, C.; Eperon, G. E.; Johnston, M. B.; Snaith, H. J.; Herz, L. M. *Adv. Mater.* **2014**, *26*, 1584.
(30) Jeon, T.-I.; Grischkowsky, D. *Phys. Rev. Lett.* **1997**, *78*, 1106.
(31) Smith, N. V. *Phys. Rev. B* **2001**, *64*, 155106.
(32) Turner, G. M.; Beard, M. C.; Schmuttenmaer, C. A. *J. Phys. Chem. B* **2002**, *106*, 11716.
(33) Beard, M. C.; Turner, G. M.; Murphy, J. E.; Micic, O. I.; Hanna, M. C.; Nozik, A. J.; Schmuttenmaer, C. A. *Nano Lett.* **2003**, *3*, 1695.
(34) Hendry, E.; Schins, J. M.; Candeias, L. P.; Siebbeles, L. D. A.; Bonn, M. *Phys. Rev. Lett.* **2004**, *92*, 196601.
(35) Hendry, E.; Koeberg, M.; Schins, J. M.; Nienhuys, H. K.; Sundström, V.; Siebbeles, L. D. A.; Bonn, M. *Phys. Rev. B* **2005**, *71*, 125201.
(36) Kim, J.; Maeng, I.; Jung, J.; Song, H.; Son, J.-H.; Kim, K.; Lee, J.; Kim, C.-H.; Chae, G.; Jun, M.; Hwang, Y.; Jeong Lee, S.; Myoung, J.-M.; Choi, H. *Appl. Phys. Lett.* **2013**, *102*, 011109.
(37) Ai, X.; Beard, M. C.; Knutsen, K. P.; Shaheen, S. E.; Rumbles, G.; Ellingson, R. J. *J. Phys. Chem. B* **2006**, *110*, 25462.
(38) Baxter, J. B.; Guglietta, G. W. *Anal. Chem.* **2011**, *83*, 4342.
(39) Nienhuys, H.-K.; Sundström, V. *Appl. Phys. Lett.* **2005**, *87*, 012101.
(40) Joyce, H. J.; Baig, S. A.; Parkinson, P.; Davies, C. L.; Boland, J. L.; Tan, H. H.; Jagadish, C.; Herz, L. M.; Johnston, M. B. *J. Phys. D Appl. Phys.* **2017**, *50*, 224001.
(41) Sarkar, S.; Ravi, V. K.; Banerjee, S.; Yettapu, G. R.; Markad, G. B.; Nag, A.; Mandal, P. *Nano Lett.* **2017**, *17*, 5402.
(42) Ziwritsch, M.; Müller, S.; Hempel, H.; Unold, T.; Abdi, F. F.; van de Krol, R.; Friedrich, D.; Eichberger, R. *ACS Energy Lett.* **2016**, *1*, 888.
(43) Kar, S.; Jayanthi, S.; Freysz, E.; Sood, A. K. *Carbon* **2014**, *80*, 762.

(44) Parkinson, P.; Joyce, H. J.; Gao, Q.; Tan, H. H.; Zhang, X.; Zou, J.; Jagadish, C.; Herz, L. M.; Johnston, M. B. *Nano Lett.* **2009**, *9*, 3349.

Chapter 3

Terahertz Conductivity within Colloidal $CsPbBr_3$ Perovskite Nanocrystals

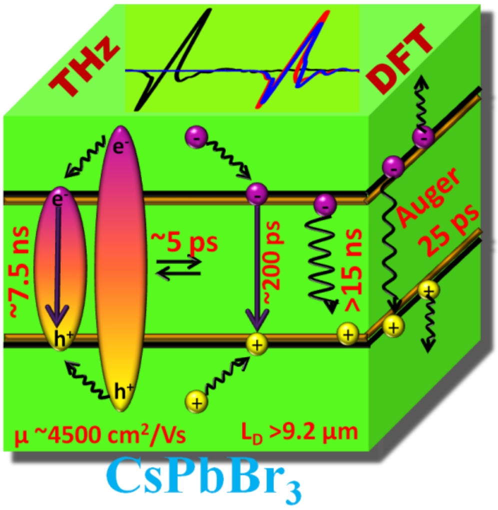

3.1 Introduction:

Hybrid organic-inorganic perovskites (HOIP), with a chemical formula of $CH_3NH_3MX_{3-n}Y_n$ (M = Pb, Sn; X, Y = Cl, Br, I), have recently emerged as one of the most sought-after materials for solar cell applications.[1-10] In a short span of time the power conversion (solar cell) efficiency employing these materials has reached encouragingly high value (~22.1%)[11] and is most likely to increase further in near future. These hybrid perovskites also exhibit promises for other optoelectronic applications such as light emitting diodes (LEDs) and photodetectors.[12,13] Motivated by this success of hybrid perovskite films, another class of perovskite materials, namely, colloidal all-inorganic $CsPbX_3$ (X = Cl, Br, I) nanocrystals (NCs) have been reported by Kovalenko and co-workers in the year 2015.[14] From the perspective of possible applications as devices, these NCs are also gifted with several desirable properties, such as extremely high (>80%) fluorescence quantum yield (QY), very narrow emission bandwidth (~85 meV), reduced fluorescence blinking, and low threshold (~5 $\mu J/cm^2$) lasing capability.[14-18] Utilizing this unique combination of luminescence properties, efficient LEDs with high color purity have already been demonstrated using these NCs.[19]

Clearly, both HOIP films and colloidal $CsPbX_3$ (X = Cl, Br, I) NCs exhibit extraordinary semiconductor quality, even though they are prepared employing low-temperature solution-based methodology. However, the understanding of fundamental physics behind such amazing properties is still evolving.[20-24] Several forms of time-resolved (ultrafast to ultraslow) spectroscopic studies have been instrumental for such a cause. Time-resolved terahertz (THz) spectroscopy (TRTS), also known as optical pump THz probe (OPTP) spectroscopy has played a significant role in evaluating the photophysical properties of HOIP films such as photoconductivity, carrier density, carrier mobility, diffusion length, and their temporal evolution after photoexcitaion.[25-32] The results of the above studies indicate a smaller density of defect states as the main reason for such good semiconductor properties in these films. However, in the case of $CsPbX_3$ NCs, a large density of surface defects is expected because of the large surface to volume ratio owing to the small size of NCs. Thus high fluorescence QY of $CsPbX_3$ NCs is counter-intuitive. Attempts to understand the carrier dynamics and lasing mechanisms in $CsPbBr_3$ NCs have just begun, and a few ultrafast and single NC spectroscopic studies have been reported very recently.[33-39] However, the intrinsic semiconducting parameters such as carrier mobility, diffusion length, and their temporal evolution are still unknown, even though these provide guidelines to achieve desired optoelectronic properties. Further, as these properties are highly sensitive to trap states, it is desirable to study them in order to understand the role of defects in a given semiconducting material.[40]

In this report, we employed TRTS, for the first time, to elucidate above mentioned semiconductor properties intrinsic to $CsPbBr_3$ NCs. We probed transient photoconductivity within the $CsPbBr_3$ NCs to monitor sub-ps to ns carrier dynamics and tried to unravel their recombination mechanism. TRTS probes the frequency averaged and frequency-resolved photoconductivity of the NCs without any electrical connection.[41-44] The time-resolved results reveal threefold carrier recombination mechanisms, namely an inefficient monomolecular trap-assisted recombination, bimolecular electron-hole recombination and fast third order Auger recombination. This inefficient trap-assisted recombination suggests the absence of surface defects at the mid-gap region, which, in turn, results into remarkably high carrier mobility (~4500 $cm^2V^{-1}s^{-1}$) and diffusion length in microns for $CsPbBr_3$ NCs. These properties of colloidal $CsPbBr_3$ NCs are comparable to the best quality bulk single crystalline semiconductors.[5,45]

3.2 Experimental Section:

Synthesis and characterization of colloidal $CsPbBr_3$ nanocrystals:

The complete synthesis and characterization of $CsPbBr_3$ NCs were done by Abhishek Swarnkar and Vikas K Ravi from Dr. Angshuman Nag's Lab. The colloidal $CsPbBr_3$ NCs were synthesized following the procedure given by Protesescu *et al*.[14]

Preparation of Cs-oleate Precursor: Cesium carbonate (0.4 g), Oleic acid (1.25 mL) and Octadecene (20 mL) were added into a 50 mL three neck round bottom (RB) flask. The mixture was dried under vacuum for 1 hour at 120°C. Further, the temperature was raised to 150°C and kept until the solution became clear.

3.2.1 Synthesis of $CsPbBr_3$ Colloidal NCs:

Lead bromide (0.188 mmol) and 1-Octadecene (5 mL) were mixed in 50 mL RB and dried the mixture under vacuum for 1 hour. Then anhydrous oleylamine (0.5mL) and oleic acid (0.5mL) were added to the mixture at 120°C. After the solution became clear, the temperature was increased to 190°C and pre-heated Cs-oleate solution (0.1M, 0.4 mL) was swiftly injected into the reaction mixture. The reaction was quenched after 5 seconds to arrest the growth of NCs by an ice-water bath. The as-synthesized $CsPbBr_3$ NCs were precipitated by adding n-butanol and centrifuging the mixture at 10000 rpm for 10 minutes. The precipitate was then re-dispersed in toluene to form a long-term colloidal stable solution.

3.2.2 Sample Preparation for THz Experiments:

Colloidal $CsPbBr_3$ NCs were dissolved in 2,2,4,4,6,8,8-heptamethylnonane (HMN) solvent, which is quite transparent in the broadband THz region. The solution is then injected into the demountable liquid cell (Harrick Scientific Products, DLC-M25), in which two TPX windows were placed and separated by a Teflon spacer of 950 μm thickness. The path length of the sample is equal to the spacer thickness.

3.2.3 Characterization:

UV-visible absorption spectrum was recorded by using a Perkin Elmer, Lambda-45 UV /Vis spectrometer. Steady-state photoluminescence (PL) of the NCs was measured by FLS 980 (Edinburgh Instruments).

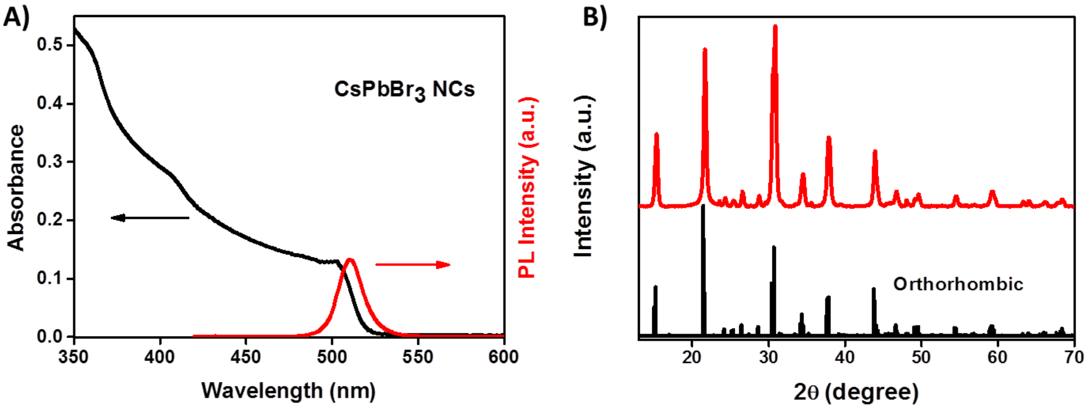

Figure 3.1: A) UV-visible, photoluminescence and B) PXRD spectra of $CsPbBr_3$ NCs

Powder X-ray diffraction (XRD) data were recorded by a Bruker D8 Advance X-ray diffractometer using Cu Kα radiation (1.54 Å).

Transmission electron microscopy (TEM) studies were carried out using a JEOL JEM 2100 F field emission transmission electron microscope at 200 kV. The sample preparation for TEM was done by putting a drop of the colloidal solution of NCs in hexane on the carbon-coated copper grids.

The synthesized NCs exhibit cube-like morphology (see Figure 3.6.A) with ~11 nm edge dimension and an orthorhombic crystal structure.[17] The lowest energy excitonic absorption is at 504 nm (2.46 eV) along with an excitonic PL at 514 nm. Interestingly, the PL quantum yield is ~80% without doing any surface modification, along with a narrow spectral width of ~85 meV. These PL behaviours are indeed unique and advantageous compared to traditional colloidal quantum dots like CdSe based ones.[18]

3.3 THz time-domain spectroscopy (THz-TDS) and OPTP measurements:

Broadband THz probe in the range of 0.5 to 7 THz has been employed in the present study. The spectrometer is based on an ultrafast (~50 fs) amplified laser system, and uses air plasma for generation and coherent detection of THz light.[44,46] We measured THz- time-domain spectra (THz-TDS) and OPTP spectra of the $CsPbBr_3$ NCs dispersed in HMN at room temperature. The THz transmission was recorded at a precise delay after exciting the NCs with an optical pump pulse having energy equal to or more than the band gap of the NCs. The pump-induced change in THz transmission ($-\Delta E(t_p)$) and the corresponding THz transmission through the non-photoexcited NCs ($E_0(t_p)$) were recorded simultaneously using double lock-in technique.[47] All THz-TDS and OPTP measurements were recorded using a liquid sample cell with two TPX windows of 2 mm thickness and a spacer thickness (path length) of 950 μm. This allows us to study the frequency dependent photoconductivity till 5 THz whereas most OPTP studies are limited to 2.5 THz.[43] The NCs were excited with three different pump wavelengths, 504 (2.46 eV), 480 (2.58 eV) and 400 (3.1 eV) nm, for studying the photo-generated carrier dynamics. The NC solution had an optical density (OD) of 0.83, 0.89 and 1.83 at the pump wavelength 504, 480 and 400 nm respectively. The optical pump and the THz probe beam diameters were ~3.5 mm and ~1.0 mm respectively.

The THz frequency averaged photoconductivity transients were recorded fixing the sampling delay (delay 1 in Figure 2.3. in Chapter 2) at the peak of the THz electric field and scanning the delay (delay 3 in Figure 2.3. in Chapter 2) between the optical pump and THz probe pulses. Alternatively, the photoinduced time-domain THz transmission spectra $\Delta E(t, t_p)$ were recorded at different pump-probe delay (t_p) after photoexcitation with 400 nm pump having fluence of 57 and 94 μJ/cm^2, and with 480 nm pump having fluence of 73 and 166 μJ/cm^2. The frequency domain complex photo-conductivities ($\Delta\sigma_1(\omega) + i\,\Delta\sigma_2(\omega)$) were calculated from the time domain spectra following the method developed by Heinz and co-workers.[48,49] The details of our experimental setup, experimental procedure, and analysis of THz-TDS and OPTP data can be found in Chapter 2.

3.4 Computational details:

All computational studies documented here were carried out by Debnath Talukdar under the supervision of Dr. Prasenjit Ghosh of IISER, Pune. To get better insights, they are included in this thesis.

First-principles density functional theory based calculations have been performed using the Quantum ESPRESSO suite of codes.[50] The electron-ion interactions were described by ultrasoft pseudopotentials.[51] Pb being a heavy element shows strong spin-orbit interactions (SOI). It has been shown that for lead halide perovskites it is important to include the SOI explicitly in the calculation of its electronic structure.[52] To correctly account for this, we have solved the relativistic Kohn-Sham equations self consistently[53,54] using fully-relativistic ultrasoft pseudopotentials for all the elements.[55] The electron-electron exchange-correlation functional has been described using the Perdew-Burke-Ernzerhof (PBE) parametrization of the generalized gradient approximation (GGA).[56] Brillouin zone (BZ) integrations were done with an 8×6×8 Monkhorst-Pack k-point mesh.[57] Recently it has been shown that large polarizability of the halogen atoms induces significant van der Waals interaction in the halide octahedron[58,59], which makes it necessary to include these interactions to reliably predict structural parameters in these systems. Since in conventional PBE-GGA based exchange-correlation functionals van der Waals interaction is not included, we have used Grimme's empirical van der Waals correction to the DFT total energy.[60,61] We note that this form of correction only affects the binding energy (and geometry) and does not explicitly affect the electronic structure of the system. Since the electronic structure is affected by the geometry, the effect of dispersion is implicitly incorporated in the electronic structure. The phonons at the zone center and the dielectric constant of orthorhombic bulk $CsPbBr_3$ were calculated using the linear response density functional perturbation theory (DFPT).[62] The details of the calculations of the effective mass, exciton binding energies and Bohr exciton radius are given below.

3.4.1 Calculation of effective mass, exciton binding energy, and Bohr exciton radius:

Based on the assumption that in this material the excitons are Wannier type excitons, according to the effective mass theory the Bohr exciton radius is given by:

$$a_0 = \frac{\epsilon a_0^H}{\mu}, \qquad (3.1)$$

and the exciton binding energy is given by:

$$E_b = 13.6\frac{\mu}{\epsilon^2} \qquad (3.2)$$

In Eqn. (3.1) and (3.2), ϵ is the dielectric constant, a_0^H is the radius of Hydrogen atom and μ is the reduced mass of the exciton. The reduced mass is given by $\frac{1}{\mu} = \frac{1}{m_e^*} + \frac{1}{m_h^*}$, m_e^*, m_h^* being the effective masses of electron and hole respectively. Since the photoconductivity measured is obtained from averaging along x, y and z direction, we consider the conductivity effective masses$\left(\frac{1}{m^{C*}} = \frac{1}{3}\left(\frac{1}{m_{100}^*} + \frac{1}{m_{010}^*} + \frac{1}{m_{001}^*}\right)\right)$. The effective masses of electrons and holes along the [100], [010] and [001] directions are determined by fitting the band structure (within k_BT of band edges) at the valence band maximum (VBM) and conduction band minimum (CBM) at Γ point.

Determining the correct values of Bohr exciton radius (equation 3.1) and exciton binding energy (equation 3.2) are challenging because the dielectric constant (ϵ) shows large variation with frequency and temperature. The correct choice of ϵ depends on the exciton binding energy (which itself is unknown) and the energy of the optical phonons.[32] Hence we have given estimates for the upper and lower limits of the exciton binding energy and Bohr exciton radius by computing them using values of the dielectric constant in the high frequency limit (ϵ_∞) and in the static (ϵ_s) limit. ϵ_s is given by:

$$\epsilon_s = \epsilon_\infty + \frac{4\pi}{V}\sum_p \frac{Z_p^2}{\nu_p^2}, \qquad (3.3)$$

where ν_p is the phonon frequency of mode p, V is the unit cell volume and Z_p is the mass-weighted mode effective Born vector. These quantities that go into the calculation of the dielectric constant of $CsPbBr_3$ are obtained from density functional perturbation theory calculations.

3.4.2 DFT calculations (effect of van der Waals interaction):

3.4.2.A Structure:

For orthorhombic bulk $CsPbBr_3$, within the GGA approximation, we obtain the lattice parameters a, b and c to be 8.52, 12.10, and 8.55 Å. In comparison to the experimental values, the lattice parameters are overestimated by 3-4 %, resulting in about 11% overestimation in the unit cell volume. On including the van der Waals (vdW) interaction, we find the lattice parameters b and c are significantly reduced to 11.89 and 7.56 Å while a remains unchanged. This results in about 3.3% compression in the unit cell volume compared to the experimentally measured one. In addition to the lattice parameters, the in-plane and apical Pb-Br bond lengths and Pb-Br-Pb angles are shortened on the inclusion of the vdW interaction. A comparison of the structural parameters obtained from calculations with GGA and GGA+vdW with the experimental ones are given in Fig. 3.2.A and B.

3.4.2.B Phonons and dielectric constant:

Consistent with the overall compression in the structural parameters on the inclusion of vdW interactions, we find that the phonon modes are stiffened. Fig. 3.3 shows the computed IR spectra with and without vdW. We observe vdW interactions result in an overall shift of the phonon modes towards the high-frequency side because of the stiffening of the bonds and compression of the unit cell. This effect is further reflected when we calculate the static dielectric constant. Though we find similar values for ϵ_∞ with (4.0) and without (4.14) vdW, the static dielectric constants reduces to almost half of the value we obtain with GGA. While with GGA the static dielectric constant is 30.79, after incorporating vdW interactions, we obtain $\epsilon_s = 15.61$. We find that this value of dielectric constant is very similar to what is obtained for bulk $CsPbCl_3$, measured at room temperature at $10^5 - 10^6$ Hz.[63] This suggests that it is indeed important to incorporate vdW interactions in order to compute the structure and electronic properties of lead halides. A detailed analysis of the phonon frequencies, born effective charges and effective plasma frequencies of the phonon modes indicate that the large ionic contribution to the static dielectric constant in absence of vdW results primarily from the overall softening (low phonon frequencies) of the phonon modes.

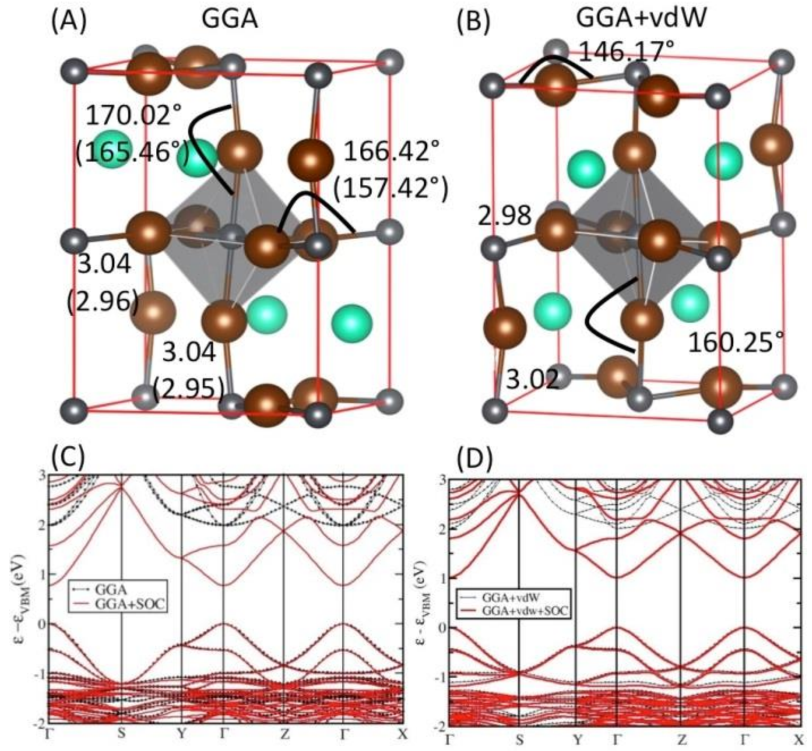

Figure 3.2: Structure of orthorhombic bulk $CsPbBr_3$ with (A) GGA and with (B) GGA+vdW. The Pb-Br computed (experimental) bond lengths are given in Å. The angles made by the axis of two octahedra along the b direction and in the ac plane are also shown. The electronic structure (with and without SOC) along the high symmetry directions of the BZ for (C) GGA and (D) GGA+vdW. The brown, black and green spheres represent Br, Pb and Cs atoms respectively.

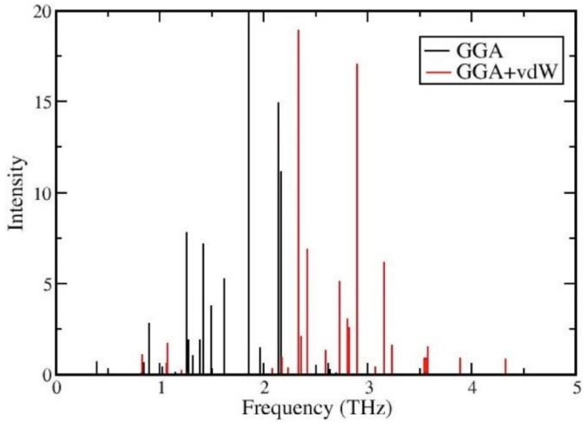

Figure 3.3: Computed IR spectra with (red lines) and without (black lines) vdW showing an overall shift in the phonon frequencies due to the strengthening of bonds on the inclusion of vdW interactions.

3.4.2.C Electronic structure:

Van der Waals interactions also affect the electronic properties of the system implicitly through the change in structure. Fig. 3.3, (C and D) show the band dispersion with and without vdW. In order to highlight the importance of spin-orbit coupling (SOC), we have also included the band structure without spin-orbit coupling for both the cases. A comparison of the red curves in Fig. 3.3 (C and D) shows that vdW reduces the dispersion of the bands, thereby making them flatter. This results in larger effective masses for both electrons and holes at the Γ-point of the Brillouin zone. The effective masses for both the cases are listed in table 1. Additionally, there is also an increase in the band gap (1.01 eV with vdW+GGA compared to 0.76 eV with GGA). In both the cases, we find a SOC splitting of about 0.81 eV. The isosurfaces of the wavefunction corresponding to the VBM and CBM with vdW interaction are shown in Figure 3.4. C and D respectively.

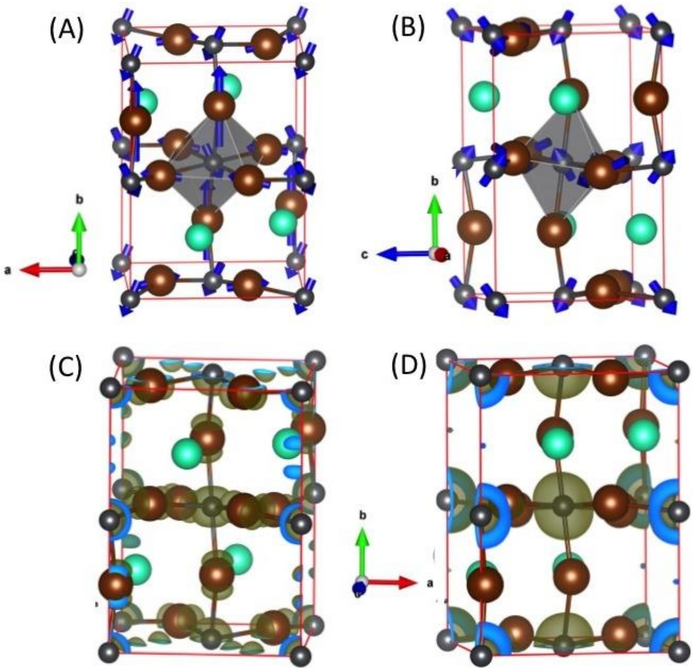

Figure 3.4: (A) and (B) shows the displacement patterns (denoted by blue arrows) corresponding to the two peaks in the computed spectra at 2.33 and 2.9 THz in Fig. 3.6.D. Contribution to the charge density from the valence band maxima (C) and conduction band minima (D) at Γ point of the BZ.

Table 3.1: Effective masses of electrons and holes along the three high symmetric directions and the conductivity effective mass. The numbers in parenthesis are those obtained without the inclusion of van der Waals interaction.

Direction	m_e^*	m_h^*
[100]	0.24 (0.15)	0.26 (0.16)
[010]	0.17 (0.14)	0.20 (0.15)
[001]	0.27 (0.15)	0.26 (0.15)
Conductivity effective mass	0.22 (0.15)	0.24 (0.15)

3.4.2.D Exciton binding energies and Bohr exciton radius:

Using ϵ_{∞}, the exciton binding energies with and without vdW interactions are 90 and 64 meV respectively. The higher exciton binding energy upon the inclusion of vdW can be attributed to the increase in the electron and hole effective masses, which in turn increases the exciton mass to 0.113 from 0.075 (with only GGA). Using the static value of the dielectric constant we find the exciton binding energies to be 6.0 and 1.1 meV with and without vdW respectively.

Our calculations predict that within GGA the Bohr exciton radius will lie between 28.21 (with ϵ_{∞}) and 217.17 Å (with ϵ_0), depending on the value of the dielectric constant. On inclusion of vdW, we find that the lower and upper limit of the Bohr exciton radius reduces to 19.39 and 73.08 Å respectively.

Table 3.2: Effect of van der Waals interaction and choice of dielectric constant in the calculation of Bohr exciton radius and exciton binding energies. The numbers in parenthesis are computed with static dielectric constant.

Property	Level of theory	
	GGA	vdW + GGA
Bohr exciton radius (Å)	28.21 (217.17)	19.39 (73.08)
Exciton binding energy (meV)	64.0 (1.1)	90.0 (6.0)

3.5 Results and Discussion:

3.5.1 Phonons in non-photoexcited NCs:

The time domain THz waveforms, transmitted through the empty sample cell, and that filled with HMN (solvent), and the NC solution are shown in Figure 3.6.B. The amplitude, shape and relative phase of the time domain spectrum of the NC solution is different from that of solvent (highlighted in the inset of Figure 3.6.B) mainly due to absorption and dispersion by the NCs. Prior to the calculation of absorbance and complex dielectric function of NCs, we have measured absorbance, real refractive indices and complex dielectric functions of HMN and NC solution, and are given in Figure 3.5.

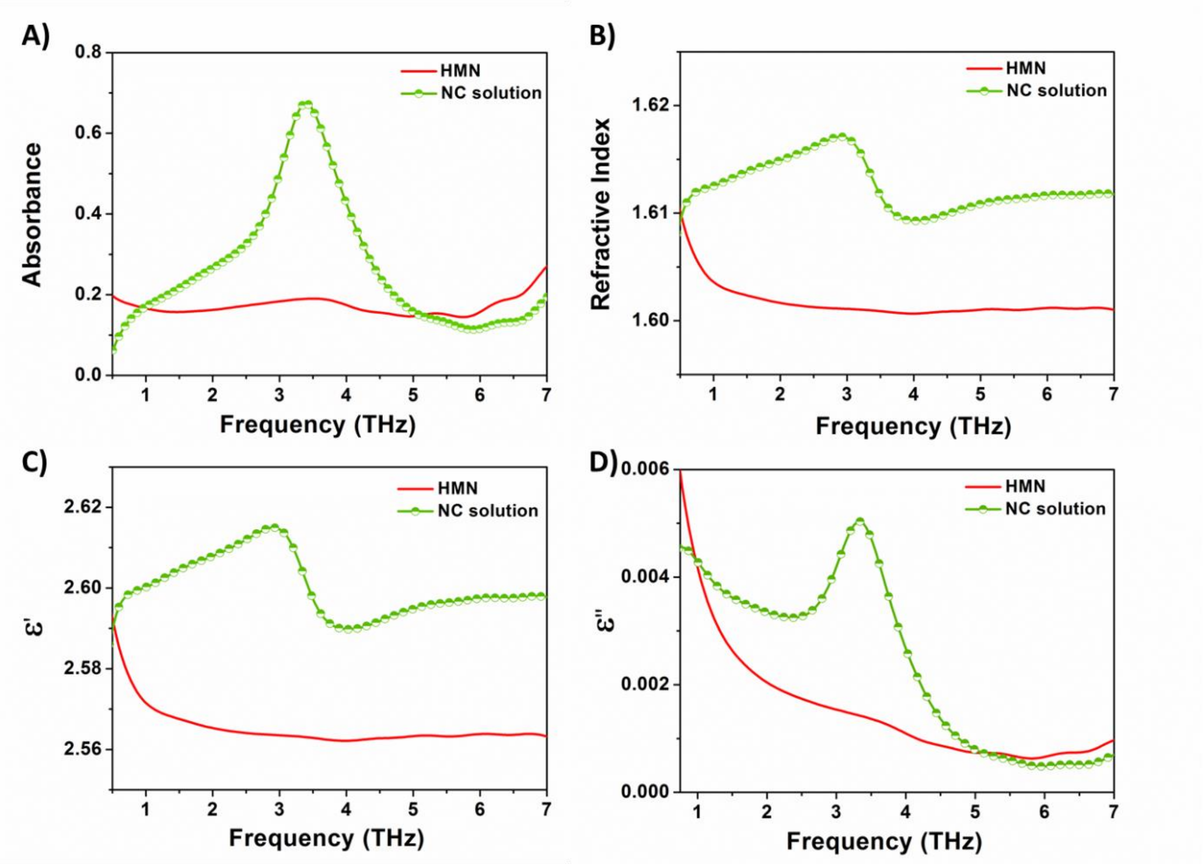

Figure 3.5: THz absorption (A), refractive indices (B), real (C), and imaginary (D) dielectric functions of HMN solvent (Red solid line) and the CsPbBr$_3$ perovskite NC solution (Fluorescent green line).

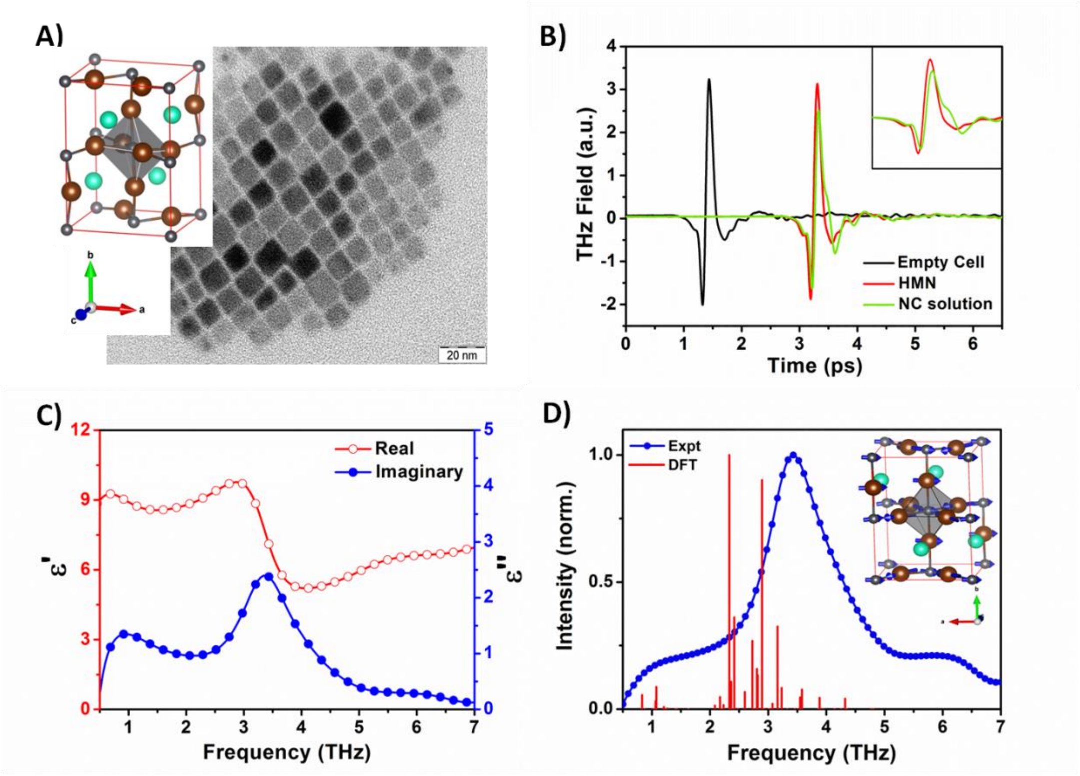

Figure 3.6. A) TEM image of synthesized $CsPbBr_3$ NCs. The inset shows the orthorhombic crystal structure obtained from DFT calculation (GGA+vdW) on the bulk crystal. B) THz-TDS waveforms transmitted through the empty sample cell (black), solvent (red) and the NC solution (fluorescent green), C) Intrinsic real (open circles) and imaginary (solid circles) parts of the frequency dependent dielectric functions of NCs obtained from the effective medium analysis, D) Normalized THz-TDS absorption spectrum (blue solid circles) of NCs and optical phonon intensities (red sticks) from DFT calculation.

Figure 3.6.C shows the intrinsic frequency dependent complex dielectric function of the NCs calculated using a simple linear effective medium approach (EMA) for dielectric inclusion embedded in a host medium.[64] Adopting simple EMA in the present work is due to the following reasons: (1) the size of the inclusions (nanocrystals, ~11 nm) is significantly less than the wavelength of the probe light (0.5 to 7 THz, 150 to 2100 μm), (2) the volume fraction is very small ($\sim 10^{-3}$) making the Bruggeman method inapplicable, this being used for very large volume fraction where inclusions come together and form domains; moreover linear EMA seems to be working reasonably well for such dilute solution,[7] and (3) the NCs of this study have a cubic/orthorhombic geometry and the geometry factor for cubic/orthorhombic structure required for Maxwell-Garnet method is not known and determining the same is beyond the scope of the present work. The real dielectric constant varies between 5 and 10 in the frequency

range of 0.5 to 7 THz (17 to 233 cm^{-1}). We note that this lies within the theoretical estimates of the lower (high frequency optical dielectric constant, $\varepsilon_\infty = 4.14$) and upper limits (static dielectric constant, $\epsilon_S = 15.6$) of the dielectric constants predicted from our first principles calculations (GGA+vdW).

The absorbance of NCs was obtained by subtracting the absorbance of the NC solution with the absorbance of HMN solvent. The THz absorption spectrum of the NCs (see Figure 3.6.D) shows a broad strong absorption band with a peak at ~3.4 THz (115 cm^{-1}). In addition, there are two small shoulders at ~1 THz (33 cm^{-1}) and 6 THz (~200 cm^{-1}). The absorption features observed are due to infrared (IR) active lattice vibrations (optical phonons) of the orthorhombic lattice of the NCs. In order to understand the nature of the phonon modes, we have computed the IR spectra. Figure 3.6.D shows the computed spectrum along with the THz absorption spectrum. We observe that the computed modes are softer compared to the experimental ones. This can be attributed to the fact that (a) the computed Pb-Br bond lengths and the *a* and *b* values of the lattice parameters of the orthorhombic bulk unit cell are larger than the experimental ones, given in figure 3.2.A and 3.2.B, and (b) the experiments are done on NCs where one would expect slight stiffening of the bonds due to reduced coordination of the surface atoms, thereby resulting in higher frequencies of the phonon modes. In the computed spectrum we observe two strong IR peaks at 2.33 THz and 2.90 THz with a couple of low-intensity peaks in between. We assign these two modes to the peak of the experimental spectrum. The low resolution of the apparatus does not allow us to resolve the modes. All these modes between 2.33 and 2.90 THz are primarily associated with the vibrations of the $PbBr_6$ octahedron. The displacement pattern due to the peaks at 2.33 THz and 2.90 THz are given in Fig. 3.4 (A) and (B) respectively. The optical phonon mode at 2.33 THz involves motion of all the Br and Pb atoms in the octahedron; the dominant contribution coming from antisymmetric stretching of the apical Pb-Br bonds (perpendicular to the a-c plane). Additionally, there is also weak asymmetric stretching of the equatorial Pb-Br bonds in the $PbBr_6$ octahedron. On the contrary, the displacement pattern corresponding to the phonon mode at 2.90 THz only involves the bending of the in-plane Br-Pb-Br bond angle. Very similar phonon vibrations have been reported earlier for $CsPbBr_3$ single crystal by Far IR and Raman spectral study.[65]

3.5.2 Carrier mobility from frequency averaged OPTP:

In OPTP, excitation above the bandgap produces charge carriers that absorb the THz probe light, thereby reducing the transmission. Pump light of 504 nm (equal to lowest energy excitonic absorption; see Figure 3.1.A) produces carriers with no or minimum extra energy, whereas 480 and 400 nm pumps create carriers with excess energy of ~120 meV and ~640 meV respectively. The change in THz transmission ($-\Delta E(t_p)/E_0(t_p)$) at a particular pump-probe delay (t_p) is proportional to the photoconductivity ($\Delta\sigma(t_p)$) of the medium at that moment. We would like to emphasize that in this study the photoconductivity is measured within the NCs, not across them as these are dispersed in a non-conducting medium (solvent) with a volume fraction of the order of 10^{-3}. Here we assume that the THz conductivity arises mainly from free charge carriers rather than excitons. At our experimental condition, both excitons and free charges (electrons and holes) may coexist in the photoexcited NCs, but excitons do not respond to the THz probe.[25] The efficiency of dissociation of excitons into free electrons and holes depends largely on the exciton binding energy (E_b). Calculating the E_b has its own limitation as the choice of dielectric constant in equation 3.2 depends on the value of E_b itself and the energy of the optical phonons.[32] Hence we have calculated the lower (corresponds to static dielectric constant) and upper (using high-frequency limit of dielectric constant) limits of E_b, and their values are 6.0 and 90.0 meV respectively at the GGA+vdW level of theory (Table 2). Employing the real dielectric function obtained from our THz-TDS experiment (Figure 3.6.C) yields the E_b to be ranging from 19 to 62 meV. We note that even for hybrid organic-inorganic tri-halide perovskite, $CH_3NH_3PbI_3$, a wide range of E_b values (2 to 55 meV, depending on measurement methods) were reported till it was directly and accurately measured, recently, by Miyata *et al.*, using very high field interband magneto-absorption spectroscopy.[21] The E_b value for $CH_3NH_3PbI_3$ is rather small, ~16 meV, at low temperature and even smaller (only a few meV) at room temperature.[21] So, we anticipate that the exciton binding energy in $CsPbBr_3$ NCs will be at least in the order of the thermal energy (k_BT) at room temperature (~26 meV), and assume that a significant fraction of the excitons will dissociate into free electrons and holes. Consequently, a dynamic equilibrium between the excitons and free carriers may be established after photoexcitation.[25]

Figure 3.7.A clearly shows that the photoinduced THz transmission after photoexcitation with 480 nm pump has very strong pump fluence dependence, both in terms of the maximum of THz transmission and the nature of their temporal evolutions. With increasing fluence, photoconductivity decays faster with the presence of additional decay channels. Importantly, a significant fraction of photoconductivity exists even at 1.5 ns after photoexcitation at all pump fluence. This observation is an indication of minimal contribution from trap-state in the mid-gap region and will be discussed further in the following sub-section. Figure 3.7.B compares the normalized photoinduced THz transmissions at different pump wavelengths at the early pump-probe delay. The photoconductivity reaches its peak at the time scale of 5-6 ps, which is much longer than the instrument response time (~0.3 ps). This relatively slow rise in photoconductivity is probably the signature of dissociation of excitons into free charge carrier, and the rise time is an estimation of the rate of dissociation process. The relatively faster rise in conductivity with 400 nm pump excitation probably indicates fast dissociation of excitons, given the excess energy (640 meV) available to the excitons is significantly more in this case.

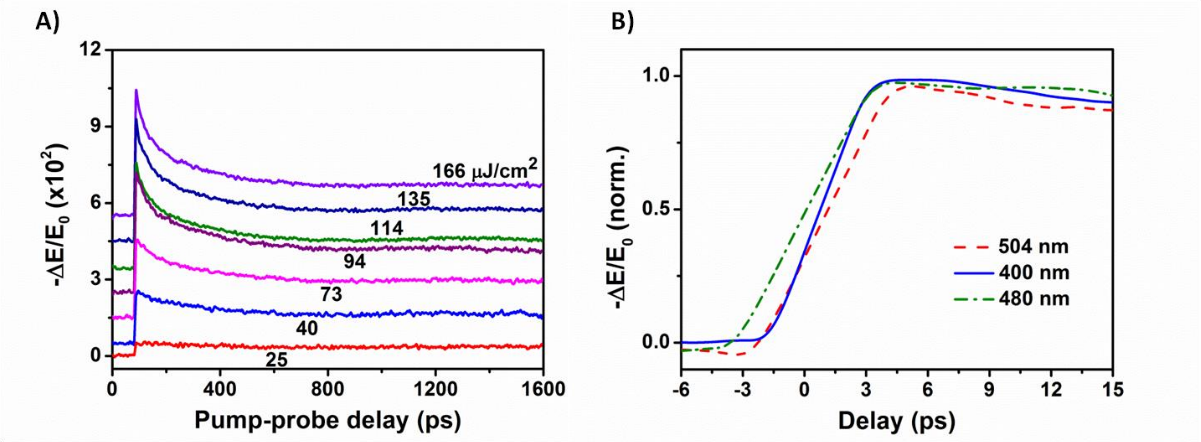

Figure 3.7.A) Frequency averaged photoinduced THz transmissions vs pump-probe delay for 480 nm pump with fluences of 25 (red), 40 (blue), 73 (magenta), 94 (purple), 114 (olive), 135 (royal blue) and 166 μJ/cm² (violet). B) Normalized photoinduced THz transmissions at early pump-probe delays for photoexcitation with 400 (94 μJ/cm², blue solid line), 480 (166 μJ/cm², green dashed-dot), and 504 (176 μJ/cm², red dash) nm pumps.

In order to estimate the initial mobility, we have calculated the peak photoconductivity of the sample from the photoinduced THz transmission according to the following equation:[66]

$$\Delta\sigma\left(t_p\right) = \frac{\varepsilon_0 c}{d}(n_a + n_b)\frac{-\Delta E(t_p)}{E_0(t_p)} \quad (3.4)$$

where ε_0 is the permittivity of free space, c is the speed of light, d is the thickness of the photoexcited sample, and n_a and n_b are the refractive indices of the media on either side of the photoexcited sample. For 504 and 480 nm pump a = b = TPX window, whereas for 400 nm pump (where the optical depth is shorter than the sample cell path length) a = TPX and b = non-photoexcited NC solution. Linear effective medium approach (Chapter 2 . Eq. x) was used to estimate the intrinsic photoconductivity of the NCs. Depending on the pump fluence, the peak photoconductivity values (intra NC) range from 84 to 230 S/m, 25 to 216 S/m and 19 to 141 S/m for the pump wavelengths of 400, 480 and 504 nm respectively. The initial carrier mobilities were calculated from the peak THz conductivities ($\Delta\sigma$) according to $\mu \cong \Delta\sigma/qN_0$, where q is the elementary charge and N_0 is the total carrier density. Both electrons and holes should contribute to the photoconductivity. On the basis of the electronic structure calculations, where we find similar values of effective masses for electrons and holes (Table 1), we hypothesize that they should have similar mobilities. Assuming that every absorbed photon results into an electron-hole pair, and photon to free carrier conversion ratio, φ = 1, we estimate the average initial carrier density ($N_0 = \varphi.2N_{ph}$) of the photoexcited NC solution (volume fraction $f = \sim 2\text{x}10^{-3}$) to be 1.1 x 10^{15} cm^{-3} to 8.0 x 10^{15} cm^{-3} depending on the pump wavelength and fluence (see Table 3.3). As the actual value of φ is not known, this method yields an effective mobility (φμ) rather than mobility (μ). The density of absorbed photon (N_{ph}) was calculated as: $N_{ph} = (F_l\,(1 - 10^{-OD_\lambda}\,))/\delta h\nu$; where F_l is the incident photon flux, $(1 - 10^{-OD_\lambda})$ is the fraction of the pump light absorbed by the sample, δ is the penetration depth, and $h\nu$ is the energy of a single photon. This gives the upper limit of N_{ph} as we ignore the reflection and scattering loss if any. The average number of photo-generated electron-hole pairs per NC varies from ~0.4 (480 nm, 25 μJcm^{-2}) to ~2.7 (504 nm, 176 μJcm^{-2}) in our experimental conditions.

The estimated initial mobilities (φμ) vary from 619 to 3275 $cm^2V^{-1}s^{-1}$, as shown in fig. 3.8, at different fluences and pump wavelengths. It should be noted that these are the lower limits of the intrinsic mobilities within a NC because, as discussed above, the carrier densities considered here are in their higher limits. These estimated carrier mobility values for colloidal $CsPbBr_3$ NCs are about one order of magnitude higher than that of $CH_3NH_3PbBr_3$ single crystal[10] and of a similar order to electron mobility value ($1000\ cm^2V^{-1}s^{-1}$) reported for bulk $CsPbBr_3$ single crystal.[65] As evident from Figure 3.8, at all pump wavelengths, the mobility initially increases with pump fluence, and then decreases at higher fluences. In general, on photoexcitation the charge carriers start filling the trap states, which are in fact low-mobility states. At reasonably high pump fluence, once all trap states are filled the charge carriers can be easily mobile in delocalized bands, increasing the mobility. However, after certain threshold carrier density carrier-carrier and carrier-lattice scattering start plying a dominating role. Hence, the mobility starts decreasing at higher pump fluence.

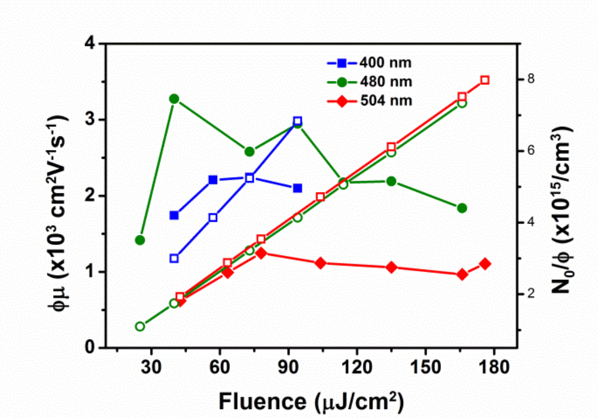

Figure 3.8: Initial effective mobility (φμ) from peak photoconductivity and carrier density (assuming $\varphi = 1$) vs. fluence at different pump wavelengths.

3.5.3. Carrier Dynamics from frequency averaged OPTP:

THz photoconductivity is proportional to the product of carrier density and carrier mobilities. Assuming that the carrier mobilities do not change significantly with the pump-probe delay (this has been verified later by frequency-resolved dynamics), the decay in THz transients essentially reflects the temporal evolution of charge carrier density after photoexcitation. In OPTP experiment THz photoconductivity may be reduced due to either the recombination of electron and hole (radiative or non-radiative) or trapping of carriers from high mobility states to low mobility states. Normalized THz transients were fit with multi-exponential decay function convoluted with a Gaussian function of the form[42]

$$y = G(t - t_0) \otimes \sum_i a_i \exp[-(t - t_0)/\tau_i\,] \qquad (3.5)$$

where $G(t - t_0)$ is a Gaussian function centered at t_0 with FWHM of ~300 fs which represents the instrument response time of our OPTP experiment, and a_i is the coefficient of the i^{th} exponential decay channel with a time constant τ_i.

Fitted THz transients at different fluences for 400, 480 and 504 nm pumps are given in Figure 3.9.A, B, and C respectively and time constants and their contributions are given in Table 3. Carrier relaxation dynamics are strongly fluence dependent for 400 and 480 nm pumps, but quite insensitive to pump fluence in case of 504 nm pump. Irrespective of the pump wavelength and fluence, the carrier decay curves become completely flat beyond ~500 ps.

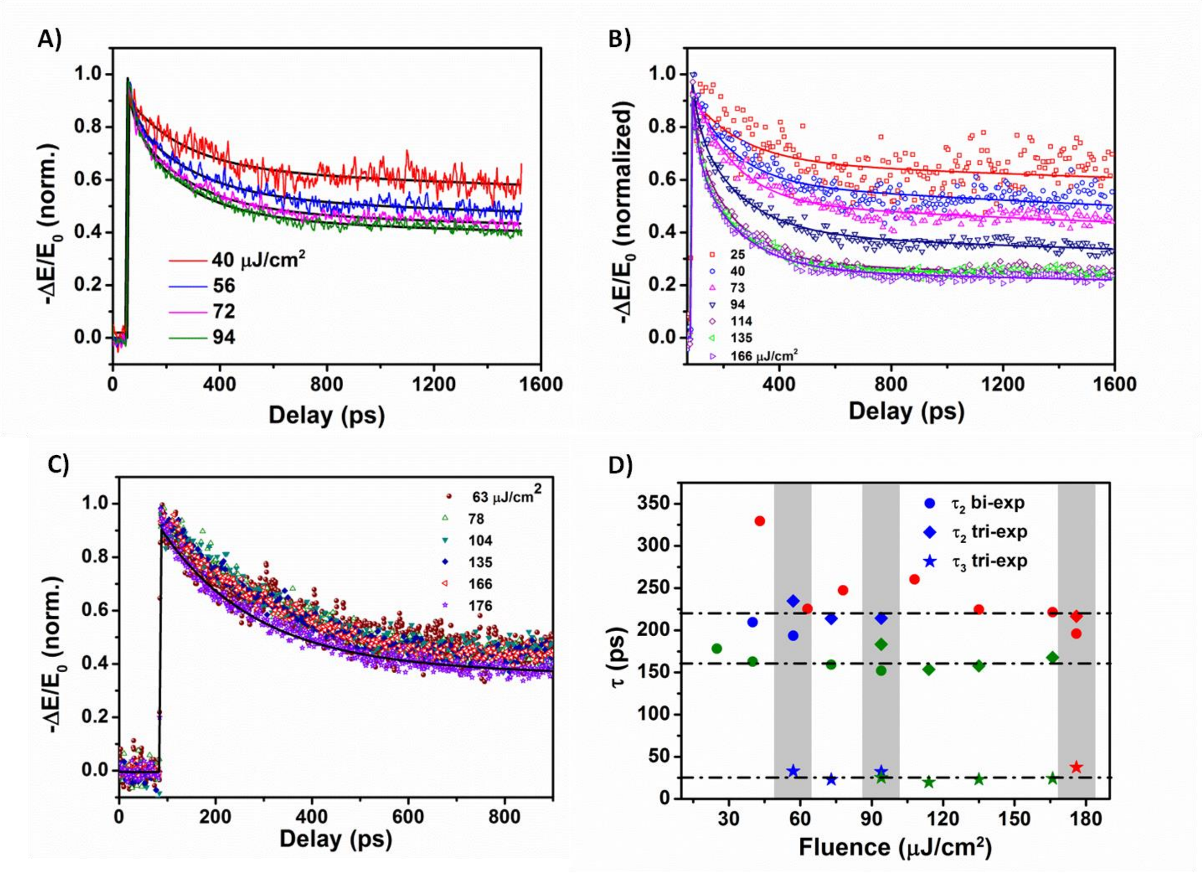

Figure 3.9. Normalized transient photoconductivity at different fluences for (A) 400 nm, (B) 480 nm and (C) 504 nm excitation. Points are experimental data and the solid lines are bi-exponential and tri-exponential fits to the data points. THz transients were recorded at varied fluences (25 μJ/cm^2 to 166 μJ/cm^2) and till ~1.6 ns for 480 nm pump; however, we could record THz transients only up to 94 μJ/cm^2 fluence for 400 nm pump. We limited pump-probe scan till 800 ps for 504 nm pump to reduce experiment time, which should be long enough as it is already evident from Figure 3.9.A and 3.9.B that the THz transients flatten off by 800 ps and does not change further within the temporal window of our experiment. (D) Time constants of different exponential obtained from the fits at 400 nm (blue), 480 nm (olive) and 504 nm (red) pump wavelengths. The shaded areas indicate average fluences at which a bi-exponential to tri-exponential change takes place.

We attribute this slow decay to trap-assisted recombination which is monomolecular ($dn/dt = -k_1\, n$) in nature and exhibits no fluence dependence. Geminate electron-hole (single exciton) recombination is also a first order process but will not be reflected in our data as discussed above. PL decay dynamics (with very small excitation fluence) of the same CsPbBr$_3$ NC sample reported in ref. 18 suggested contribution from radiative decay channels with lifetimes 3 and 8 ns, without the presence of any sub-ns nonradiative decay channels. Our attempts to fit the THz transients with lifetimes (τ_1) of the slowest decay components in the range of 1.5 to 8 ns were unsuccessful; instead, a reasonable fit was obtained with $\tau_1 \geq 15$ ns. For simplicity, we kept τ_1 fixed at 15 ns (10 times of our temporal window) for fitting all THz transients in Figure 3.9. Though our transient data (limited to 1.5 ns) cannot estimate τ_1 with certainty, however, it clearly suggests that the contribution from monomolecular trap-assisted decay is inefficient, and slower than the radiative PL decay. This observation agrees with nearly ideal (80%) PL quantum yield, and the observed high carrier mobilities in $CsPbBr_3$ NCs.

For 400 nm pump, THz transient at lowest fluence (~40 μJ/cm^2) fits quite well with a bi-exponential but those at higher fluence fit better to a tri-exponential. Similarly, for 480 nm pump, THz transients up to fluence value of ~90 μJ/cm^2 fit to a bi-exponential function but need a tri-exponential at higher fluences. In contrast, at 504 nm pump wavelength, the carrier decay dynamics can be well represented with a bi-exponential for all fluences except one (176 μJ/cm^2) where a tri-exponential gives a better fit to the data. The time constants obtained from the bi and tri-exponential fits for all pump wavelengths and fluences are shown in Figure 3.9.D. The second exponential has an average time constant (τ_2) of ~160 ps for 480 nm pump and ~220 ps for 400 and 504 nm pumps. We attribute this pathway of carrier relaxation to the bi-molecular electron-hole recombination ($dn/dt = -k_2 n^2$), which takes place at all pump fluences. The third and the fastest carrier relaxation channel which is evident only above a threshold fluence at a particular pump wavelength, has an average time constant (τ_3) ~25 ps, and is attributed to the tri-molecular non-radiative Auger recombination ($dn/dt = -k_3\, n^3$). By increasing the τ_1 value above 15 ns, we did not see any appreciable change in the two time constants, τ_2 and τ_3.

The threshold fluence (shaded part in Figure 3.9.D) for the Auger process corresponds to ~1.4 excitons per NC for 400 and 480 nm pumps, and ~2.7 excitons per NC for 504 nm pump. This observation can be rationalized by comparing the available average kinetic energy of the carriers. In case of 400 and 480 nm pumps, the excess carrier kinetic energies (~640 meV and ~120 meV respectively) make a three body collision between the charge carriers (essential for Auger process) take place at a modest carrier density (~1.4 excitons per NC), whereas almost a double carrier density is required to make such a collision probable when the carriers are generated with no or minimum excess kinetic energy.

Table 3.3: Details of parameters obtained from fitting the frequency averaged transient photoconductivity data to multi-exponential decay function (Eqn. 5) at excitation pulse energy. Error bars are calculated from the standard deviations of coefficients and time constant values of the fits of the experimental transients to the exponential function.

λ_{pump} (nm)	**Fluence (μJ/cm^2)**	**$N_{ph}/10^{15}$ (cm^3)**	τ_1	a_1	τ_2	a_2	τ_3	a_3
400	41	1.50	15000	0.62 (0.001)	209.7 (0.9)	0.27 (0.001)	..	..
	57	2.07	15000	0.53 (0.00)	234.8 (0.9)	0.32 (0.001)	32.9 (0.7)	0.13 (0.001)
	72	2.62	15000	0.49 (0.00)	214.0 (0.5)	0.36 (0.001)	22.9 (0.3)	0.14 (0.001)
	94	3.42	15000	0.46 (0.00)	214.4 (0.5)	0.37 (0.001)	32.2 (0.3)	0.18 (0.001)
480	24.9	0.55	15000	0.60 (0.001)	178.2 (1)	0.25 (0.001)	..	..
	39.5	0.87	15000	0.56 (0.001)	162.8 (0.4)	0.37 (0.001)	..	..
	72.7	1.61	15000	0.49 (0.00)	159.2 (0.2)	0.46 (0.001)	..	..
	93.5	2.07	15000	0.38 (0.00)	183.4 (0.3)	0.44 (0.001)	25.3 (0.2)	0.20 (0.001)
	114.3	2.53	15000	0.28 (0.00)	153.6 (0.02)	0.50 (0.001)	19.8 (0.2)	0.21 (0.001)
	135.1	2.98	15000	0.26 (0.00)	157.7 (0.2)	0.44 (0.001)	23.2 (0.1)	0.26 (0.001)
	166.3	3.67	15000	0.25	167.7	0.44	24.1	0.29

				(0.00)	(0.2)	(0.001)	(0.1)	(0.001)
504	42.6	0.97	15000	0.46 (0.002)	329.5 (8.5)	0.14 (0.001)	..	..
	63.4	1.44	15000	0.48 (0.001)	225.4 (1.1)	0.42 (0.001)	..	..
	78	1.77	15000	0.43 (0.00)	214.6 (0.6)	0.46 (0.001)	..	..
	104	2.36	15000	0.43 (0.001)	247.3 (0.5)	0.5 (0.00)	..	..
	135	3.06	15000	0.44 (0.00)	260.3 (0.6)	0.53 (0.00)	..	..
	166	3.76	15000	0.43 (0.00)	224.5 (0.3)	0.55 (0.00)	..	..
	176	3.99	15000	0.38 (0.00)	221.5 (0.3)	0.53 (0.00)	37.4 (1.1)	0.07 (0.001)

Alternatively, following the method of Herz and co-workers,[25-27] we have fitted the frequency averaged THz transients, as shown in figure 3.10, to the overall kinetic equation, which includes all three possible mechanisms of carrier recombination discussed above,

$$\frac{dn}{dt} = -k_1.n - k_2.n^2 - k_3.n^3. \qquad (3.6)$$

The global fit of all THz transients at different fluences allows us to determine the rate constants (k_1, φk_2, $\varphi^2 k_3$) for different carrier recombination processes, and are given in Table 3.4.

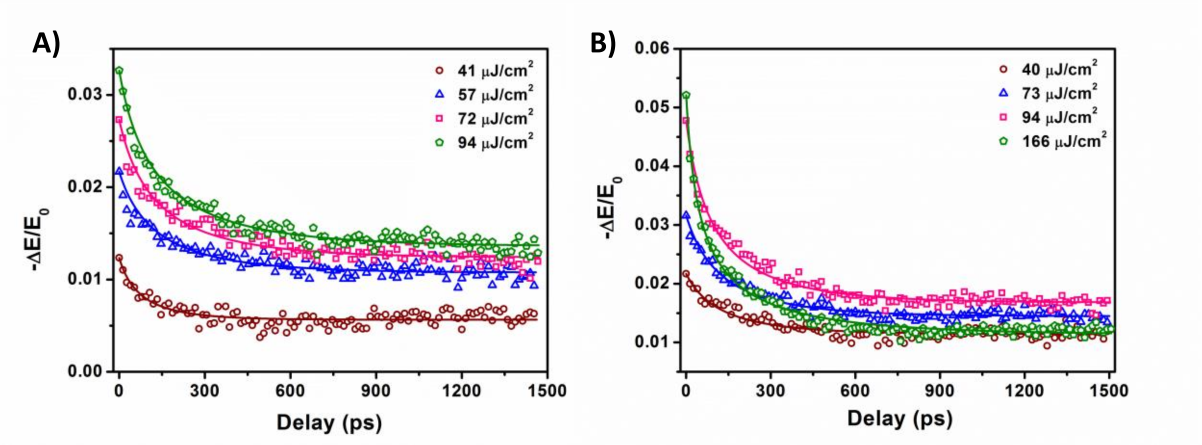

Figure 3.10: Carrier density vs pump-probe delay at different fluences for (A) 400 nm and (B) 480 nm pump. The solid lines are the fits to the kinetic equation: $\frac{dn}{dt} = -k_1.n - k_2.n^2 - k_3.n^3$; where k_1, k_2, and k_3 are the rate constants for mono-molecular trap-assisted recombination, bi-molecular electron-hole recombination, and tri-molecular Auger recombination, respectively.

Table 3.4: Kinetic parameters obtained from fitting the frequency averaged and frequency-resolved data to the kinetic equation. The frequency averaged data evaluates k_1, φk_2, and $\varphi^2 k_3$, whereas frequency resolved data evaluates k_1, k_2 and k_3 directly.

λ_{pump} (nm)		k_1 (s^{-1})	k_2 or φk_2 ($cm^3\ s^{-1}$)	k_3 or $\varphi^2 k_3$ ($cm^6\ s^{-1}$)
400	Frequency Resolved	$1.7 \pm 0.14 \times 10^{9}$	$1.35 \pm 0.8 \times 10^{-7}$	$9.55 \pm 2.2 \times 10^{-22}$
	Frequency Averaged	$2.37 \pm 0.8 \times 10^{9}$	$2.99 \pm 0.24 \times 10^{-7}$	$3.14 \pm 0.18 \times 10^{-23}$
480	Frequency Resolved	$0.9 \pm 0.7 \times 10^{9}$	$9.3 \pm 0.14 \times 10^{-8}$	$1.016 \pm 0.06 \times 10^{-21}$
	Frequency Averaged	$2.93 \pm 0.39 \times 10^{9}$	$9.14 \pm 2.14 \times 10^{-7}$	$4.53 \pm 0.45 \times 10^{-23}$

3.5.4 Diffusion Length:

Diffusion length (L_D) of carriers is an important parameter for a semiconductor material to be used in photovoltaic and other electro-optic devices. We present here an estimation of carrier diffusion length for the CsPbBr$_3$ NCs from an average lifetime according to the relation: $L_D = \sqrt{(\langle\tau\rangle\mu k_B T/q)}$; where $\langle\tau\rangle$ is the average life time, μ is the mobility, k_B is Boltzmann constant, T is temperature and q is the elementary charge. Average lifetime $\langle\tau\rangle$ is calculated as $\langle\tau\rangle = \sum f_i\tau_i$, where f_i is the steady state population fraction of the i^{th} decay channel.[67], [68] Taking τ_1 to be 15 ns (used in the multi-exponential fitting of all our THz transient data in Figure 3.9) gives an average L_D of 9.2±1 μm. As discussed above, 15 ns is the lower limit of τ_1 restricted by the temporal window of our experiments. τ_1 as high as 2.5 μs was reported for single crystalline bulk CsPbBr$_3$.[65] Assuming the τ_1 to be 2.5 μs for the NCs as well, the average diffusion length would increase to 120±10 μm. So, we estimate the lower limit of the carrier diffusion length of CsPbBr$_3$ NCs at room temperature to be ~9.2 μm, which is of similar order as in CH$_3$NH$_3$PbBr$_3$ single crystal and several conventional semiconductors.[5,10] Such long diffusion length indicates a very low density of mid-gap trap states in these NCs. Figure 3.11 shows a variation of diffusion length, obtained from the average lifetime and initial mobility, as a function of carrier density.

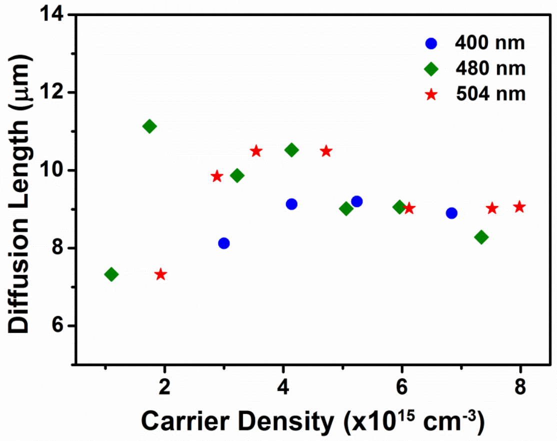

Figure 3.11: Diffusion length obtained from the average lifetime and initial mobility as a function of initial carrier density.

3.5.5 Frequency-resolved dynamics:

We have conducted frequency-resolved transient photoconductivity experiments to evaluate the temporal evolution of carrier density and mobility from an alternative approach, which is not limited by the approximation of the frequency-averaged method. This approach provides actual carrier density (N) and mobility (μ), not their higher (N_0/φ) and lower ($\varphi\mu$) limits respectively.[29] Quantitative comparisons between the results from these two approaches can indeed evaluate the quantum efficiency (φ) of free carrier generation from the absorbed photons. Figure 3.12 (A , B and C, D) display the complex photoconductivity spectra in the range of 0.7 to 5.0 THz for 480 nm pump with 73 and 166 μJ/cm^2 fluences and Figure 3.13 (A, B and C, D) show the complex photoconductivity spectra in the same range for 400 nm pump at 57 and 94 μJ/cm^2 fluences. At all fluences, irrespective of pump wavelength, the real conductivity ($\Delta\sigma_1(\omega)$) is maximum immediately after photoexcitation and reduces with increasing pump-probe delay which implies the decrease in carrier density with time after photoexcitation. There is a strong absorption feature at ~3 THz in the real photoconductivity spectra and a corresponding crossover from negative to positive in the imaginary photoconductivity spectra. This absorption feature, which corresponds to the phonon vibration (also observed in the non-photoexcited sample, see Figure 3.6.C and 3.6.D), has maximum intensity immediately after photoexcitation and decays with increasing pump-probe delay. This probably indicates to an instantaneous thermalization of the photo-generated carriers through possible exciton-phonon and/or free-carrier-phonon coupling. It is interesting to note that the phonon peak has moved to a lower frequency on photoexcitation. This may be due to relatively stronger carrier-phonon coupling with the softer modes.

As the real photoconductivity ($\Delta\sigma_1(\omega)$) is increasing with frequency and the corresponding imaginary component ($\Delta\sigma_2(\omega)$) is negative at lower frequencies, we have fitted our complex conductivity data to truncated Drude-Smith (DS) model of conductivity[43,69] to extract the carrier density and mobility. Very small contribution from exciton polarizability, especially at the early pump-probe delay, may also be present in the observed photoconductivity; but has been ignored in the present analysis. According to the DS model, the complex conductivity is given by:

$$\Delta\tilde{\sigma}(\omega) = \frac{\varepsilon_0 \omega_p^2}{\Gamma - i\omega}\left(1 + \frac{C\Gamma}{\Gamma - i\omega}\right) \qquad (3.7)$$

where ω_p is the plasma frequency, Γ is carrier scattering rate and C is the expectation value of $\langle\cos\theta\rangle$ for carrier scattering angle θ. The C parameter, which represents the degree of carrier localization, may have values between 0 (Drude behaviour, delocalized carrier) and -1 (fully localized carrier). The C parameters in our fits are ~-1 suggesting near complete localization of the carriers within the NC. This is quite rational considering the fact that the nanometer sized crystallites are embedded in non-conducting medium (solvent). We have calculated the carrier density from plasma frequency as $N = \varepsilon_0\omega_p^2 m^*/e^2$, and mobility from the scattering rate as $\mu = e/\Gamma m^*$, where e is the electronic charge and m^* is the carrier effective mass. As the carrier effective masses in $CsPbBr_3$ NCs have not yet been measured experimentally, we have used the effective masses obtained from our DFT calculations at the GGA+vdW level of theory (Table 3.1) in the above equations. Since both electron and hole will contribute to the observed photoconductivity, and we have no prior information about their individual contributions, we have used an average carrier effective mass ($m^* = ½ (m_e + m_h)$ for evaluating carrier density and mobility. As the carrier effective masses in $CsPbBr_3$ NCs have not yet been measured experimentally, we have used the effective masses obtained from our DFT calculations at the GGA+vdW level of theory (Table 3.1) in the above equations. It is important to note that the effective masses, reported here using GGA functional, may differ from the actual values, and therefore may under or overestimate the carrier density and mobility values. For example, He *et al.*[70] and Menéndez-Proupin *et al.*[71] have found that for $CH_3NH_3AI_3$ (A=Pb and Sn) typical errors in the values of the effective masses computed from GGA are ~10% in comparison to more accurate GW calculation. Assuming similar errors in our calculations of the effective masses, we estimate the errors in our mobility and carrier density also to be ~10% (linear dependence). However, it is very encouraging to find that the effective masses ($m_e = 0.22$ & $m_h = 0.24$) of $CsPbBr_3$ calculated at the GGA+vdW level of theory are very similar to the experimentally observed values for analogous $MAPbBr_3$ in its low temperature orthorhombic phase.[72] Krzysztof Galkowski *et al.* very recently reported the exciton reduced mass ($\mu = m_e . m_h / (m_e + m_h)$) to be 0.117, which yields an average carrier effective mass ($m^* = 2\mu$) to be 0.234 assuming similar masses for electron and hole ($m* = m_e = m_h$).[72]

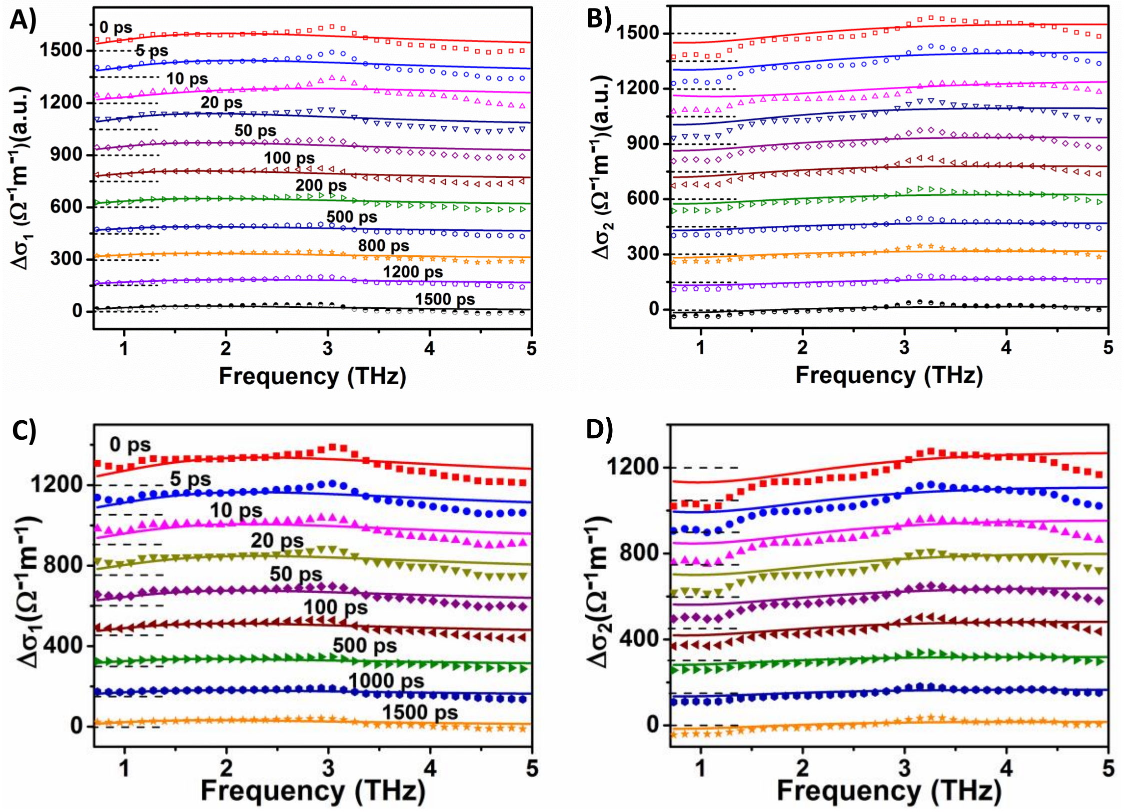

Figure 3.12. Frequency-resolved real (A and C) and imaginary (B and D) conductivity spectra at a fluence of 73 (upper panels) and 166 μJ/cm² (lower panels) for 480 nm pump wavelength. Solid lines are fit to the Drude-Smith model. The spectra at all delays except at longest delays are vertically offset for clarity.

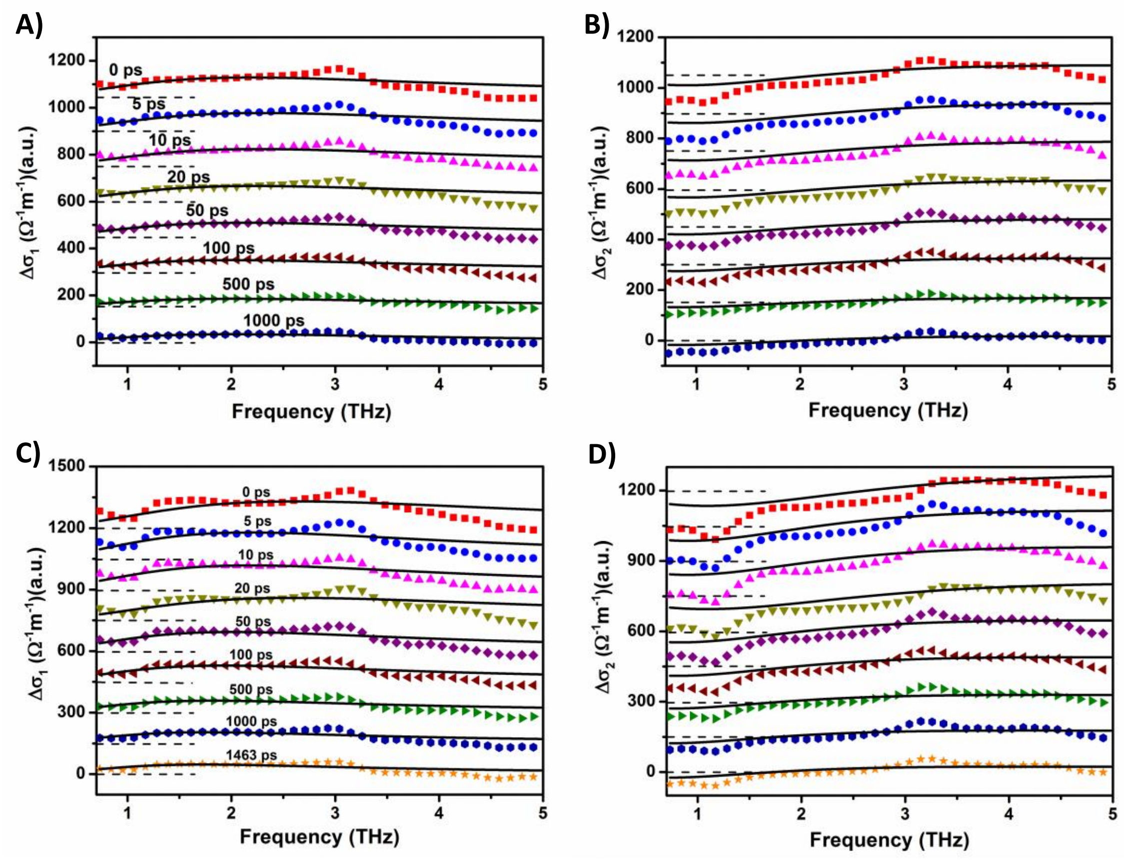

Figure 3.13. Frequency-resolved real (A and C) and imaginary (B and D) conductivity spectra at a fluence of 57 (upper panels) and 94 μJ/cm^2 (lower panels) for 400 nm pump wavelength. Solid lines are fit to the Drude-Smith model. The spectra at all delays except at longest delays are vertically offset for clarity.

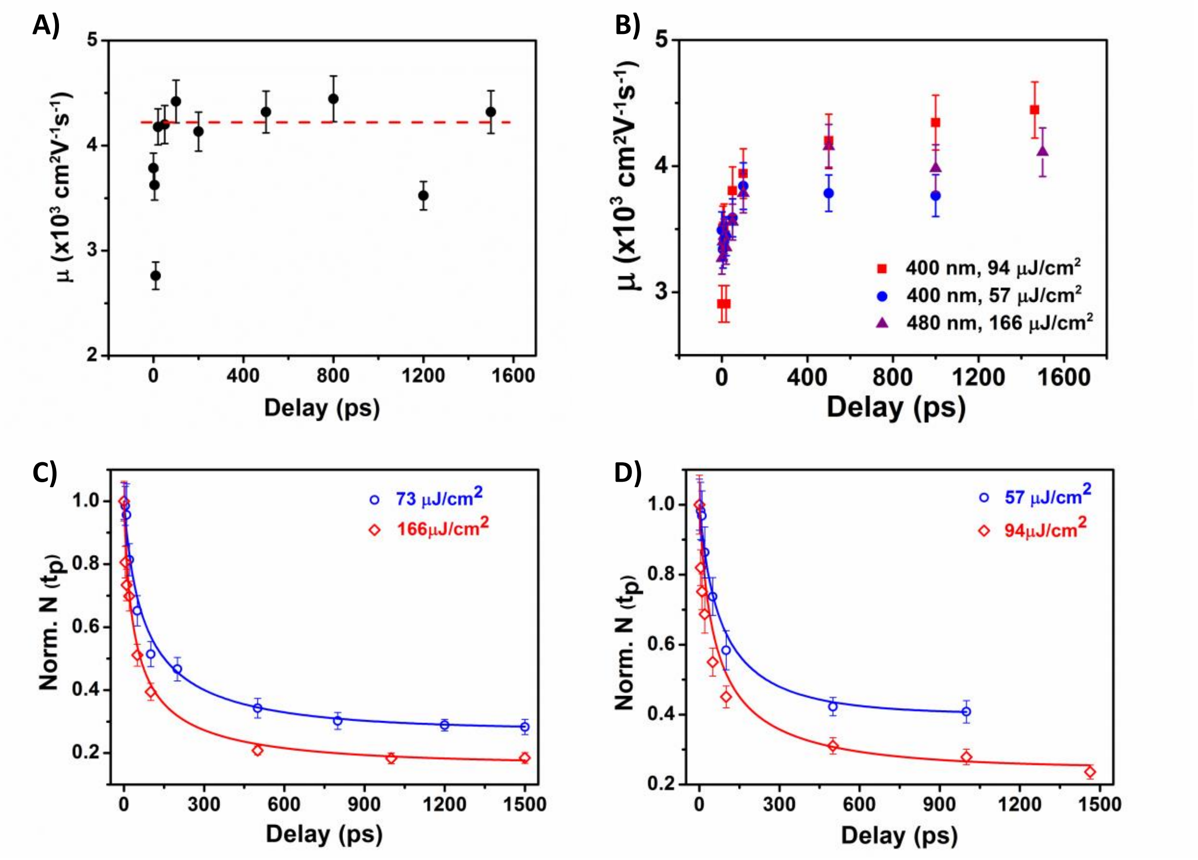

Figure 3.14. Mobilities and carrier density obtained from fitting the Drude-Smith model to frequency-resolved conductivity at 480 and 400 nm pumps. Change in mobilities, A) with 480 nm pump at 73 μJ/cm^2 and B) with 480 and 400 nm pumps at 166 μJ/cm^2 and 54, 97 μJ/cm^2, with pump-probe delay. Red dashed line indicates the average mobility after 20 ps. Carrier density vs. pump-probe delay (C and D) at 480 and 400 nm pump wavelengths. Points are experimental data whereas the lines are fits to the kinetic equation: $\frac{dn}{dt} = -k_1.n - k_2.n^2 - k_3.n^3$. The error bars in Figures 3.14 (A, B, C &D) are the uncertainties in calculated values of mobility and carrier density obtained from the corresponding uncertainties of the DS parameters.

The calculated mobilities at 480 nm pump wavelength with 73 μJ/cm^2 fluence are shown in Figure 3.14.A. The mobility values initially increase with pump-probe delay (t_p) and reach a steady value by ~20 ps. A similar increase in mobility at early pump-probe delay has been observed earlier in case of $CH_3NH_3PbI_3$ perovskite films[29] and was attributed to initial thermalization of hot carriers.[29] The higher scattering rate (lower mobility) at the initial stage after photoexcitation may take place due to a higher population of the optical phonons as evident in Figure 3.12 (A and C) and in Figure 3.13 (A and C). The average mobility value at pump-probe delay > 20 ps is ~4250±300 cm^{2}V$^-$

$^{1}s^{-1}$. The steady-state mobility values are higher than the initial mobility values estimated from frequency averaged peak conductivity approximately by a factor of 1.6. The ratio of the mobility (μ) at early pump-probe delays from the frequency-resolved data to the effective mobility (φμ) obtained from the peak conductivity of frequency averaged response essentially yields the photon to free carrier generation quantum efficiency φ to be ~0.65±0.06 (see table 3.5). If our initial assumption of an absorbed photon to electron-hole pair conversion ratio of unity is valid, then, ~35% of the electron-hole pairs remain as bound excitons or undergo direct recombination from excitonic states during the course of THz pump-probe experiment. This indicates to an exciton binding energy for these NCs in the order of thermal energy at room temperature.

The carrier densities immediately after photoexcitation at different pump conditions are given in table 3.5 for comparison with the density of absorbed photons. The carrier densities obtained from plasma frequencies are the actual free carrier densities and does not depend on any approximation. We have calculated the photon to free carrier conversion ratio ($\varphi = N_0(\omega_p)/2Np$), and given in the 5th column in Table-3.5. Alternatively, we have calculated φ also from mobility values obtained from frequency averaged and frequency-resolved approaches and is tabulated in the 8th column of table-3.5. The calculated φ values from two different approaches are quite similar.

Table 3.5. Comparison between frequency averaged and frequency-resolved results. The volume fraction of the NC solution is ~2x10^{-3}.

λ_{pump} (nm)	Fluence ($\mu J/cm^2$)	$N_0/10^{15}$ (cm^{-3})		φ	Initial mobility ($cm^2V^{-1}s^{-1}$)		φ	L_D (μm)
		$2N_{ph}$	N_0 (DS)^a	$N_0/2N_{ph}$	φμ	μ (DS)^a	φμ / μ	τ_1=15 ns
400	57	4.1	2.8	0.68	2208	3491	0.63	9.1
400	94	6.8	5.6	0.82	2100	2907	0.72	8.9
480	73	3.2	3.2	1.00	2580	3785	0.68	9.9
480	166	7.3	5.3	0.73	1839	3267	0.56	8.3

^{a}DS = Drude-Smith

The carrier densities calculated from the plasma frequencies (ω_p) obtained from DS fits for photoexcitation with 480 and 400 nm pumps of fluences 73 and 166 μJ/cm^2 and 57 and 94 μJ/cm^2 are shown in Figure 3.14 (C and D). The decay of the carrier density with the pump-probe delay has been fitted to the kinetic model (equation 6) that includes all possible decay channels (solid lines in Figures 3.14. C and D).[25-27] Rate constants (k_1, k_2, k_3) obtained from the fits are given in Table 4. To the best of our knowledge, this is the first ever study where the kinetic parameters were determined from both frequency-averaged and frequency-resolved THz transients of the same sample under the same condition. The kinetic parameters obtained from the two approaches are of a similar order and confirms the presence of three-fold carrier recombination mechanism. However, a quantitative comparison between them may not be appropriate because of the following reasons. Firstly, the temporal window of our experiment is not adequate enough to determine k_1, which introduces errors in other parameters as well. Secondly, the number of data points in the frequency-resolved study is few and needs to be increased for a more accurate analysis. Lastly, any inadequacy of the conductivity model (Drude-Smith model in this case) used to extract the carrier density is also likely to add to the errors in determining the kinetic parameters. Hence, the rate constants reported in Table 4 should be considered as approximate estimation rather that accurate numbers.

Table 3.6. Comparison of mobility and diffusion length of $CsPbBr_3$ NCs with those of other important NCs and single crystals. Note that a direct comparison of the mobility and diffusion length values is totally viable among materials for which the parameters are determined using the same technique under the same condition (such as THz spectroscopy). A comparison of parameter values across different measurement techniques should be done with great care.

Material	Mobility ($cm^2V^{-1}s^{-1}$)		Diffusion Length (μm)		Measurement technique
	Electron	Hole	Electron	Hole	
$CsPbBr_3$ NC (this work)	~4500	~4500	≥ 9.2	≥ 9.2	THz

$CsPbBr_3$ single crystal[65]	~1000				PC
$MAPbBr_3$ polycrystalline film[5]	30		0.3 – 1		THz
$MAPbBr_3$ single crystal[10]	~115	20-60	3 - 17		TOF/Hall/TA/TRPL
$MAPbI_3$ single crystal[73]	500-800	500-800			THz
CdSe NCs[42]	~1-100				THz
CdSe bulk[42]	~470	~145			THz
GaAs crystal[74]	~8000	~400	7	1.6	Hall
Si crystal[74]	~1450	~500	1000	600	Hall
PbTe crystal[74]	~6000	~4000			Hall

MA = CH_3NH_3, THz = terahertz spectroscopy, PC = photoconductivity, TOF = time of flight, TA = transient absorption, TRPL = time resolved photoluminescence

3.5.6 Surface does not Trap Carriers!

Our THz conductivity data show that mid-gap trap states are negligible in $CsPbBr_3$ NCs, which in turn can manifest into PL quantum yield of ~ 80%, the carrier mobility of ~4500 $cm^2V^{-1}s^{-1}$, and diffusion length of >9.2 μm. One should note that the diffusion length mentioned above is its lower limit because of underestimation of τ_1. To the best of our knowledge, such an extraordinary combination of semiconductor properties has not been observed in any colloidal NCs studied so far. Table 3.6 compares the carrier mobility values of the various known semiconductor in the form of bulk single crystals, thin films, and colloidal NCs. Among these materials, only PbTe crystal has an electron and hole mobilities similar to $CsPbBr_3$ NCs. GaAs crystal has higher electron mobility but much lower hole mobility due to the heavier hole. We find that in these NCs the carrier mobility is 1-3 orders of magnitude higher than that in CdSe NCs depending on their sizes. Additionally, the lower limit of the carrier diffusion length in these NCs are comparable to those found in the more expensive GaAs and $MAPbBr_3$ single crystals, and are much higher, as expected, than that in polycrystalline $MAPbBr_3$ because the conductivity is affected by carrier scattering at the inter-particle interfaces and grain boundaries. Thus our colloidal $CsPbBr_3$ NCs behave like the best quality bulk single crystals even though these NCs possess high surface to volume ratio, and synthesized in solution-based process. In the case of native $CsPbBr_3$ NCs it is difficult to probe carrier dynamics for electrons and holes, separately. The effective masses of charge carriers in case of $CsPbBr_3$ NCs are almost similar (m_e=0.22, m_h=0.24). Hence, the intra-band relaxations for electrons and holes are similar because of similar energy spacing between the intra-band energy levels. However, the effective masses for electrons and holes for various semiconductors given in Table 3.6 are very different. For GaAs the electron and hole masses are 0.067 and 0.45 m_e, respectively. Hence, the mobilities are quite different for electrons and holes.

Interestingly, the NCs exhibit two orders magnitude larger carrier mobility compared to polycrystalline films of $MAPbBr_3$ and about one order of magnitude higher than in $MAPbBr_3$ single crystal suggesting lower intrinsic crystal-defects in these NCs. This decrease in intrinsic-crystal defects may arise from several factors, namely (i) smaller NCs are known for their efficient ejection of defects from the core of NC,[75] (ii) a better control in the colloidal synthesis of these NCs employing relatively high (190 ^oC) reaction temperature and surface passivation with capping layers, and (iii) replacement of $CH_3NH_3^+$ with Cs^+ provides better crystallinity. A direct comparison with $MAPbBr_3$ NCs would be more enlightening in determining the effect of Cs^+; however, we have not come across such data in the current literature. It is important to note that the electron mobility in $CsPbBr_3$ single crystal was reported to be of same order of magnitude as that of the NCs.[65] Recently, mobility values up to 800 $cm^2V^{-1}s^{-1}$ have been reported for $MAPbI_3$ single crystal, and this was attributed to a better crystal quality with lower defect density.[73] Therefore, high carrier mobility may be intrinsic to these class materials. However, the density of defects may vary depending on the method of synthesis modulating the mobility. In addition, free rotation and large amplitude vibrations of the $CH_3NH_3^+$ moiety may increase the phonon scattering, reducing the mobility further.

It is well known that NCs with large surface to volume ratio possesses a large density of dangling bonds on the surface. Trapping of charge carriers by these surface dangling bonds is one of the major hindrances to electronic, optical and optoelectronic applications of semiconductor NCs. However, observation of exceptionally high mobility (within the NC) suggests negligible mid-gap trap states in case of colloidal $CsPbBr_3$ NCs.

Our electronic structure calculation of bulk $CsPbBr_3$ shows that valence band maximum arises from anti-bonding Pb 6*s* and Br 4*p* states, and conduction band minimum is predominately a Pb 6*p* state. On the other hand, relativistic spin-orbit interaction has been reported to increase the bandwidth of Pb 6*p* conduction band by ~ 2 eV lowering the energy of conduction band minimum compared atomic Pb 6*p* states.[76] According to this unique band structure, a dangling (non-bonding atomic like orbital, or lower coordination number) Pb 6*s* and Br 4*p* bond on the surface is expected to have energy lower than (or similar to) the valence band maximum, and a dangling Pb 6*p* is expected to exhibit energy higher than (or similar to) the conduction band minimum. In other words, there is no deep trap state in the mid-gap region of $CsPbBr_3$ NCs to influence the mobilities and diffusion lengths of charge carriers, unlike in the case of CdSe NCs.

Though we find extremely high carrier mobility values for $CsPbBr_3$ NCs from our OPTP study, it needs to be independently validated by other more direct measurements. Further to the uncertainties shown in Figure 3.14.A and B, there may be additional errors in our measurements arising from uncertainties related to the evaluation of volume fraction, choice of effective medium theory, and any inadequacy of DS model in describing the observed conductivities. It is also important to realize that the mobility and diffusion lengths reported in the present work are within the tiny NCs probed locally using an AC field. Magnitudes of these semiconductor properties are expected to differ, rather significantly, in NC solids (film) measured using techniques such as field effect transistor or hall measurement, which involve charge transport both within a NC and through the interface between adjacent NCs. One should also not expect similar numbers in a device architecture employing these NCs, due to losses at the inter-particle interfaces and non-ideality of any electrical connections. Since colloidal $CsPbBr_3$ NCs are capped with insulating organic capping ligands, a poor charge transport across adjacent NCs is expected. However, further development of surface chemistry will certainly improve the potential of these NCs for optoelectronic applications.

3.6 Stability of Colloidal $CsPbX_3$ NCs:

$CsPbX_3$ perovskites are relatively stable compared with hybrid organic-inorganic perovskites (HOIP). These HOIPs degrade to volatile gases and forms hydrates at environmental humid and temperature conditions. Efforts are underway to increase the stability of the NCs. One way to increase the stability is by surface modification. Very initial report suggests that the native NCs are stable upto 150 min.[18] Later, Koscher et al. showed photo stability up to 90 hr, after post-synthetic treatment of $CsPbBr_3$ NCs with thiocyanate (SCN^-) salts, with near unity quantum yield.[77] Very recently, the photo stability was checked after silver complex treatment. These NCs showed excellent photo stability even after 5 days with 80 % quantum yield.[78]

3.7 Conclusions:

In conclusion, time-resolved THz spectroscopy, in conjunction with first principles DFT calculations, has been employed to elucidate free carrier dynamics, carrier mobility, diffusion length, and phonon modes of colloidal $CsPbBr_3$ NCs in the range of 0.5 to 7.0 THz. The phonon absorption band has a peak at ~3.4 THz. DFT calculations (at GGA+vdW level) suggest that the vibrations of the $PbBr_6$ octahedron contribute to the THz absorption. The major contributions come from an antisymmetric apical Pb-Br stretching mode and one in-plane Br-Pb-Br bending mode. Time-resolved THz spectroscopic study of the photoexcited free carrier dynamics within the NCs shows three channel mechanism of carrier relaxation: trimolecular non-radiative Auger recombination, bimolecular electron-hole recombination, and monomolecular trap-assisted recombination with a time constants of ~25 ps, 150-300 ps and >15 ns respectively. Early free carrier dynamics indicates that exciton-free carrier equilibrium is established within 5-6 ps after photoexcitation. A strong exciton-phonon coupling gives rise to a strong phonon absorption feature on photoexcitation. Comparison of frequency averaged and frequency-resolved results evaluates photon to free carrier conversion ratio to be 0.65±0.06 and indicates to exciton binding energy in the order of thermal energy at room temperature. We find the charge carriers of the NCs to be highly mobile (~4500 $cm^2V^{-1}s^{-1}$) with long diffusion lengths (> 9.2 μm). These values are orders of magnitude higher compared to those found in the hybrid halide perovskite films and comparable to single crystalline bulk semiconductors. These values will certainly reduce in a device configuration but are anticipated to remain much higher compared to other semiconductor NCs. Therefore, $CsPbBr_3$ NCs are promising candidates for applications in optoelectronic and photovoltaic devices.

3.8 References:

(1) Stranks, S. D.; Snaith, H. J. *Nat. Nanotechnol.* **2015**, *10*, 391.
(2) Johnston, M. B.; Herz, L. M. *Acc. Chem. Res.* **2015**.
(3) Stranks, S. D.; Eperon, G. E.; Grancini, G.; Menelaou, C.; Alcocer, M. J. P.; Leijtens, T.; Herz, L. M.; Petrozza, A.; Snaith, H. J. *Science* **2013**, *342*, 341.
(4) Lee, M. M.; Teuscher, J.; Miyasaka, T.; Murakami, T. N.; Snaith, H. J. *Science* **2012**, *338*, 643.
(5) Brenner, T. M.; Egger, D. A.; Kronik, L.; Hodes, G.; Cahen, D. *Nat. Rev.Mater.* **2016**, *1*, 15007.
(6) Yang, W. S.; Noh, J. H.; Jeon, N. J.; Kim, Y. C.; Ryu, S.; Seo, J.; Seok, S. I. *Science* **2015**, *348*, 1234.
(7) Kojima, A.; Teshima, K.; Shirai, Y.; Miyasaka, T. *J. Am. Chem. Soc.* **2009**, *131*, 6050.
(8) Etgar, L.; Gao, P.; Xue, Z.; Peng, Q.; Chandiran, A. K.; Liu, B.; Nazeeruddin, M. K.; Grätzel, M. *J. Am. Chem. Soc.* **2012**, *134*, 17396.
(9) Stoumpos, C. C.; Kanatzidis, M. G. *Acc. Chem. Res.* **2015**, *48*, 2791.
(10) Shi, D.; Adinolfi, V.; Comin, R.; Yuan, M.; Alarousu, E.; Buin, A.; Chen, Y.; Hoogland, S.; Rothenberger, A.; Katsiev, K.; Losovyj, Y.; Zhang, X.; Dowben, P. A.; Mohammed, O. F.; Sargent, E. H.; Bakr, O. M. *Science* **2015**, *347*, 519.
(11) NREL Efficiency Chart. http://www.nrel.gov/ncpv/images/efficiency_chart.jpg (accessed June 8.
(12) Tan, Z.-K.; Moghaddam, R. S.; Lai, M. L.; Docampo, P.; Higler, R.; Deschler, F.; Price, M.; Sadhanala, A.; Pazos, L. M.; Credgington, D.; Hanusch, F.; Bein, T.; Snaith, H. J.; Friend, R. H. *Nat. Nanotechnol.* **2014**, *9*, 687.
(13) Yakunin, S.; Sytnyk, M.; Kriegner, D.; Shrestha, S.; Richter, M.; Matt, G. J.; Azimi, H.; Brabec, C. J.; Stangl, J.; Kovalenko, M. V.; Heiss, W. *Nat. Photonics* **2015**, *9*, 444.
(14) Protesescu, L.; Yakunin, S.; Bodnarchuk, M. I.; Krieg, F.; Caputo, R.; Hendon, C. H.; Yang, R. X.; Walsh, A.; Kovalenko, M. V. *Nano Lett.* **2015**, *15*, 3692.
(15) Yakunin, S.; Protesescu, L.; Krieg, F.; Bodnarchuk, M. I.; Nedelcu, G.; Humer, M.; De Luca, G.; Fiebig, M.; Heiss, W.; Kovalenko, M. V. *Nat. Commun.* **2015**, *6*.
(16) Wang, Y.; Li, X.; Song, J.; Xiao, L.; Zeng, H.; Sun, H. *Adv.Mater.* **2015**, *27*, 7101.
(17) Bekenstein, Y.; Koscher, B. A.; Eaton, S. W.; Yang, P.; Alivisatos, A. P. *J. Am. Chem. Soc.* **2015**, *137*, 16008.
(18) Swarnkar, A.; Chulliyil, R.; Ravi, V. K.; Irfanullah, M.; Chowdhury, A.; Nag, A. *Angew. Chem. Int. Ed.* **2015**, *54*, 15424.
(19) Zhang, X.; Lin, H.; Huang, H.; Reckmeier, C.; Zhang, Y.; Choy, W. C. H.; Rogach, A. L. *Nano Lett.* **2016**, *16*, 1415.
(20) Manser, J. S.; Kamat, P. V. *Nat. Photonics* **2014**, *8*, 737.
(21) Miyata, A.; Mitioglu, A.; Plochocka, P.; Portugall, O.; Wang, J. T.-W.; Stranks, S. D.; Snaith, H. J.; Nicholas, R. J. *Nat. Phys.* **2015**, *11*, 582.
(22) Christians, J. A.; Manser, J. S.; Kamat, P. V. *J. Phys.Chem.Lett.* **2015**, *6*, 2086.
(23) Yang, Y.; Yang, M.; Li, Z.; Crisp, R.; Zhu, K.; Beard, M. C. *J. Phys.Chem.Lett.* **2015**, *6*, 4688.
(24) Piatkowski, P.; Cohen, B.; Ponseca, C. S.; Salado, M.; Kazim, S.; Ahmad, S.; Sundström, V.; Douhal, A. *J. Phys. Chem. Lett.* **2016**, *7*, 204.
(25) Wehrenfennig, C.; Eperon, G. E.; Johnston, M. B.; Snaith, H. J.; Herz, L. M. *Adv. Mater.* **2014**, *26*, 1584.

(26) Rehman, W.; Milot, R. L.; Eperon, G. E.; Wehrenfennig, C.; Boland, J. L.; Snaith, H. J.; Johnston, M. B.; Herz, L. M. *Adv. Mater.* **2015**, *27*, 7938.
(27) Milot, R. L.; Eperon, G. E.; Snaith, H. J.; Johnston, M. B.; Herz, L. M. *Adv. Funct. Mater.* **2015**, *25*, 6218.
(28) Ponseca, C. S.; Savenije, T. J.; Abdellah, M.; Zheng, K.; Yartsev, A.; Pascher, T.; Harlang, T.; Chabera, P.; Pullerits, T.; Stepanov, A.; Wolf, J.-P.; Sundström, V. *J. Am. Chem. Soc.* **2014**, *136*, 5189.
(29) La-o-vorakiat, C.; Salim, T.; Kadro, J.; Khuc, M.-T.; Haselsberger, R.; Cheng, L.; Xia, H.; Gurzadyan, G. G.; Su, H.; Lam, Y. M.; Marcus, R. A.; Michel-Beyerle, M.-E.; Chia, E. E. M. *Nat. Commun.* **2015**, *6*.
(30) Karakus, M.; Jensen, S. A.; D'Angelo, F.; Turchinovich, D.; Bonn, M.; Cánovas, E. *J. Phys. Chem. Lett.* **2015**, *6*, 4991.
(31) La-o-vorakiat, C.; Xia, H.; Kadro, J.; Salim, T.; Zhao, D.; Ahmed, T.; Lam, Y. M.; Zhu, J.-X.; Marcus, R. A.; Michel-Beyerle, M.-E.; Chia, E. E. M. *J. Phys. Chem. Lett.* **2016**, *7*, 1.
(32) Herz, L. M. *Annu.Rev. Phys.Chem.* **2016**, *67*, 65.
(33) Wang, Y.; Li, X.; Zhao, X.; Xiao, L.; Zeng, H.; Sun, H. *Nano Lett.* **2016**, *16*, 448.
(34) Wu, K.; Liang, G.; Shang, Q.; Ren, Y.; Kong, D.; Lian, T. *J. Am. Chem. Soc.* **2015**, *137*, 12792.
(35) Makarov, N. S.; Guo, S.; Isaienko, O.; Liu, W.; Robel, I.; Klimov, V. I. *Nano Lett.* **2016**.
(36) Seth, S.; Mondal, N.; Patra, S.; Samanta, A. *J. Phys. Chem. Lett.* **2016**, *7*, 266.
(37) Park, Y.-S.; Guo, S.; Makarov, N. S.; Klimov, V. I. *ACS Nano* **2015**, *9*, 10386.
(38) Rainò, G.; Nedelcu, G.; Protesescu, L.; Bodnarchuk, M. I.; Kovalenko, M. V.; Mahrt, R. F.; Stöferle, T. *ACS Nano* **2016**, *10*, 2485.
(39) Hu, F.; Zhang, H.; Sun, C.; Yin, C.; Lv, B.; Zhang, C.; Yu, W. W.; Wang, X.; Zhang, Y.; Xiao, M. *ACS Nano* **2015**, *9*, 12410.
(40) Ramasamy, P.; Lim, D.-H.; Kim, B.; Lee, S.-H.; Lee, M.-S.; Lee, J.-S. *Chem. Commun.* **2016**, *52*, 2067.
(41) Beard, M. C.; Turner, G. M.; Schmuttenmaer, C. A. *J. Phys. Chem. B* **2002**, *106*, 7146.
(42) Beard, M. C.; Turner, G. M.; Schmuttenmaer, C. A. *Nano Lett.* **2002**, *2*, 983.
(43) Ulbricht, R.; Hendry, E.; Shan, J.; Heinz, T. F.; Bonn, M. *Rev.Mod. Phys.* **2011**, *83*, 543.
(44) Baxter, J. B.; Guglietta, G. W. *Anal. Chem.* **2011**, *83*, 4342.
(45) Brenner, T. M.; Egger, D. A.; Rappe, A. M.; Kronik, L.; Hodes, G.; Cahen, D. *J. Phys. Chem. Lett.***2015**, *6*, 4754.
(46) Clough, B.; Dai, J.; Zhang, X.-C. *Mater. Today* **2012**, *15*, 50.
(47) Iwaszczuk, K.; Cooke, D. G.; Fujiwara, M.; Hashimoto, H.; Jepsen, P. U. *Opt. Express* **2009**, *17*, 21969.
(48) Knoesel, E.; Bonn, M.; Shan, J.; Wang, F.; Heinz, T. F. *J. Chem. Phys.* **2004**, *121*, 394.
(49) Knoesel, E.; Bonn, M.; Shan, J.; Heinz, T. F. *Phys. Rev. Lett.* **2001**, *86*, 340.
(50) Paolo, G.; Stefano, B.; Nicola, B.; Matteo, C.; Roberto, C.; Carlo, C.; Davide, C.; Guido, L. C.; Matteo, C.; Ismaila, D.; Andrea Dal, C.; Stefano de, G.; Stefano, F.; Guido, F.; Ralph, G.; Uwe, G.; Christos, G.; Anton, K.; Michele, L.; Layla, M.-S.; Nicola, M.; Francesco, M.; Riccardo, M.; Stefano, P.; Alfredo, P.; Lorenzo, P.; Carlo, S.; Sandro, S.; Gabriele, S.; Ari, P. S.; Alexander, S.; Paolo, U.; Renata, M. W. *J. Phys.: Condens. Matter* **2009**, *21*, 395502.
(51) Vanderbilt, D. *Phys. Rev. B* **1990**, *41*, 7892.
(52) Even, J.; Pedesseau, L.; Jancu, J.-M.; Katan, C. *J. Phys. Chem. Lett.* **2013**, *4*, 2999.
(53) MacDonald, A. H.; Vosko, S. H. *J. Phys. C: Solid State Phys.* **1979**, *12*, 2977.
(54) Rajagopal, A. K.; Callaway, J. *Phys. Rev. B* **1973**, *7*, 1912.
(55) Corso, A. D.; Conte, A. M. *Phys. Rev. B* **2005**, *71*, 115106.
(56) Perdew, J. P.; Burke, K.; Ernzerhof, M. *Phys. Rev. Lett.* **1996**, *77*, 3865.

(57) Monkhorst, H. J.; Pack, J. D. *Phys. Rev. B* **1976**, *13*, 5188.
(58) Wang, Y.; Gould, T.; Dobson, J. F.; Zhang, H.; Yang, H.; Yao, X.; Zhao, H. *Phys. Chem. Chem. Phys.* **2014**, *16*, 1424.
(59) Egger, D. A.; Kronik, L. *J. Phys. Chem. Lett.* **2014**, *5*, 2728.
(60) Grimme, S. *J. Comput. Chem.***2006**, *27*, 1787.
(61) Barone, V.; Casarin, M.; Forrer, D.; Pavone, M.; Sambi, M.; Vittadini, A. *J. Comput. Chem.* **2009**, *30*, 934.
(62) Baroni, S.; de Gironcoli, S.; Dal Corso, A.; Giannozzi, P. *Rev.Mod. Phys.* **2001**, *73*, 515.
(63) Young, K. F.; Frederikse, H. P. R. *J. Phys. Chem. Ref. Data* **1973**, *2*, 313.
(64) Mandal, P. K.; Chikan, V. *Nano Lett.* **2007**, *7*, 2521.
(65) Stoumpos, C. C.; Malliakas, C. D.; Peters, J. A.; Liu, Z.; Sebastian, M.; Im, J.; Chasapis, T. C.; Wibowo, A. C.; Chung, D. Y.; Freeman, A. J.; Wessels, B. W.; Kanatzidis, M. G. *Cryst. Growth Des.* **2013**, *13*, 2722.
(66) Nienhuys, H.-K.; Sundström, V. *Phys. Rev. B* **2005**, *71*, 235110.
(67) Lakowicz, J. *Principles of Fluorescence Spectroscopy*; 3rd Edition ed.; Springer: New York, 2006.
(68) Guglietta, G. W.; Diroll, B. T.; Gaulding, E. A.; Fordham, J. L.; Li, S.; Murray, C. B.; Baxter, J. B. *ACS Nano* **2015**, *9*, 1820.
(69) Smith, N. V. *Phys. Rev. B* **2001**, *64*, 155106.
(70) He, Y.; Galli, G. *Chem. Mater.* **2014**, *26*, 5394.
(71) Menéndez-Proupin, E.; Palacios, P.; Wahnón, P.; Conesa, J. C. *Phys. Rev. B* **2014**, *90*, 045207.
(72) Galkowski, K.; Mitioglu, A.; Miyata, A.; Plochocka, P.; Portugall, O.; Eperon, G. E.; Wang, J. T.-W.; Stergiopoulos, T.; Stranks, S. D.; Snaith, H. J.; Nicholas, R. J. *Energy & Environ. Sci.* **2016**, *9*, 962.
(73) Valverde-Chavez, D. A.; Ponseca, C. S.; Stoumpos, C. C.; Yartsev, A.; Kanatzidis, M. G.; Sundstrom, V.; Cooke, D. G. *Energy & Environ. Sci.* **2015**, *8*, 3700.
(74) Ng, S. M. S. a. K. K. *Physics of Semiconductor Devices*; 3rd Edition ed.; John Wiley & Sons. Inc., 2007.
(75) Chan, T.-L.; Zayak, A. T.; Dalpian, G. M.; Chelikowsky, J. R. *Phys. Rev. Lett.***2009**, *102*, 025901.
(76) Brandt, R. E.; Stevanović, V.; Ginley, D. S.; Buonassisi, T. *MRS Commun.* **2015**, *5*, 265.
(77) Koscher, B. A.; Swabeck, J. K.; Bronstein, N. D.; Alivisatos, A. P. *J. Am. Chem. Soc.* **2017**, *139*, 6566.
(78) Li, H.; Qian, Y.; Xing, X.; Zhu, J.; Huang, X.; Jing, Q.; Zhang, W.; Zhang, C.; Lu, Z. *J. Phys. Chem. C* **2018**, *122*, 12994.

Chapter 4

Carrier Dynamics in CsPbBr$_3$ Nanocrystal Film: Comparison between Single and Two-Photon Pumping

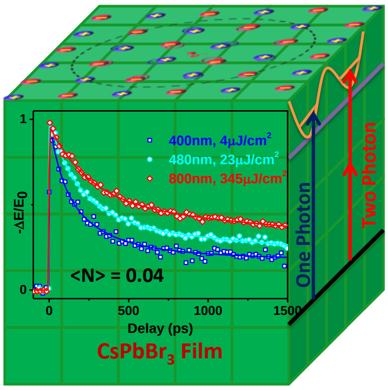

4.1 Introduction:

Cesium lead halide perovskite nanocrystals (NCs) have shown promises towards applications such as wavelength-tunable visible phosphors, single-photon sources, light emitting diodes (LEDs), photovoltaics, and lasers.[1-7] The success can be attributed to their exceptional photophysical properties, which partially originate from their unique electronic band structure.[8-12] Further, few ultrafast techniques have been employed to understand the carrier recombination dynamics, electron-hole transfer, fluorescence blinking, etc. which are directly related to the efficiency of photovoltaic and optoelectronic applications.[13-16] We reported a three-fold carrier recombination mechanism in a colloidal dispersion of $CsPbBr_3$ NCs, where the non-radiative trap-assisted carrier recombination was rather inefficient, probably resulting in those amazing properties.[17,18] Using optical-pump THz probe spectroscopy, we determined the intrinsic semiconductor properties of the NCs. A remarkably high carrier mobility ($\sim$4500 $cm^2V^{-1}s^{-1}$) and a rather long diffusion length (>9 μm) were determined from our transient AC photoconductivity results. However, these numbers/parameters are characteristics of individual NCs and do not reflect the actual device performances since all devices are solid/film based in the present generation. In the case of film, the overall carrier transport properties should depend on the inter-particle transport and long-range disorders in the medium, in addition to the intrinsic defects. Often grain boundaries act as trap centers and can localize charge carriers, thereby limiting the carrier transport properties. Hence, in the present work, we extended our study to NC-film to obtain a more practical understanding of carrier dynamics and related semiconductor properties related to device performance made out of these NCs. The film photoconductivity data reveals a carrier mobility two orders of magnitude lower than that in individual NCs.

Motivated by the success of linear optical properties, understanding of nonlinear optical properties have just begun in lead halide perovskites. $CsPbBr_3$ NCs exhibit strong two-photon absorption (TPA) cross-section, which is two orders of magnitude higher than conventional II-VI semiconductors, due to large size and high optical gain.[19-23] Nonlinear two-photon absorption (TPA) has several merits over linear one-photon absorption (OPA) such as high spatial resolution due to high skin depth, less damage to sample due to low energy of photons and also frequency upconverted lasers, where phase matching is relaxed.[19,20,24] These unique features make TPA phenomenon to be used in realistic applications such as bioimaging, three-dimensional microfabrication and microscopy.[25-28] First demonstration of feasibility of two-photon absorption in organic-inorganic lead halide perovskite was shown by Sargent et al. and later in the case of all-inorganic lead halide perovskite by Sun et al. and Xiao et al.[19,20,29] Despite the improvements in the photoluminescence quantum yield and solar cell efficiency, understanding the excited state properties/dynamics in these all inorganic lead halide perovskites under OPA and TPA are highly desirable, since the above-mentioned applications depends on the excited state dynamics. The dynamics under one and two-photon excitations are debated in the literature.[19,20,30-32] Recently, by employing time-resolved photoluminescence (TRPL) and femtosecond transient absorption spectroscopy (fs-TAS), it was shown that the PL is red-shifted and dynamics are slower in TPA compared to OPA.[19,30,32] Initially, it was attributed to reabsorption effect but in case of film it should not be as significant as in bulk single crystal. More recent studies revealed that selective absorption of larger NCs under TPA is the origin for such effect.[32] However, narrow linewidth indicates narrow size distribution but such narrow size distribution should slightly broaden full-width at half maximum in PL but should not shift the PL peak maxima.[7,15] It was also shown by TRPL that dynamics are similar under TPA and OPA.[20,31] Alternatively, it is possible to occupy different initial excitonic states under OPA and TPA and involve different relaxation pathways due to different parity selection rules involved.[33,34] TRPL and fs-TAS probe the charge carriers at band edges while initial excited state occupied by carriers under one and two-photon excitation are not known.

Time-resolved THz spectroscopy (TRTS) uses non-contact, low photon energy (1 THz = 4 meV), ac probe to get better insight into the nature of type carriers, free, localized, bound electron-hole pair (exciton) or polaron.[35-39] Very recently TRTS has been successfully used to reveal the nature of photoexcited carriers and their temporal evolution, recombination mechanisms and transport properties in organic-inorganic lead halide and some other perovskite materials.[40-44] Herein, we employ TRTS to study carrier dynamics in $CsPbBr_3$ NC film under one and two-photon pump excitations. Under similar excitonic conditions, TPA dynamics are slower compared with OPA.

Auger recombination, which is prominent at higher pump fluences in linear excitation, hardly affects the recombination under two-photon excitation. The mobilities and diffusion lengths obtained in our study are comparable with other lead halide perovskites studied by Herz and coworkers as well as Douhal and coworkers.[45,46]

4.2. Experimental section:

Colloidal $CsPbBr_3$ NCs were synthesized by the method proposed by Kovalenko and co-workers.[7] The NCs exhibit cubic morphology with edge length ~11nm and crystallizes in orthorhombic phase (see figure 4.1.A and Chapter 3). For both optical and THz measurements, a thin film on polystyrene substrate was made by spin coating the colloidal NCs (dispersed in toluene). The average thickness of the film was measured using a profilometer to be ~6.7 μm. Polystyrene substrate is transparent to both the optical pump (400 nm to 800 nm) and the THz (0.5 to 10 THz) probe light. The absorption spectrum of the film was recorded in reflection geometry and the first excitonic peak is at 508 nm, as shown in Figure 4.1.B., also indicates that the average size of these NC is 11nm.[15] The reduced absorption at 400 nm compared with first excitonic peak probably indicates scattering of light at shorter wavelengths. We neglect the effect of the scattering and reflection on the absorbance.[44] As is evident from the UV-Vis absorbance plot that the sample has no absorbance at 800 nm, indicates the observed dynamics in the case of 800 nm is due to multiphoton absorption, as is discussed in detail below. The experimental setup was enclosed in a box continuously purged with dry nitrogen to eliminate unwanted THz absorption by ambient moisture. All THz experiments were carried out at room temperature (298 K) and at a relative humidity level below 0.5%. To minimize the thermal effects the sample was moved slightly to a new spot for each scan.

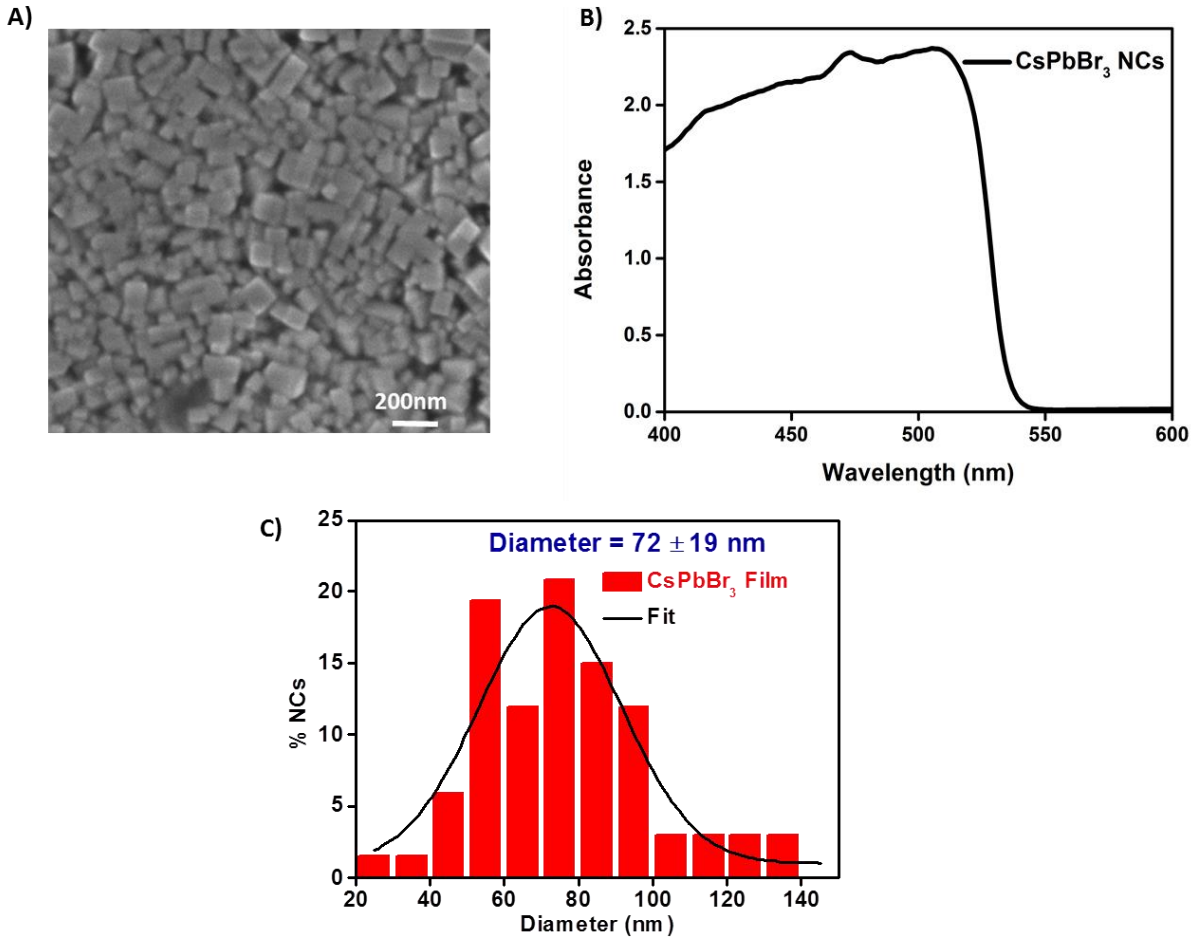

Figure 4.1. SEM image A) and absorption spectrum B) of $CsPbBr_3$ NCs deposited on polystyrene substrate exhibit cubic morphology and first excitonic peak at 508 nm. C) Size distribution plot for the film. Film shows large non-uniformity in particle size with an average size of 72±19 nm. This results in the absence of a clear sharp excitonic peak in the absorption spectrum (Figure 4.1.B).

4.3. Results & Discussion:

4.3.1. Phonon modes in $CsPbBr_3$ NCs film:

Prior to the pump-probe experiments, we recorded the time-domain THz spectrum of the NC film. Similar to THz waveforms obtained for $CsPbBr_3$ NC solution, the amplitude and shape of THz waveforms for NC film are different from those of the substrate. The THz waveforms, obtained through the substrate (polystyrene, PS) and NC film deposited on PS, are given in Figure 4.2.A. The change in the waveform is due to absorption and dispersion due to NCs deposited on PS substrate. The absorption spectrum of the NC film, shown in Figure 4.2.B, has a strong resonance at 3.0 THz due to IR active phonon modes.

From the computed IR spectra, the nature of the phonon modes was assigned, from our previous report,[17] mainly to anti-symmetric apical Pb-Br stretching, which occurs at slightly low THz frequencies (2.33 THz) and in-plane bending of Br-Pb-Br, which occur at high THz frequencies (2.9THz). However, in case of film, the nature of the THz absorption spectrum is slightly different from that of NC dispersion. The major peak is red-shifted by ~0.4 THz (13 cm^{-1}) and the overall spectrum is broadened with a prominent shoulder at ~1.4 THz. The softening of the phonon modes and the increase in the amplitude of the lower frequency modes may have occurred due to the physical coupling between individual NCs in the film. It will be certainly interesting to look at the effect of solvent on phonon frequencies. It is difficult to study carrier dynamics in various solvents using TRTS. Most solvents in which these colloidal nanocrystals can be dispersed either have aggressive absorber of THz radiation or not compatible with the window materials (TPX in the present study) used for optical pump THz probe experiments. Herein, we have used HMN (2, 2, 4, 4, 6, 8, 8-Hepta methyl nonane) solvent, which is quite transparent in the entire THz frequency range of our interest and also compatible with TPX. Hence, we couldn't perform solvent dependence study and

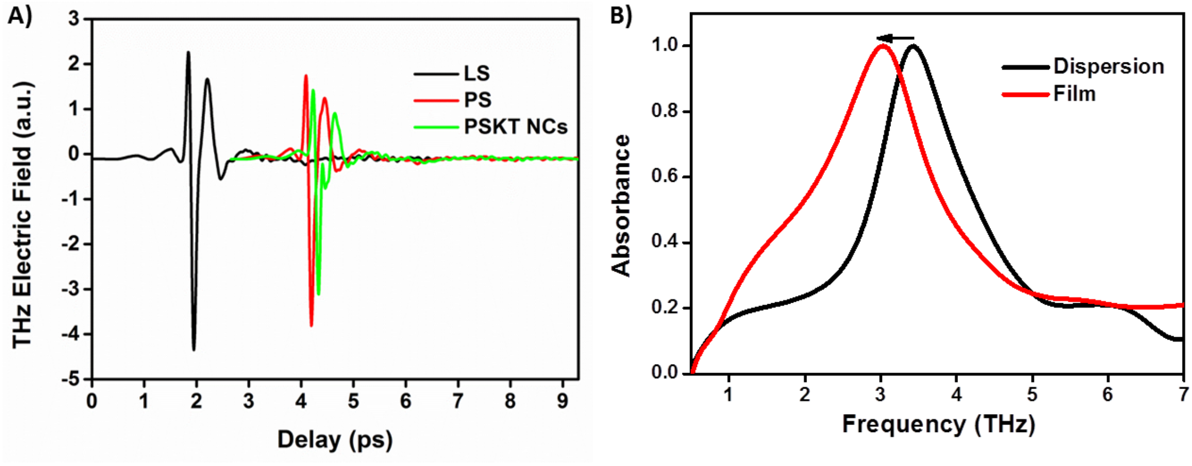

Figure 4.2. A) Time domain waveforms of the THz electric field passing through a vacuum (called LS), reference (polystyrene, PS) and $CsPbBr_3$ NCs (PSKT NCs) deposited on PS substrate. B) The absorption spectrum of $CsPbBr_3$ NC film obtained from the negative logarithm of ratios of amplitudes, obtained from the Fourier transform of electric fields passing through PS substrate and film deposited on PS. The phonon resonance in the film (red line) is slightly redshifted compared to NCs dispersed in HMN (black line).

unaware of the outcome of the effect of solvent on phonon frequency. However, we believe that the effect of solvent on phonon resonance was taken care of in colloidal $CsPbBr_3$ NCs by using effective medium theory. Hence, we are expecting the redshift in the phonon frequencies in film is due to coupling of smaller NCs to become bigger NCs, evident from the size distribution plot given in Figure. 4.1.C. Also, we haven't come across any report at least in perovskites where phonon frequencies are affected by solvent. The SEM image, given in Figure 4.1.A, clearly shows cubes of much larger dimensions in the film compared to the size of the colloidal nano-cubes (~11 nm, Chapter 3).

4.3.2. Time-Resolved Dynamics:

To gain insight into the nature of the carrier kinetics, the dynamics at three optical pump wavelengths 400, 480 and 800 nm were studied. The carriers generated at these pump wavelengths possess excess energy (EE) (EE_{400nm}= 640, EE_{480nm}=120 meV) and the same wavelengths were used in earlier studies to probe carrier dynamics in same NC solution. Probing carrier dynamics at same wavelengths in film and solution allows us to find out the role of the solvent in carrier recombination. In case of 400 and 480 nm pump wavelengths, an electron is promoted from the valence band to the conduction band by absorbing a single photon, whereas two photons are required using 800 nm (1.55 eV) pump light, given the bandgap of the material is at 508 nm (2.44 eV). In TRTS experiments, photoinduced change in THz transmission is proportional to the change in conductivity, which in turn, is proportional to the product of carrier density and mobility. So, a decrease in THz transmission or conductivity indicates a decrease in either carrier density or mobility or both. The carrier density decreases when the charge carriers recombine through different recombination processes and the mobility reduces when the charge carriers get trapped in low-mobility states. Figure 4.3.A shows pump-induced THz transmission traces at different pump wavelengths and fluences. In case of 800 nm pump light, the carrier recombination dynamics is slower compared to recombination dynamics in case of 400 and 480 nm pump even at very high pump fluence. This indicates that the higher order decay mechanisms are involved in OPA pumping. One may expect an average number of excitons generated to be less in the case of TPA since two-photon absorption cross-section is low compared to one-photon absorption cross-section. Further, one may also expect similar carrier dynamics under OPA and TPA excitation when the average number of excitons is same/similar, assuming that the initial excited state is same, as shown in Figure 4.7.A. Hence, it is essential to compare carrier dynamics under similar carrier generation condition. The average number of exciton per NC (<N>) generated under fluences of 289 μJ/cm^2 and 11 μJ/cm^2, in the case of TPA and OPA, respectively, is ~ 0.04. Herein, we hypothesize that under one and two-photon excitations carriers would access different initial excitonic states hence the observed discrepancy. To test our hypothesis the dynamics were monitored at a different wavelength. Here we use a 480 nm wavelength pump and an average number of excitons generated are ~0.05. The clear difference in dynamics, in case of 480 nm, indicates although carrier density is similar but they accessed different initial excitonic states and they relax differently. Such, discrepancy is also observed from frequency-resolved dynamics (see below).

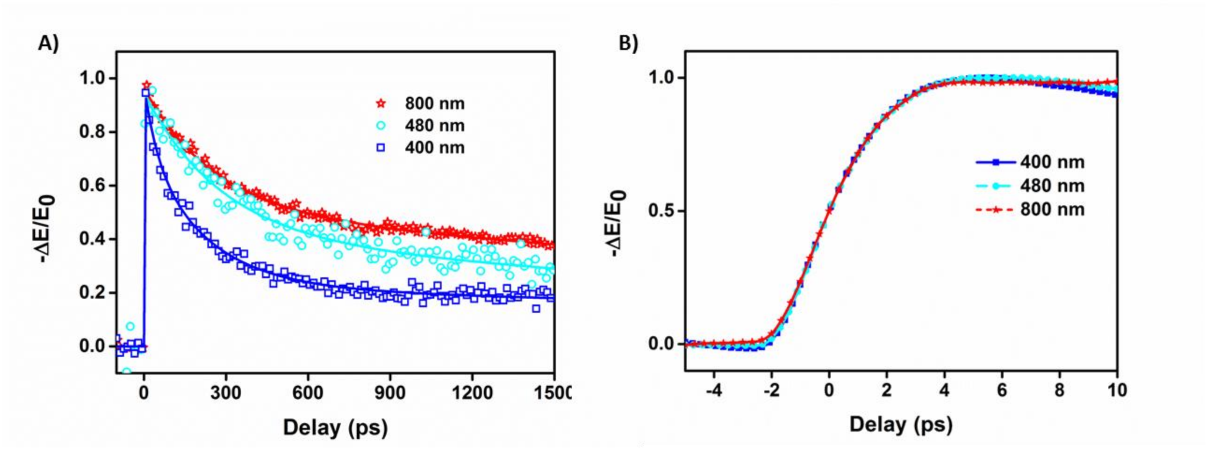

Figure 4.3: Pump induced change in THz transmission as a function of pump-probe delay A). THz transients at wavelengths 800 nm (289 μJ/cm^2), 480 nm (11 μJ/cm^2) and 400 nm (11 μJ/cm^2) B). THz transients obtained at early pump-probe delay at wavelengths 400 nm (60 μJ/cm^2), 480 nm(60 μJ/cm^2) and 800 nm (259 μJ/cm^2) (Note: symbol and its color is preserved to a particular wavelength throughout the manuscript; 800 nm: Star & Red, 480 nm: Circle & cyan and 400 nm: Square & Blue)

The normalized THz transients at early pump-probe delay times and at different wavelengths are shown in Figure 4.3.B. The slow rise time in THz conductivity probably indicates dissociation of excitons to free carriers and slightly large timescales (6-7 ps) indicates relatively large exciton binding energies observed in $CsPbBr_3$ NCs and variation in the steepness indicates different NC having different binding energies and they dissociate in different time scale. In contrast, in $CH_3NH_3PbI_3$ the maximum THz conductivity was obtained in less than 2 ps which corroborate the exciton binding energies observed in those materials.[42]

4.3.3. Peak conductivity and Initial mobility:

The peak conductivity of the $CsPbBr_3$ NC film has been calculated from the maximum of the photoinduced THz transmission using the following expression[47]

$$\Delta\sigma(t_p) = \frac{\varepsilon_0 c}{\delta}(n_a + n_b)\frac{-\Delta E(t_p)}{E_0(t_p)} \tag{4.1}$$

where δ is the photoexcited sample thickness, n_a, n_b are refractive indices of air and polystyrene substrate (n_a=1, n_b=1.556 (calculated from our TDS experiment)), ε_0 is the permittivity of free space and c is the speed of light. The photo excited sample thickness (δ) was estimated from the inverse of the absorption coefficient, which is given by, $\alpha = OD_\lambda/d$ where OD_λ is the absorbance at that particular wavelength, λ, and d is the film thickness. The linear absorbance at 800 nm is zero. Hence, we have calculated the absorbance in the case of 800 nm, under two-photon absorption, by measuring transmitted power through the sample at variable incident intensities. The conductivity values obtained at pump wavelengths 400, 480 and 800 nm for various fluences vary from 20 to 48 S/m, 8 to 84 S/m, and 1 to 45 S/m, respectively. The initial effective mobilities (φμ) from the given conductivity values can be calculated as $\varphi\mu \cong \frac{\Delta\sigma}{qN_0}$ where φμ is the effective mobility, φ is the photon to free carrier conversion ratio, q is the elementary charge, and N_0 is the number of carriers generated upon photon absorption. Assuming that every absorbed photon results in one electron-hole pair, i.e. φ = 1, number of free carriers generated under one photon condition are $N_0 = 2N_p$ and in case of two-photon absorption, $N_0 = N_p$, where N_p is the number of absorbed photons. N_p can be determined from the absorbance at the pump wavelength as $N_p = F_l(1-10^{-OD_\lambda})/\delta h\nu$, where F_l is the pump fluence and $h\nu$ is the single-photon energy. Further, the absorbance in TPA is calculated from the two-photon absorption coefficient (β) as $A = 1 - \frac{1}{1+\beta I_0 L}$, where I_0 is the incident light intensity and L is the thickness of the film. Here, the value of $\beta(= 11cm/GW)$ is taken from the literature and linear absorption is neglected.[23] It was shown that, the TPA absorption coefficient does not show strong size dependence in $CsPbBr_3$ NCs. The value vary from 6.5 cm/GW for 4.6 nm size particles, which are in strong confinement limit given the Bohr diameter of exciton in these NCs is 7 nm, to 12.5 cm/GW for 11.5 nm size particles, which are in very weak confinement regime i.e. in bulk limit. Since we neglect the reflection and scattering losses, the obtained carrier densities are higher bound, and the mobilities are lower bound.

THz transients obtained at pump wavelengths 400 and 480 nm for various fluences are shown in Figure 4.5. To assign different processes involved in the carrier recombination mechanism, their relative contribution, and respective timescales, the measured THz transients were fitted to a multiexponential function convoluted with the Gaussian function of the form[48]

$$y = G(t - t_0)\otimes \sum_i a_i \exp\left[-\frac{t - t_0}{\tau_i}\right] \qquad (4.2)$$

where $G(t - t_0)$ is the Gaussian function centered at t_0 and a_i represents the contribution of the ith decay channel with a time constant τ_i towards total recombination kinetics.

The carrier dynamics obtained with 400 nm pump fit well with a tri-exponential function and the three de-excitation mechanisms were assigned according to the previous literature.[17] The dynamics become very slow (almost parallel to the delay axis) at the longer pump-probe delay and determining the time constant of this slow component with certainty is not possible because of the limitation in the temporal window (maximum attainable temporal window is ~1.6 ns) of our experiments. The longest time constant was varied between 3 and 8 ns, obtained from PL measurements, to fit the THz transients. In TRPL, assuming that at low fluences, kinetics mainly follow mono-molecular recombinations. In case of 400 nm pump, the data fit well by taking the slowest time constant as 7 ns (τ_1). The THz transients at higher fluences were fitted to the multiexponential function keeping the slowest time constant fixed at 7 ns and other decay channel parameters were derived. The other two average time constants (τ_3 and τ_2) obtained are ~60 ps, ~250 ps and are higher than those determined in colloidal dispersion (Chapter 3). The time constant τ_1 is attributed to trap-assisted recombination, τ_2 to the two-body recombination and τ_3 to the Auger recombination. Whereas in the case of 480 nm THz transients were well fit with bi-exponential at lower fluence (11 μJ/cm^2) and need tri-exponential at higher fluences. The slowest time constant found at lowest fluence for 480 nm pump wavelength is 4 ns. However, all THz transients, as shown in Figure 4.8.A, in case of 800 nm fitted well with bi-exponential, even under similar or more exciton generation condition, and the lowest time constant is 5 ns. The absence of the third de-excitation mechanism, such as Auger recombination, is surprising given that Auger recombination is dominant at higher fluence.[17] The absence of higher order recombination processes at higher fluence indicates it being a promising material as a gain media in lasing applications. These low time constants obtained at lowest fluences even matches well with earlier reports of dynamics study at low fluences.[15] The fitting parameters for all wavelengths at different fluences are given at the end of the chapter in Table 3.

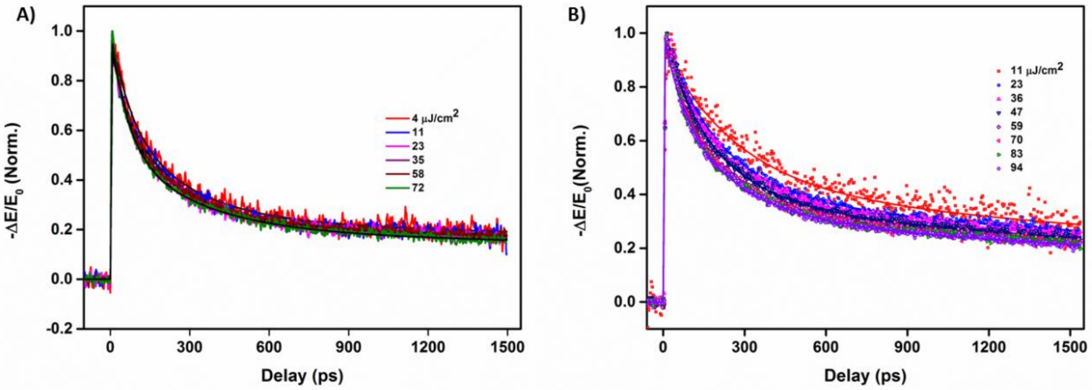

Figure 4.5: Pump induced change in THz transmission and their fit with multiexponential decay as a function of pump-probe delay at different pump fluences A) THz transients at 400 nm B) THz transients at 480 nm.

4.3.4. THz dynamics at 800 nm:

We have measured the peak THz transients ($-\Delta E/E_0$) at different fluences (Fl) under two-photon excitation by 800 nm pump. The amplitude of THz transients depends on the number of carriers generated. The measured peak THz field ($-\Delta E/E_0$) of the transients at different fluences are shown in Figure 4.6. The peak THz field vs fluence data points were fitted to the equation: $-\Delta E/E_0 = CFl^n$, where, Fl is the pump (800 nm) fluence, and the best fit was obtained for n=1.97, as shown by the red solid line in Figure 4.6. The near quadratic nature of initial THz transients/peak conductivity with increasing fluence indicates that TPA indeed is taking place.

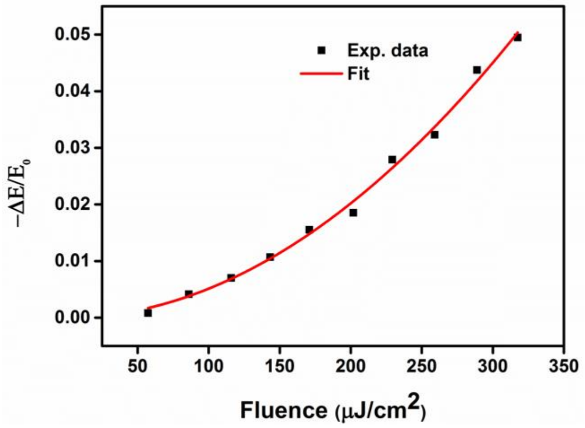

Figure 4.6: Initial peak THz transients vs. fluences and fit with equation $-\Delta E/E_0 = CFl^n$. The best fit was obtained with n = 1.97 and indicates the quadratic nature.

The mobilities, which are lower bound as explained above, obtained from peak conductivity at different fluences of under OPA (400 and 480 nm) and TPA (800 nm), are shown in Figure 4.8.B. The difference in the carrier density dependence of mobility indicates that the nature of the initial excited state accessed under OPA and TPA are possibly different. Earlier, the discrepancy in carrier decay kinetics was explained based on the size inhomogeneity and reabsorption effect.[30,32] Although, one would expect re-absorption effect (emission of light from small NCs to be absorbed by the large NCs due to a smaller band gap in large NC) can be the origin for such a discrepancy, Chen et. al. revealed that by changing the concentration of solution one would not see such shift, may be due to, at very low concentration the distance between NC increases and the light emitted by one NC cannot be absorbed by another NC.[32] However, even at very low concentration they observed such shift. Further, Han *et al.,* showed by using TRPL that there is no systematic change in peak shift and FWHM of PL, opposite to the expected trend. Hence, we exclude reabsorption to be the origin for such discrepancy. Alternatively, Chen *et al.* explained the observed dynamics with size inhomogeneity.[32] If the observed shift is only due to size inhomogeneity, one would expect slower kinetics as well as PL shift. However, they did not observe such PL shift in the case of large NCs (~11 nm). Herein, our study clearly shows dynamics with one and two-photon excitations are different even in 11 nm sized NCs; dynamics are faster in OPA excitation whereas it is slow under TPA excitation. Therefore, we propose that carriers under OPA and TPA occupy different initial states having same/similar energy due to the difference in selection rule for one and two-photon absorption (see Figure 4.7.B). Further, it is also possible that the occupied states under OPA are delocalized and under TPA states are localized, such as traps. The parameters obtained by fitting THz transients to a multi-exponential function also support the observed decay. The fitting parameters obtained at similar exciton condition are given in Table 1. As discussed above, the contribution of the slowest time constant, which represents the trap-assisted recombination, is more in TPA (51%) than OPA (22%). These results are in line with the observed PL shift and slower dynamics in the same material by Han et.al. where the authors predicted more than a single excited state.[30] Such PL shift was also predicted in single crystal $CsPbBr_3$ and was attributed to different initial excited state due to different selection rules for OPA and TPA.[33] However, the applicability of such selection rules in case of NCs needs to be validated further.

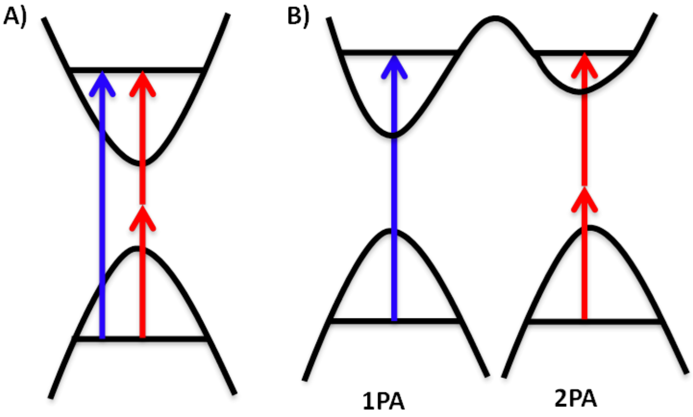

Figure 4.7: Schematic of one and two photon absorption showing when carriers accessed to the same initial excited state A) and when accessed to different initial excited state B).

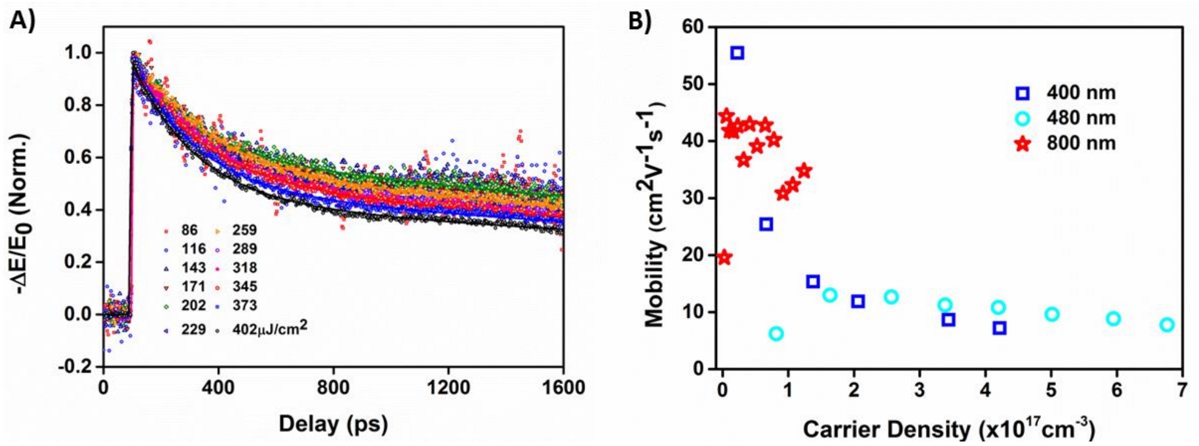

Figure 4.8: A) THz transients obtained under two-photon excitation (800 nm) at various pump fluences B) Comparison of mobilities obtained at different wavelengths as a function of carrier density generated at the particular fluences used in the experiment.

Table 4.1: Parameters obtained from fitting the THz transients to multiexponential function at similar exciton condition.

Wavelength (nm)	Fluence (μJ/cm²)	<N>	t_1 (ns)	a_1	t_2 (ps)	a_2	t_3 (ps)	a_3
400	11	0.04	7	0.22 (0.0)	222 (0.5)	0.5 (0.0)	47 (0.4)	0.22 (0.0)
800	289	0.04	5	0.51 (0.0)	253 (0.2)	0.45 (0.0)	---	---

Values in the parenthesis are deviations in the fit

4.3.5. Frequency-Resolved conductivity:

We can also derive the carrier density and mobility from frequency-resolved TRTS experiments (probe-scan) where we record the complete THz waveforms at different pump-probe delays. Analysis of the probe-scan data yields the photo-induced complex conductivity spectra as a function of time after photo-excitation (see chapter 2 for details). Further, the conductivity spectra are fitted to a conductivity model appropriate for the system. The complex conductivity spectra thus obtained for the $CsPbBr_3$ film at different pump-probe delays after the photoexcitation with the 400 nm pump are shown in Figure 4.9. The negative imaginary conductivity and strong phonon feature at

3.4 THz lead us to use one Lorentz oscillator and the Drude-Smith model to fit the conductivity spectra,[49] as shown in Figure 4.9.A for 5 ps delay. See Chapter 2 for the functional form of Lorentz and Drude-Smith model and related discussions. According to the Drude-Smith model, the parameter C indicates whether carriers are localized or free.[50] For localized carriers, the parameter C = -1 and imaginary conductivity becomes negative, whereas, for free carriers, C = 0 and imaginary conductivity becomes zero. The localization of the carriers can take place due to defects or backscattering from the interface/grain boundaries. At first, the nature of the conductivity spectra in the film is slightly different from those observed in colloidal dispersion (Chapter 3). However, one should note that in the film, the conductivity is measured across the NCs, whereas in solution the conductivity was obtained within the NCs by using simple effective medium theory. Further, the nature of the conductivity in 800 nm pump is similar to 400 nm pump and is shown in Figure 4.10. It indicates the charge carriers generated are same in both the cases.

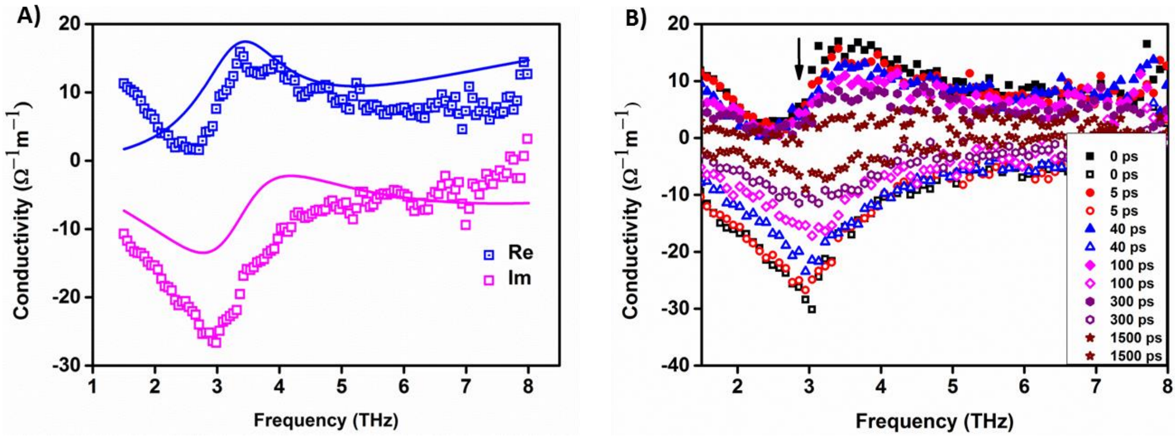

Figure 4.9: A) Frequency-resolved complex conductivity spectrum at 5 ps pump-probe delay after photoexcitation with 400 nm pump. Solid lines are a fit of the experimental data to the Drude-Smith-Lorentz model. B) Frequency-resolved conductivity at various pump-probe delays for 400 nm wavelength.

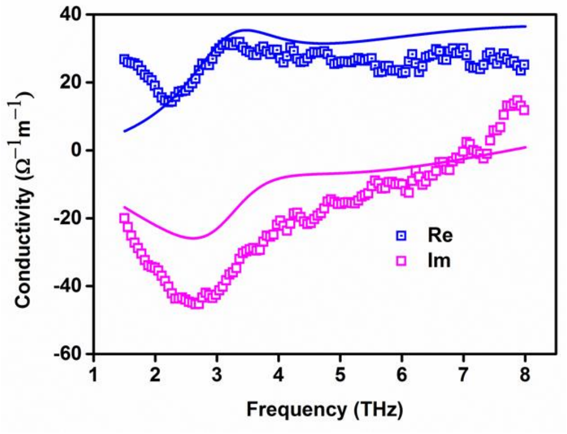

Figure 4.10: Frequency-resolved complex conductivity spectrum at 5 ps pump-probe delay after photoexcitation with 800 nm pump. Solid lines are a fit of the experimental data to the Drude-Smith-Lorentz model.

One would expect that grain boundaries present in the polycrystalline film can play a major role in the localization of carriers, however, theoretical calculations show that at worst scenario, these NCs can form shallow trap states rather than midgap traps. Generally, midgap states arise from interstitial or antisite misplaced atoms (point defects), which requires a high energy of formation than the parent perovskite material; hence perovskites are not prone to form such midgap defects.[9-11] It is more likely that the strong resonance at 3.0 THz is due to polaron formation. Polaron is a carrier confined by the potential that is created by the polarization of the lattice due to the presence of a charged particle. Polaron formation is highly likely in these perovskite materials due to their soft ionic nature of the lattice, so the lattice can easily get distorted. Hence it is likely that initially large number of polarons are generated, subsequently, those polarons recombine and reduce the amplitude of peak resonance as shown in figure 4.9.B. Recently, Miyata *et al.* explained defect tolerance responsible for excellent optical properties in both organic and inorganic halide perovskites by using the concept of polaron.[51] The strength of the electron-phonon coupling can be expressed with Fröhlich parameter (α_{e-Ph}),[52] a dimensionless quantity, which can be calculated from the following formula

$$\alpha_{e-Ph} = \frac{e^2}{\hbar}\frac{1}{4\pi\epsilon}\left(\frac{1}{\varepsilon_{opt}} - \frac{1}{\varepsilon_s}\right)\sqrt{\frac{m^*}{2\hbar\omega_{LO}}} \qquad (4.3)$$

where $\hbar$ is the reduced Planck's constant, ϵ is the vacuum permittivity, ε_{opt} , ε_s are dielectric constants at optical and static limits, m^* is the band edge effective mass and $\omega_{LO} = 2\pi\vartheta_{LO}$ the angular frequency of longitudinal optical phonon.

The obtained α_{e-Ph} values are given in Table 2. The value $\alpha_{e-Ph}< 6$ indicates that the generated polaron is intermediate to large and extended to several unit cells as opposed to the small polaron ($\alpha_{e-Ph} > 6$) confined to single unitcell. These large polarons are less likely to undergo recombination with traps.[51,53,54] The strong phonon mode absorption in our study is mainly IR-active whereas Miyata *et al.* observed the phonon mode at 4.07 THz in time-resolved optical Kerr effect (TR-OKE) spectroscopy. In TR-OKE experiment the observed phonon modes are Raman active. Recently, it was shown that dynamic disorder due to twin boundaries form different domains within the NCs.[55] These twin boundaries also can localize charge carriers. From all these, we conclude that dynamic disorder and strong electron/hole–phonon coupling (large polaron) both are responsible for the observed nature of the conductivity. Recently, by using TRTS, Ziwrtsch *et al.* and Butler *et al.* observed a similar spectral signature in $BiVO_4$, a photoanode material.[37,38] However, the resonance are due to small polarons, which limit charge carrier mobility to < 1 $cm^2V^{-1}s^{-1}$.[37] Very recently, evidence of polaron formation in $CH_3NH_3PbI_3$ perovskite was observed using transient absorption and femtosecond impulsive stimulated Raman spectroscopy.[56]

Table 4.2: Frölich electron-phonon coupling parameters obtained from phonon resonance frequency and dielectric constant

Material	ε_{opt}	ε_s	ϑ_{LO}(THz)	α_{e-Ph}	Mobility ($cm^2V^{-1}s^{-1}$)	Technique
$CsPbBr_3$-e	4#	15.61#	3.4**	2.72	~40-160	TRTS (Present work)
$CsPbBr_3$-h				2.84		
$CsPbBr_3$-e[51]	4.3	29.37	4.07	2.64	48.2	TR-OKE
$CsPbBr_3$-h[51]				2.76	41.3	

$CH_3NH_3PbBr_3$[57]	4.7	32.3	1.53, 5.01	1.69	158	Far-IR
GaAs[58]	--	--	--	0.068	7000	--

** Value taken from time domain THz spectrum (Figure 4.2.B).

Values taken from our previous chapter, 3.

From the fitting of the conductivity spectra, the obtained carrier density and mobility are plotted as a function of delay for both 400 and 800 nm and are given in Figure 4.11. Here also, we can clearly see that the dynamics are slower in the case of TPA compared to that in the case of OPA. This observation further confirms our hypothesis that the carriers are excited to different initial excited states under OPA and TPA. Mobilities (μ) obtained from frequency-resolved dynamics are higher than the effective initial mobilities (φμ) obtained from the frequency-averaged peak THz transients by a factor of 3. The higher mobilites derived from frequency-resolved conductivity compared to mobilities obtained from peak conductivity can be due to the inadequacy of the models which we have employed here. It is evident that the quality of the fits is not that good. We need to probe further in this regard.

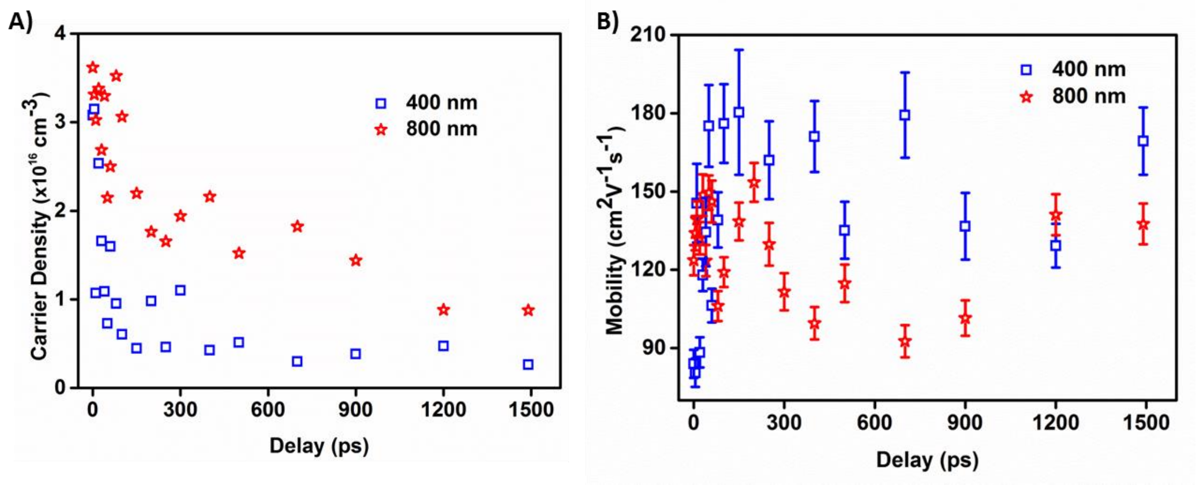

Figure 4.11: Comparison of A) carrier densities and B) mobilities between 400 and 800 nm under similar average exciton density obtained from frequency-resolved conductivity at different pump-probe delays.

4.3.6 Comparison of mobilities:

The mobilities obtained in CsPbBr$_3$ NCs film, which is polycrystalline in nature, are less than the mobility obtained for NC solution and a single crystal of the same material by an order of magnitude.[17,59] The discrepancy can be attributed to long-range disorder and grain boundaries present in the film which limits the mobility and even similar discrepancy was observed in $CH_3NH_3PbBr_3$ single crystal and polycrystalline film.[60,61] Care must be taken while doing an experiment to avoid sample degradation or to avoid thermal effects. Such effects can add artifacts in the data, for example, PL was completely quenched under intense light.[3] The reduced mobilities with increasing carrier concentration can be attributed to carrier-carrier and/or carrier-ion core interaction which randomizes their motion.

4.3.7 Diffusion Length (L_D):

Diffusion length is one of the key parameters which influence the efficiency of the solar cell and its value can be estimated from the given initial mobility and an average lifetime as $L_D = \sqrt{(\langle\tau\rangle \mu k_B T/q)}$; where μ is the initial mobility, k_B is the Boltzmann constant, q is the elementary charge and $\langle\tau\rangle$ is the average life time (which can be derived from, $\langle\tau\rangle = \frac{\sum_i a_i \tau_i^2}{\sum_i a_i \tau_i}$ where a_i is the amplitude and τ_i is the life time of ith decay channel).[62] The diffusion lengths at various initial carrier densities for 400, 480 and 800 nm pump wavelengths are plotted in Figure 4.12, and vary between 0.3 um to 1 um. These values are a lower limit since the initial mobilities are lower limits and accuracy of these values again depends on the photon to free carrier conversion ratio (φ). The diffusion lengths obtained under two-photon absorption are very similar to that for one-photon absorption at similar carrier densities. It is to be noted that the nature of the diffusion lengths for OPA and TPA (barring one point in TPA) are same and are different for 480 nm pump. It may be possible that with 480 nm pump excitation, initially charge carriers are trapped in trap-states. This results to a modest initial diffusion length of charge carriers, and increases with an increase in pump fluence because the charge carriers can access the delocalized bands after all the trap-states are filled. However, after certain threshold fluence carrier-carrier and carrier-lattice interactions dominate and as a result diffusion length starts decreasing. One would expect a similar trend for both 400 and 800 nm excitation as well. In case of OPA and TPA, due to the excess kinetic energy available to the carriers the carrier-carrier and carrier-lattice scattering is significantly high. This results to a steadily reducing diffusion lengths rather than initial increase and consequent decrease.

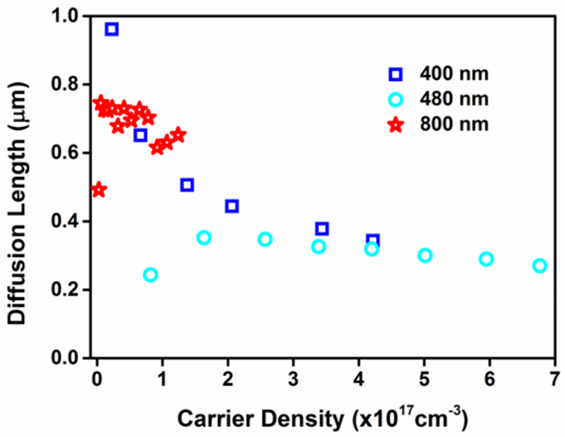

Figure 4.12: Diffusion length as a function of carrier density generated at the optical pump powers used in the experiments.

Table 4.3: Parameters obtained from THz transients fitted with a multiexponential function

Wavelength (nm)	Fluence ($\mu J/cm^2$)	<N>	τ_1 (ps)	a_1	τ_2 (ps)	a_2	τ_3 (ps)	a_3
400	4	0.015	7000	0.24	249.3	0.46	67.4	0.30
				(0.00)	(1.0)	(0.002)	(0.6)	(0.002)
	11	0.044	7000	0.22	221.9	0.51	47.0	0.22
				(0.00)	(0.5)	(0.001)	(0.4)	(0.001)
	23	0.092	7000	0.21	266.7	0.35	76.1	0.38
				(0.00)	(1.1)	(0.002)	(0.4)	(0.002)
	35	0.137	7000	0.22	255.2	0.42	60.2	0.34
				(0.00)	(0.6)	(0.001)	(0.3)	(0.001)
	58	0.229	7000	0.20	281.1	0.37	60.5	0.40
				(0.00)	(0.7)	(0.001)	(0.2)	(0.001)
	72	0.281	7000	0.19	300.8	0.36	64.0	0.43
				(0.00)	(0.8)	(0.001)	(0.2)	(0.001)
	11	0.054	4000	0.42	275.7	0.52	---	---
				(0.00)	(0.5)	(0.00)		
	23	0.109	4000	0.39	238.5	0.46	122.2	0.14

				(0.00)	(2.4)	(0.014)	(4.5)	(0.013)
480	36	0.171	4000	0.36	258.4	0.38	122.8	0.25
				(0.00)	(2.6)	(0.01)	(2.1)	(0.01)
	47	0.225	4000	0.35	262.8	0.38	112.4	0.26
				(0.00)	(1.9)	(0.006)	(1.3)	(0.006)
	59	0.279	4000	0.32	285.7	0.32	107.9	0.33
				(0.00)	(1.8)	(0.004)	(0.7)	(0.004)
	70	0.334	4000	0.31	264.4	0.39	85.0	0.28
				(0.00)	(1.0)	(0.002)	(0.6)	(0.002)
	83	0.396	4000	0.32	238.6	0.41	81.2	0.25
				(0.00)	(0.9)	(0.003)	(0.6)	(0.003)
	94	0.45	4000	0.31	248.0	0.41	76.7	0.25
				(0.00)	(0.8)	(0.002)	(0.5)	(0.002)
800	57	0.002	5000	0.20	156.7	0.25	---	---
				(0.001)	(2.6)	(0.002)		
	86	0.004	5000	0.47	195.1	0.32	---	---
				(0.00)	(1.1)	(0.001)		
	116	0.007	5000	0.60	160.4	0.35	---	---
				(0.00)	(0.6)	(0.001)		
	143	0.011	5000	0.61	187.2	0.35	---	---
				(0.00)	(0.4)	(0.00)		
	171	0.015	5000	0.60	202.2	0.39	---	---
				(0.00)	(0.3)	(0.00)		
	202	0.021	5000	0.61	219.03	0.37	---	---
				(0.00)	(0.3)	(0.00)		
	229	0.027	5000	0.53	249.1	0.41	---	---
				(0.00)	(0.2)	(0.00)		
	259	0.035	5000	0.55	269.2	0.44	---	---
				(0.00)	(0.3)	(0.00)		
	289	0.043	5000	0.51	252.6	0.45	---	---
				(0.00)	(0.2)	(0.00)		
	318	0.052	5000	0.51	258.0	0.47	---	---
				(0.00)	(0.2)	(0.00)		

	345	0.061	5000	0.50 (0.00)	253.5 (0.2)	0.46 (0.00)	---	---
	373	0.071	5000	0.48 (0.00)	217.8 (0.2)	0.52 (0.00)	---	---
	402	0.082	5000	0.44 (0.00)	218.3 (0.1)	0.54 (0.00)	---	---

4.4 Conclusions:

In summary, by employing time-resolved THz spectroscopy, we have probed carrier dynamics under linear (OPA) and nonlinear (TPA) pump wavelengths. The kinetics is slower in case of two-photon excitation compared to one photon, confirmed by both frequency-averaged and frequency-resolved experiments. The Lorentz oscillator at 3.4 THz originates mainly due to strong carrier-phonon coupling, which results in large polaron formation. In case of TPA, carriers access different state with energy similar to the state accessed by the carriers under OPA. Polarons/intrinsic disorder can limit the mobilities and diffusion lengths but their effect is not very detrimental due to the large nature of the polarons. The mobilities and diffusion lengths in the film are comparable to other lead halide perovskites and suggest that there are no fundamental obstacles in using these NCs in optoelectronic and photovoltaic applications.

In immediate future we should focus in the direction of retaining the similar transport properties in CsPbBr$_3$ NC film, as observed in the colloidal NCs. One way to approach at it is by post-synthetic treatment of the film. Changing the surface ligands may improve the conductivity as well as mobilities. Recently, Sarkar et al. (from our group) performed one such study on CsPbI$_3$ NCs. When the drop-cast film treated with methyl acetate and lead acetate, mobilities were increased by orders of magnitude. This study clearly indicates that inter-dot coupling increases when the insulating long-chain oleylamine ligands are removed, which in turn increases the conductivity and mobility. Although we performed a detailed study on CsPbBr$_3$ NCs, an in-depth study is required in future to look at dynamics by varying the compositions of A cations and halides (X) in ABX$_3$ perovskites. Recently, it was shown that the power conversion efficiency was increased greater than 20% when mixed cation and mixed anion composition was employed.[63]

4.5 References:

(1) Yakunin, S.; Protesescu, L.; Krieg, F.; Bodnarchuk, M. I.; Nedelcu, G.; Humer, M.; De Luca, G.; Fiebig, M.; Heiss, W.; Kovalenko, M. V. *Nat .Commun.* **2015**, *6*.
(2) Wang, Y.; Li, X.; Song, J.; Xiao, L.; Zeng, H.; Sun, H. *Adv. Mater.* **2015**, *27*, 7101.
(3) Park, Y.-S.; Guo, S.; Makarov, N. S.; Klimov, V. I. *ACS Nano* **2015**, *9*, 10386.
(4) Zhang, X.; Lin, H.; Huang, H.; Reckmeier, C.; Zhang, Y.; Choy, W. C. H.; Rogach, A. L. *Nano Lett.* **2016**, *16*, 1415.
(5) Swarnkar, A.; Ravi, V. K.; Nag, A. *ACS Energy Lett.* **2017**, *2*, 1089.
(6) Huang, H.; Bodnarchuk, M. I.; Kershaw, S. V.; Kovalenko, M. V.; Rogach, A. L. *ACS Energy Lett.* **2017**, *2*, 2071.
(7) Protesescu, L.; Yakunin, S.; Bodnarchuk, M. I.; Krieg, F.; Caputo, R.; Hendon, C. H.; Yang, R. X.; Walsh, A.; Kovalenko, M. V. *Nano Lett.* **2015**, *15*, 3692.
(8) Brandt, R. E.; Stevanović, V.; Ginley, D. S.; Buonassisi, T. *MRS Commun.* **2015**, *5*, 265.
(9) Guo, Y.; Wang, Q.; Saidi, W. A. *J. Phys. Chem. C* **2017**, *121*, 1715.
(10) Kang, J.; Wang, L.-W. *J. Phys. Chem. Lett.* **2017**, *8*, 489.
(11) ten Brinck, S.; Infante, I. *ACS Energy Lett.* **2016**, *1*, 1266.
(12) Dirin, D. N.; Protesescu, L.; Trummer, D.; Kochetygov, I. V.; Yakunin, S.; Krumeich, F.; Stadie, N. P.; Kovalenko, M. V. *Nano Lett.* **2016**, *16*, 5866.
(13) Wu, K.; Liang, G.; Shang, Q.; Ren, Y.; Kong, D.; Lian, T. *J. Am. Chem. Soc.* **2015**, *137*, 12792.
(14) Seth, S.; Mondal, N.; Patra, S.; Samanta, A. *J. Phys. Chem. Lett.* **2016**, *7*, 266.
(15) Swarnkar, A.; Chulliyil, R.; Ravi, V. K.; Irfanullah, M.; Chowdhury, A.; Nag, A. *Angew. Chem. Int. Ed.* **2015**, *54*, 15424.
(16) Sarkar, S.; Ravi, V. K.; Banerjee, S.; Yettapu, G. R.; Markad, G. B.; Nag, A.; Mandal, P. *Nano Lett.* **2017**, *17*, 5402.
(17) Yettapu, G. R.; Talukdar, D.; Sarkar, S.; Swarnkar, A.; Nag, A.; Ghosh, P.; Mandal, P. *Nano Lett.* **2016**, *16*, 4838.
(18) Mondal, N.; Samanta, A. *Nanoscale* **2017**, *9*, 1878.
(19) Xu, Y.; Chen, Q.; Zhang, C.; Wang, R.; Wu, H.; Zhang, X.; Xing, G.; Yu, W. W.; Wang, X.; Zhang, Y.; Xiao, M. *J. Am. Chem. Soc.* **2016**, *138*, 3761.
(20) Wang, Y.; Li, X.; Zhao, X.; Xiao, L.; Zeng, H.; Sun, H. *Nano Lett.* **2016**, *16*, 448.
(21) Pu, S.-C.; Yang, M.-J.; Hsu, C.-C.; Lai, C.-W.; Hsieh, C.-C.; Lin, S. H.; Cheng, Y.-M.; Chou, P.-T. *Small* **2006**, *2*, 1308.
(22) Dakovski, G. L.; Shan, J. *J. Appl. Phys.* **2013**, *114*, 014301.
(23) Chen, J.; Žídek, K.; Chábera, P.; Liu, D.; Cheng, P.; Nuuttila, L.; Al-Marri, M. J.; Lehtivuori, H.; Messing, M. E.; Han, K.; Zheng, K.; Pullerits, T. *J. Phys. Chem. Lett.* **2017**, *8*, 2316.
(24) He, G. S.; Tan, L.-S.; Zheng, Q.; Prasad, P. N. *Chem. Rev.* **2008**, *108*, 1245.
(25) Zhang, X.-X.; Wu, H.; Li, P.; Qu, Z.-J.; Tan, M.-Q.; Han, K.-L. *Chem. Commun.* **2016**, *52*, 8283.
(26) Sun, W.; Fan, J.; Hu, C.; Cao, J.; Zhang, H.; Xiong, X.; Wang, J.; Cui, S.; Sun, S.; Peng, X. *Chem. Commun.* **2013**, *49*, 3890.
(27) Cumpston, B. H.; Ananthavel, S. P.; Barlow, S.; Dyer, D. L.; Ehrlich, J. E.; Erskine, L. L.; Heikal, A. A.; Kuebler, S. M.; Lee, I. Y. S.; McCord-Maughon, D.; Qin, J.; Röckel, H.; Rumi, M.; Wu, X.-L.; Marder, S. R.; Perry, J. W. *Nature* **1999**, *398*, 51.
(28) Denk, W.; Strickler, J. H.; Webb, W. W. *Science* **1990**, *248*, 73.
(29) Walters, G.; Sutherland, B. R.; Hoogland, S.; Shi, D.; Comin, R.; Sellan, D. P.; Bakr, O. M.; Sargent, E. H. *ACS Nano* **2015**, *9*, 9340.

(30) Han, Q.; Wu, W.; Liu, W.; Yang, Y. *RSC Adv.* **2017**, *7*, 35757.
(31) Chen, W.; Bhaumik, S.; Veldhuis, S. A.; Xing, G.; Xu, Q.; Grätzel, M.; Mhaisalkar, S.; Mathews, N.; Sum, T. C. *Nature Commun.* **2017**, *8*, 15198.
(32) Chen, J.; Chábera, P.; Pascher, T.; Messing, M. E.; Schaller, R.; Canton, S.; Zheng, K.; Pullerits, T. *J. Phys. Chem. Lett.* **2017**, *8*, 5119.
(33) Clark, D. J.; Stoumpos, C. C.; Saouma, F. O.; Kanatzidis, M. G.; Jang, J. I. *Phys. Rev. B* **2016**, *93*, 195202.
(34) Saouma, F. O.; Stoumpos, C. C.; Kanatzidis, M. G.; Kim, Y. S.; Jang, J. I. *J. Phys. Chem. Lett.* **2017**, *8*, 4912.
(35) Baxter, J. B.; Guglietta, G. W. *Anal. Chem.* **2011**, *83*, 4342.
(36) Němec, H.; Kužel, P.; Sundström, V. *J. Photochem. Photobiol. A: Chemistry* **2010**, *215*, 123.
(37) Ziwritsch, M.; Müller, S.; Hempel, H.; Unold, T.; Abdi, F. F.; van de Krol, R.; Friedrich, D.; Eichberger, R. *ACS Energy Lett.* **2016**, *1*, 888.
(38) Butler, K. T.; Dringoli, B. J.; Zhou, L.; Rao, P. M.; Walsh, A.; Titova, L. V. *J. Mater. Chem. A* **2016**, *4*, 18516.
(39) Ulbricht, R.; Hendry, E.; Shan, J.; Heinz, T. F.; Bonn, M. *Rev. Mod. Phys.* **2011**, *83*, 543.
(40) Wehrenfennig, C.; Eperon, G. E.; Johnston, M. B.; Snaith, H. J.; Herz, L. M. *Adv. Mater.* **2014**, *26*, 1584.
(41) Noel, N. K.; Stranks, S. D.; Abate, A.; Wehrenfennig, C.; Guarnera, S.; Haghighirad, A.-A.; Sadhanala, A.; Eperon, G. E.; Pathak, S. K.; Johnston, M. B.; Petrozza, A.; Herz, L. M.; Snaith, H. J. *Energy & Environ. Sci.* **2014**, *7*, 3061.
(42) Ponseca, C. S.; Savenije, T. J.; Abdellah, M.; Zheng, K.; Yartsev, A.; Pascher, T.; Harlang, T.; Chabera, P.; Pullerits, T.; Stepanov, A.; Wolf, J.-P.; Sundström, V. *J.Am. Chem. Soc.* **2014**, *136*, 5189.
(43) Rehman, W.; Milot, R. L.; Eperon, G. E.; Wehrenfennig, C.; Boland, J. L.; Snaith, H. J.; Johnston, M. B.; Herz, L. M. *Adv. Mater.* **2015**, *27*, 7938.
(44) La-o-vorakiat, C.; Salim, T.; Kadro, J.; Khuc, M.-T.; Haselsberger, R.; Cheng, L.; Xia, H.; Gurzadyan, G. G.; Su, H.; Lam, Y. M.; Marcus, R. A.; Michel-Beyerle, M.-E.; Chia, E. E. M. *Nat. Commun.* **2015**, *6*, 7903.
(45) Herz, L. M. *ACS Energy Lett.* **2017**, *2*, 1539.
(46) Piatkowski, P.; Cohen, B.; Ponseca, C. S.; Salado, M.; Kazim, S.; Ahmad, S.; Sundström, V.; Douhal, A. *J. Phys. Chem. Lett.* **2016**, *7*, 204.
(47) Nienhuys, H.-K.; Sundström, V. *Phys. Rev. B* **2005**, *71*, 235110.
(48) Beard, M. C.; Turner, G. M.; Schmuttenmaer, C. A. *Nano Lett.* **2002**, *2*, 983.
(49) Nienhuys, H.-K.; Sundström, V. *Appl. Phys. Lett.* **2005**, *87*, 012101.
(50) Smith, N. V. *Phys. Rev. B* **2001**, *64*, 155106.
(51) Miyata, K.; Meggiolaro, D.; Trinh, M. T.; Joshi, P. P.; Mosconi, E.; Jones, S. C.; De Angelis, F.; Zhu, X. Y. *Sci. Adv.* **2017**, *3*.
(52) Fröhlich, H. *Adv. Phys.* **1954**, *3*, 325.
(53) Bonn, M.; Miyata, K.; Hendry, E.; Zhu, X. Y. *ACS Energy Lett.* **2017**, *2*, 2555.
(54) Miyata, K.; Atallah, T. L.; Zhu, X. Y. *Sci. Adv.* **2017**, *3*.
(55) Bertolotti, F.; Protesescu, L.; Kovalenko, M. V.; Yakunin, S.; Cervellino, A.; Billinge, S. J. L.; Terban, M. W.; Pedersen, J. S.; Masciocchi, N.; Guagliardi, A. *ACS Nano* **2017**, *11*, 3819.
(56) Park, M.; Neukirch, A. J.; Reyes-Lillo, S. E.; Lai, M.; Ellis, S. R.; Dietze, D.; Neaton, J. B.; Yang, P.; Tretiak, S.; Mathies, R. A. *Nat. Commun.* **2018**, *9*, 2525.
(57) Sendner, M.; Nayak, P. K.; Egger, D. A.; Beck, S.; Müller, C.; Epding, B.; Kowalsky, W.; Kronik, L.; Snaith, H. J.; Pucci, A. *Mater. Horiz.* **2016**, *3*, 613.

(58) Adachi, S. *J. Appl. Phys.* **1985**, *58*, R1.
(59) Stoumpos, C. C.; Malliakas, C. D.; Peters, J. A.; Liu, Z.; Sebastian, M.; Im, J.; Chasapis, T. C.; Wibowo, A. C.; Chung, D. Y.; Freeman, A. J.; Wessels, B. W.; Kanatzidis, M. G. *Cryst. Growth Des.* **2013**, *13*, 2722.
(60) Shi, D.; Adinolfi, V.; Comin, R.; Yuan, M.; Alarousu, E.; Buin, A.; Chen, Y.; Hoogland, S.; Rothenberger, A.; Katsiev, K.; Losovyj, Y.; Zhang, X.; Dowben, P. A.; Mohammed, O. F.; Sargent, E. H.; Bakr, O. M. *Science* **2015**, *347*, 519.
(61) Brenner, T. M.; Egger, D. A.; Kronik, L.; Hodes, G.; Cahen, D. *Nat. Rev. Mater.* **2016**, *1*, 15007.
(62) Lakowicz, J. R. *Principles of Fluorescence Spectroscopy*; 3 ed.; Springer US, 2006.
(63) Saliba, M.; Matsui, T.; Domanski, K.; Seo, J.-Y.; Ummadisingu, A.; Zakeeruddin, S. M.; Correa-Baena, J.-P.; Tress, W. R.; Abate, A.; Hagfeldt, A.; Grätzel, M. *Science* **2016**, *354*, 206.

Chapter 5

Ultrafast Carrier Dynamics in Quasi-Two-Dimensional $CsPbBr_3$ Nanoplatelets

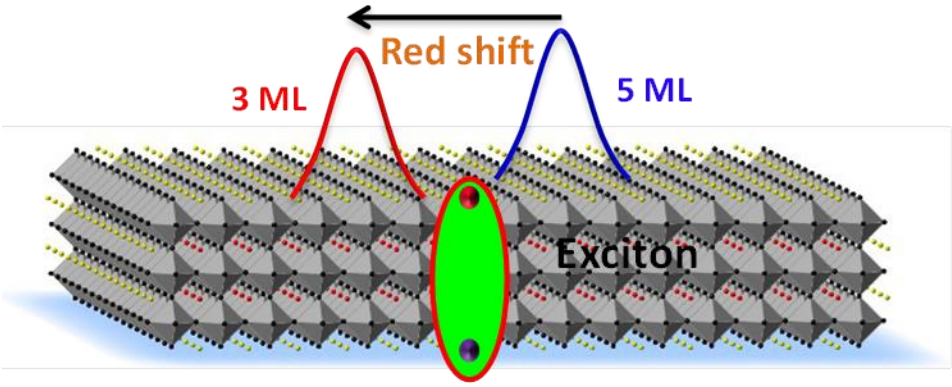

5.1. All-Inorganic perovskite nanoplatelets:

Quasi-two-dimensional (2D) semiconducting perovskite nanoplatelets (NPLs) have been emerging as a new class of functional, optoelectronic materials.[1-9] The motivation behind their exploration has come from their 3D counterparts, which are defect tolerant in nature, as evidenced by high (>80 %) photoluminescence quantum yields, reduced fluorescence blinking, and low threshold (~5 μJ/cm^2) fluences for lasing.[10-16] It is expected that the density of states at band edges in low dimensional materials increases compared to the bulk counterparts.[17] Hence one would expect to achieve population inversion and high optical gain at low threshold fluences, which strongly influences the efficiency of lasing. In this direction, researchers have already demonstrated lasing and light emitting diodes (LEDs) from these low dimensional materials.[6,18-20] Achieving quantum confinement, which occurs when the size of the NC is less than the exciton Bohr radius, in semiconducting NCs is challenging. When the size of the NC decreases the surface to volume ratio increases, the optical properties are mainly governed by the surface, which in turn determines the efficiency of optoelectronic devices. Synthesizing and achieving quantum-confined, highly PL emissive NPLs is relatively easy compared to 3D NCs. One could achieve confinement by controlling the size in only one dimension irrespective of sizes of other two dimensions.[3,4]

Recently, it was shown that excitonic dynamics are same in quantum confined NPLs, irrespective of their thickness, and in non-quantum confined samples such as cube-shaped NCs and polycrystalline film.[5] However, it is counter-intuitive to the trend observed in quantum dots, where, the probability of overlap between the electron and hole wave functions increases as the size decreases. This, in turn, reduces the lifetime and increases the recombination rate of photogenerated charge carriers. Further, studies related to recombination mechanisms and transport properties such as mobility and diffusion length which determine the efficiency of optoelectronic and photovoltaic devices, are at a rudimentary stage in this quasi 2D NPLs.[21-23] Recombination mechanisms and transport properties are highly sensitive to surface defects, also experience additional surface defects that arise due to lattice strain present in the low dimensional materials.[24] Time-resolved terahertz spectroscopy (TRTS), which uses non-contact low energy THz ac probe, has been successful over the last decade, in elucidating the recombination dynamics in picosecond resolution unlike time-resolved photoluminescence (TRPL), which probes dynamics in nanosecond range.[25-30] Further, probing phonon modes and their energy dependence on the number of monolayers in the quantum confinement regime is least explored in these quasi 2D NPLs. Probing phonons (lattice vibrations) is of paramount importance since the electron-phonon coupling limits the charge carrier mobility as well as broadens the PL emission.[31-34]

In this study, we employed time-domain (THz-TDS) and time-resolved terahertz spectroscopy (TRTS) along with time-resolved photoluminescence spectroscopy (TRPL) to examine the effect of confinement on phonon resonance, photo-induced carrier dynamics, and transport properties. THz absorption spectrum shows that as the confinement increases phonon frequency is redshifted due to the expansion of the lattice, evident from powder X-ray diffraction. Our study clearly shows that dynamics are fast due to excitons being the dominant excited species and are strongly dependent on the extent of confinement. Furthermore, strong confinement in NPLs curtails mobilities and diffusion lengths.

5.2 Synthesis and characterization of $CsPbBr_3$ nanoplatelets (3 and 5 monolayers):

Orthorhombic/cubic $CsPbBr_3$ nanoplatelets were synthesized and characterized by Wasim Mir and Jagadeeswara Rao from Dr. Angshuman Nag's group at IISER, Pune.

5.2.1 Synthesis of $CsPbBr_3$ nanoplatelets (NPLs):

The NPLs (both 5 monolayers (ML) and 3 monolayers) were synthesized by following the method developed by Manna and co-workers.[5] The reaction precursors and solvents used in the synthesis are four times higher than the earlier report to scale up the total yield of the NPLs. A mixture (mixture-1) of 5 mL 1-octadecene (ODE), 0.5 mL oleic acid (OA) and 0.5 mL oleylamine (OLA) were taken in a 50 mL centrifuge tube and kept at room temperature, under ambient conditions. The cesium oleate precursor was prepared by dissolving 350 mg of Cs_2CO_3 in 20 mL of ODE and 1.25 mL of OA at 150 ^oC. A portion (0.4 mL) of the above Cs-oleate precursor was heated to 100 ^oC and added to the mixture-1 in the 50 mL centrifuge tube under vigorous stirring. To this solution, 0.8 mL of $PbBr_2$ precursor solution (prepared by dissolving 735 mg of $PbBr_2$ in 5 mL dimethylformamide (DMF)) was injected. The reaction was quenched after 10 seconds by injecting 20 mL of acetone. The reaction mixture was centrifuged at 6000 rpm. The

NPLs thus obtained were dispersed in hexane and purified by adding methyl acetate as anti-solvent (twice the volume of hexane used). This mixture was centrifuged again at 6000 rpm. Finally, the NPLs (5-ML) were redispersed in hexane for further characterization.

Minor modifications were made in the synthesis of 3-ML NPLs. In this case, 40 µL of HBr was added to $PbBr_2$ precursor solution to control the thickness. The remaining protocol was the same as described above for 5-MLs. As synthesized NPLs were spin-cast on high-density polyethylene (HDPE) substrate for photoluminescence and THz experiments.

5.2.2 Characterization:

The **UV-visible absorption** spectrum was recorded by using a Perkin Elmer, Lambda-45 UV-Vis spectrometer. Steady-state and time-resolved photoluminescence (PL) of NCs were measured by FLS 980 (Edinburgh Instruments).

Powder X-ray diffraction (XRD) data were recorded by a Bruker D8 Advance X-ray diffractometer using Cu Kα radiation (1.54 Å).

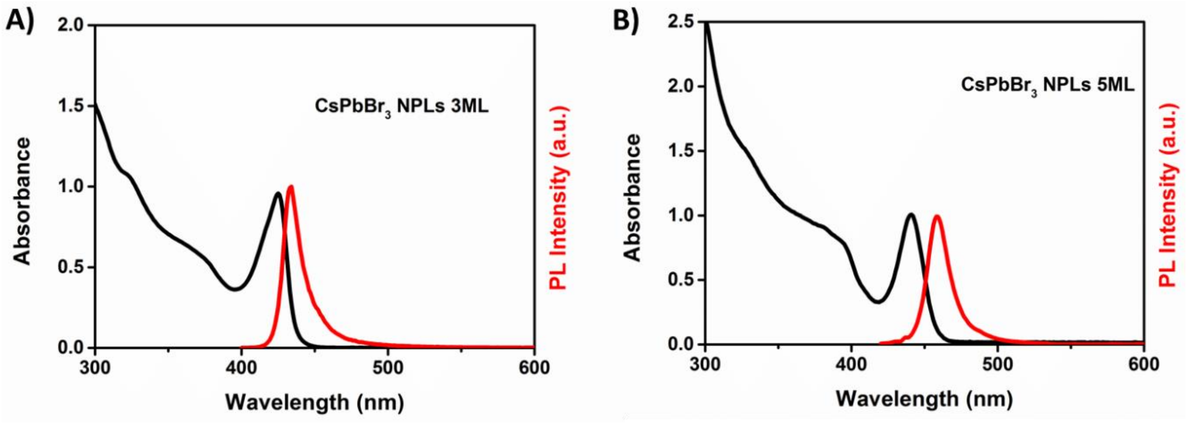

Figure 5.1. UV-vis absorption (black line) and photoluminescence (red line) spectra of A) 3 monolayer B) 5 monolayer nanoplatelets dispersed in hexane.

Transmission electron microscopy (TEM) images were recorded using a JEOL JEM 2100 F field emission transmission electron microscope at 200 kV. The sample preparation for TEM was done by putting a drop of the colloidal solution of NPLs in hexane on the carbon-coated copper grids.

Figure 5.1 shows the absorption and emission spectra of as-synthesized NPLs. The colloidal dispersion of 3-ML and 5-ML NPLs in hexane exhibit first excitonic absorption peaks at 425 and 440 nm, respectively. The PL emission maxima are observed at 434 and 459 nm for the 3-ML and 5-ML platelets, respectively. The clear blue shift in absorption/PL peaks from 5-ML to 3-ML indicates strong confinement of charge carriers. These NPLs crystallize in the orthorhombic/cubic crystal structure, confirmed from XRD, shown in Figure 5.2. The relatively broader peaks in the observed XRD pattern for the 3-ML platelets indicate less number of atomic planes compared with 5-ML platelets. The sample morphology and thicknesses were confirmed from both TEM and AFM, given in Figure 5.3. The thickness of 3-ML is unclear from TEM image. Hence, we determined the thickness of 3-ML platelets from the height profile of their AFM images. The measured thicknesses for 3-ML and 5-ML are ~2.0 nm and ~3.5 nm, respectively, thus confirming as many layers present and are consistent with previous literature.[5]

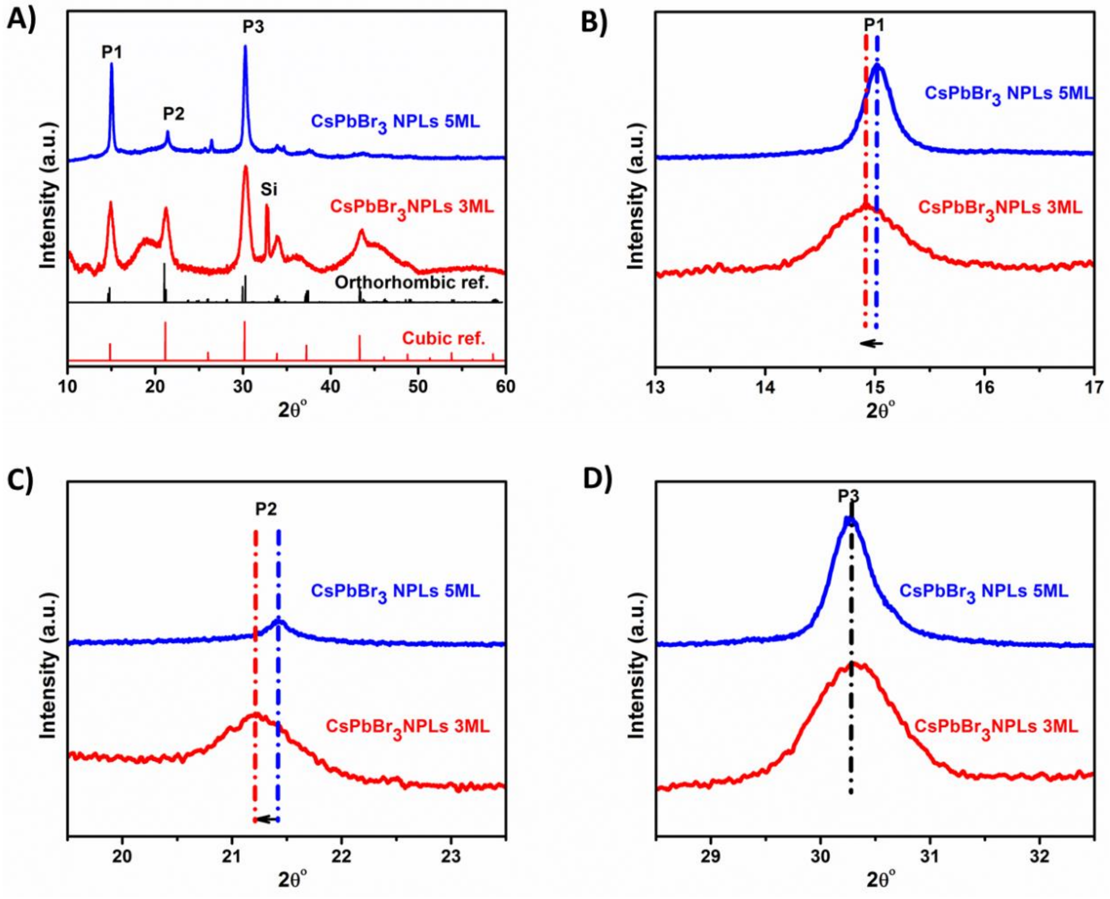

Figure 5.2. A) Powder X-ray diffraction patterns of 3-ML and 5-ML platelets of CsPbBr$_3$ along with orthorhombic/cubic reference crystal structures. Three most intense peaks labeled as P1, P2, and P3 were used to calculate the lattice parameters. B) and C) Expanded view of peaks P1 and P2 showing a decrease in 2θ values going from 5-ML to 3-ML (black arrow). D) An expanded view of peak P3 showing no change in 2θ position (short dash dot vertical black line).

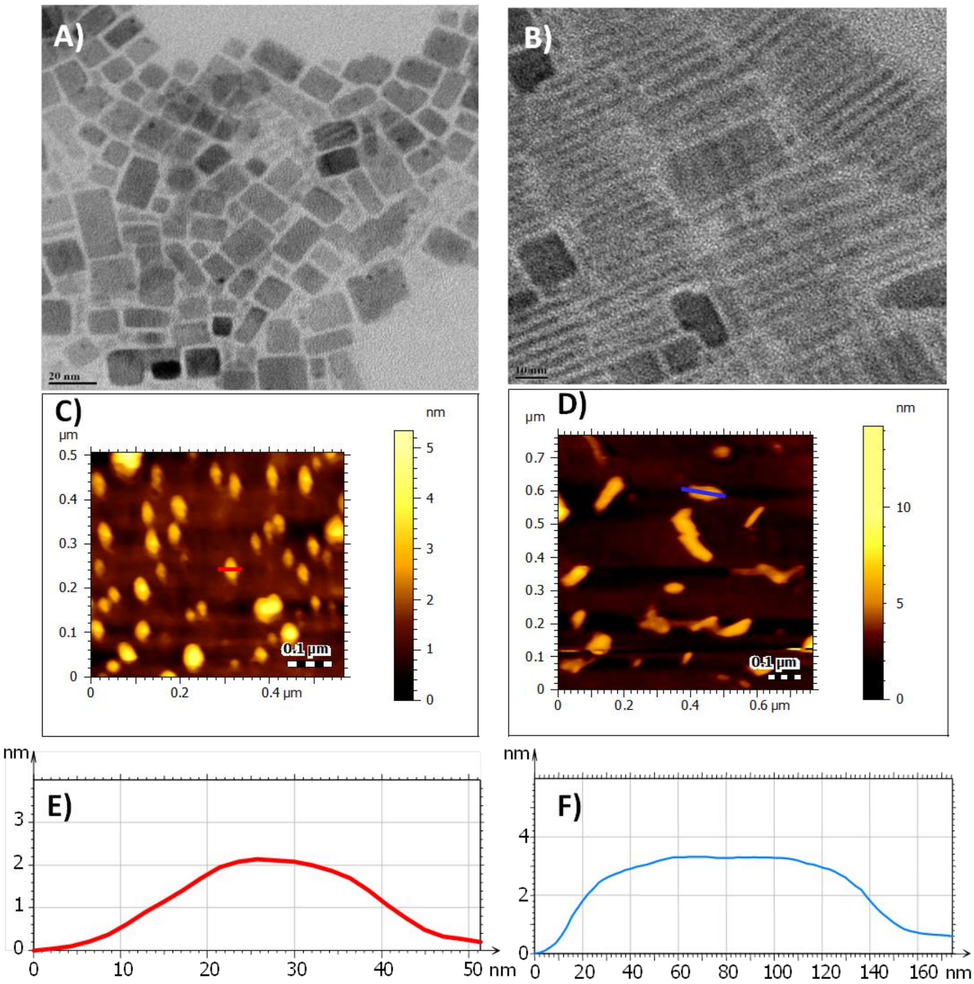

Figure 5.3: TEM images and AFM images of 3-ML (A and C) and 5-ML (B and D) of CsPbBr$_3$ nanoplatelets. E and F are the height profiles corresponding to the lines drawn in C and D.

5.3. Results and Discussion:

5.3.1 Steady-state and time-resolved photoluminescence of NPLs:

The spin-cast films on HDPE were used in both TRPL and TRTS studies. Initially, the absorption and PL spectra were recorded to see if there is any spectral change relative to the native colloidal NPLs dispersed in hexane. Figure 5.4.A and 5.4.B show the UV-vis absorption and PL spectra of 3-ML NPLs film, respectively. The absorption spectrum shows the first excitonic peak at ~425 nm, similar to NPLs solution. However, the excitonic peak is slightly broader in the film. Also, the absorption spectrum has a very weak feature at a higher wavelength (~510 nm). This probably indicates several NPLs are stacked together to make a bulk-like state in the film. The same can also be observed in the PL spectrum. The PL spectrum shows emission peak at 434 nm corresponding to 3-ML absorption peak, whereas the peak at 520 nm corresponds to emission from stacked/bulk-like NPLs having absorption feature at 510 nm. Further, as the thickness of the film increases, the intensity of the 520 nm emission peak increases, as shown in Figure 5.4.B. This clearly indicates stacking of the NPLs. Previous reports also observed similar stacked/bulk-like emission peak when NPLs solution was drop-cast on a soda-lime glass substrate.[21,35] From $CsPbBr_3$ NCs solution, it was known that the bonding of the organic capping ligand to the NC surface is highly dynamic in nature and easily detached during purification process.[36] Similar effect is expected in case of $CsPbBr_3$ NPLs. When the NPLs solution is drop casted on the substrate, the organic capping ligands may easily be displaced allowing NPLs to come closer to each other.

The excited state carrier lifetime from a particular electronic state can be obtained in TRPL by probing the temporal evolution of a particular emission wavelength corresponding to the energy of a particular electronic state. Figure 5.4.C represents the PL traces for 434 nm and 520 nm, corresponding to the 3-ML NPLs and the stacked NPLs, respectively. A faster kinetics at 434 nm indicates the emission is mostly from the quantum confined 3-ML NPLs. The 3-ML NPLs are strongly quantum confined as their transverse dimension (thickness/width) (~2 nm) is much smaller than the exciton Bohr diameter (~7 nm). This facilitates a strong overlap between electron and hole wave functions, resulting in a decrease in the lifetime and an increase in the recombination rate of photogenerated charge carriers. In the case of stacked bulk-like NPLs, the carrier wave functions are delocalized across the NPLs, which reduce the overlap between them yielding an increased lifetime. However, it was recently reported that the exciton dynamics are independent of the extent of confinement in NPLs and even they are the same when compared with non-quantum confined systems such as cubes and polycrystalline film. Hence, it is imperative to synthesize other NPLs which are thinner or thicker than 3 ML to get better insights into the dynamics. Herein we synthesized 5-ML NPLs (d=3.5nm), which are relatively easy to synthesize and more stable, to compare their dynamics with 3-ML NPLs. Figure 5.4.D compares the PL dynamics of the 3-ML and 5-ML NPLs. The PL traces are fitted with multi-exponential function and corresponding fitting parameters are tabulated in Table 1 along with the parameters for stacked NPLs having an emission peak at 520 nm.

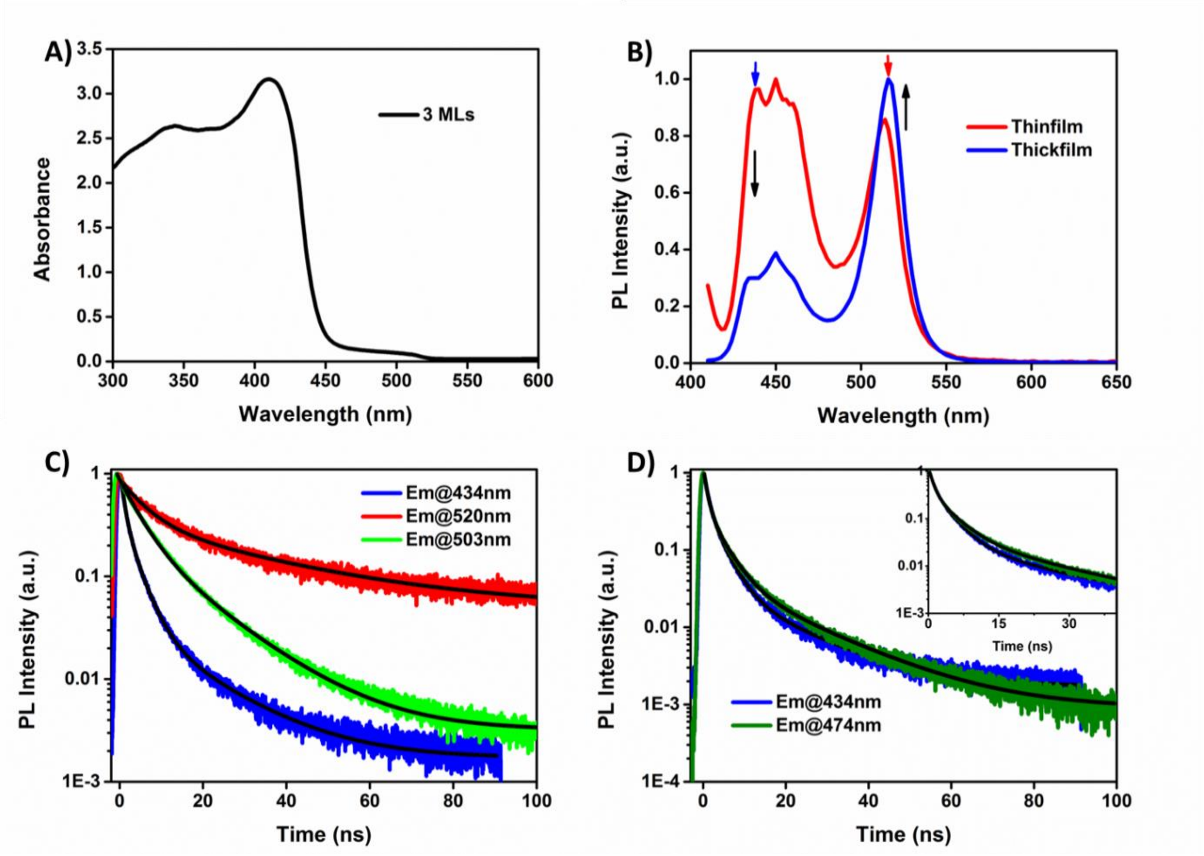

Figure 5.4: Absorption (A) and steady-state PL (B) spectra of 3-ML NPLs. C) TRPL of 3-ML NPLs. The Blue trace is obtained by keeping the emission wavelength at 434 nm, comes purely from quantum-confined 3-ML NPLs whereas the red trace is from stacked NPLs having emission at 520 nm. The green trace represents the kinetics obtained from the film, after completion of THz experiments, has emission at 503 nm. The black solid lines represent the multi-exponential function fit to the data. D) Comparison of PL dynamics obtained from 3-ML and 5-ML having emission wavelengths at 434 and 474 nm, respectively. The excitation wavelength is at 405 nm.

Table 5.1: Fitting parameters obtained for 3-ML and 5-ML NPLs along with stacked NPLs whose emission is at 520 nm.

$\lambda_{emission}$ (nm)	τ_1 (A_1) (ns)	τ_2(A_2) (ns)	τ_3(A_3) (ns)	<τ> (ns)
434 (3ML)	0.92 (0.61)	3.3 (0.35)	15.1 (0.031)	5.20
	0.006 (0.004)	0.032 (0.004)	0.298 (0.001)	(0.21)
474 (5ML)	0.89 (0.57)	3.84 (0.36)	17 (0.058)	7.83
	0.003 (0.001)	0.015 (0.001)	0.00 (0.00)	(0.01)
490 (>5ML)	0.99 (0.53)	5.11 (0.394)	20 (0.078)	10.25

	0.004 (0.001)	0.013 (0.001)	0.00 (0.00)	(0.01)
520 (stacked)	5.7 (0.65)	33.3 (0.345)	---	26.60
	0.046 (0.002)	0.212 (0.002)		(0.18)

Average lifetime: $< \tau > = \sum f_i \tau_i$; where $f_i = \frac{a_i \tau_i}{\sum a_i \tau_i}$ is the contribution of the ith recombination process to the overall recombination dynamics.

It is clear that the dynamics in 5-ML (λ_{em}=474 nm) is relatively slow compared to that in 3-ML (λ_{em}=434 nm). The same is reflected in the average lifetime which is higher for 5-ML (7.8 ns) compared to 3-ML (5.2 ns) NPLs. We attribute relatively faster recombination kinetics in case of 3-ML NPLs to a better overlap between the electron and hole wave functions caused by the stronger quantum confinement in 3-ML NPLs. Therefore, one should be more careful to rule out the effect of confinement on exciton dynamics.

Figure 5.5.A shows UV-vis absorption and PL spectra of 5-ML NPLs film. The first excitonic absorption and emission peaks are redshifted compared to those in the colloidal solution. The absorption spectrum has an extra feature at 473 nm, most probably originating from the higher order NPLs (greater than 5-MLs).[37] The corresponding PL emission is at 490 nm. Again, while comparing the PL dynamics at both wavelengths (474 nm and 490 nm), shown in Figure 5.5.B, it is evident that the dynamics are indeed dependent on the layer thickness i.e. quantum confinement effect (7.8 ns vs. 10.3 ns).

To check the structural changes during TRTS, we have recorded PL after completion of TRTS. Steady-state PL recorded before and after the exposure of visible light (pump light used in TRTS; 400, 480 and 510 nm) for 3-ML and 5-ML films are given in figure 5.5.C and 5.5.D, respectively. The PL has changed drastically in the case of 3-ML sample, as shown in Figure 5.5.C. The PL spectrum neither has the strong quantum-confined 3-ML NPLs emission feature (434 nm) nor the stacked/bulk-like NPLs emission feature (520 nm). Instead, the emission peak maximum after TRTS experiments appears at 503 nm. One should note that this emission peak is very close to that observed in CsPbBr$_3$ nano-cubes having an edge-length of 9 nm.[15] This can be understood from the concept of photon driven transformation (PDT). Exposure of prolonged laser irradiation induces desorption of the ligands attached to the surface of NPLs and converts few layer NPLs to bulk-like analog.[37] PDT process is easily feasible in these NPLs given the dynamic nature of the ligands and easy-migrating nature of the halide ions.[36,38] Further, the dynamics at this emission wavelength (503 nm), shown in Figure 5.4.C, are faster compared to bulk-like NPLs. This indicates that these NPLs are still under confinement regime. Hence, the origin can be either due to stacking/coalescence of 3-ML NPLs or bulk-like phase disintegrating into smaller higher order NPLs, as explained by PDT mechanism. On the contrary, steady-state PL of 5-ML NPLs, shown in Figure 5.5.D, is only slightly red-

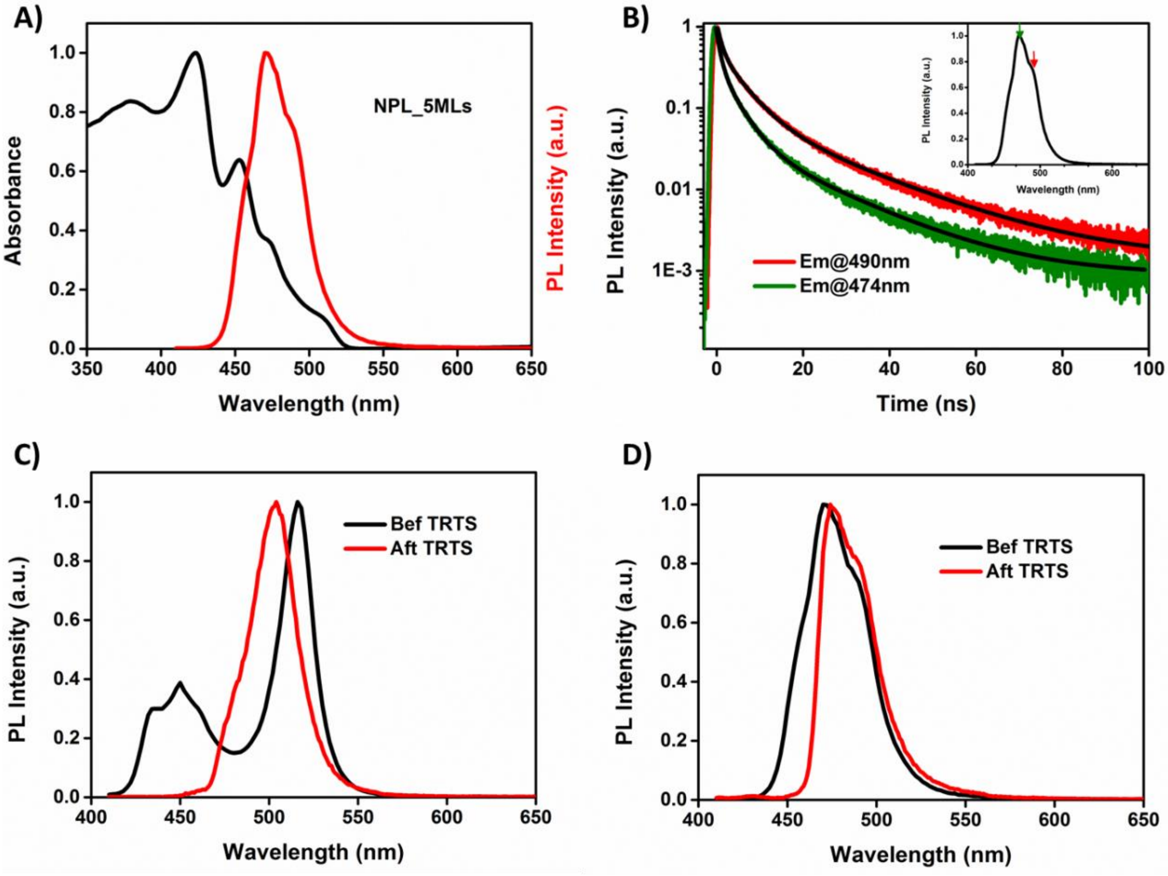

Figure 5.5. A) UV-vis absorption and PL emission spectra of 5-ML nanoplatelets. B) TRPL of 5-ML and higher order NPLs which have emission wavelengths at 474 and 490 nm, respectively. C) and D) compare the steady-state PL of 3-ML and 5-ML before and after time-resolved THz experiments, respectively. 3-ML PL has changed drastically whereas 5-ML PL is slightly red-shifted with a decrease in FWHM.

shifted after TRTS experiment, indicating better stability of these NPLs to the exposure of pump light (visible). FWHM is less, mainly the high energy (455 nm) shoulder is missing.

It is interesting to note that, below 520 nm emission wavelength, a slight change in emission wavelength, such as the case in the 5-ML film (474 nm corresponds to 5-ML vs. 490 nm corresponds to higher order (>5 ML) ML NPLs), the dynamics are clearly distinguished. Further, 474 nm dynamics are faster than 490 nm ones. Comparing 3-ML and 5-ML NPLs, one would expect even faster dynamics for 3-ML to that of 5-ML due to strong quantum confinement effect present in the former case. However, there is a very minute change in the rate of decay between both, that might have prompted previous reports to propose that PL dynamics are independent of the thickness of the NPLs.

This inspired us to pose a question that if recombination occurs on the ultrafast time scale, can TRPL (time resolution in nanoseconds) capture the dynamics on ultrafast time scale? To address this problem, one may use the femtosecond time-resolved photoluminescence (up-conversion) technique; but, it is limited to probe carrier dynamics only. Here, we employ TRTS, which simultaneously measures carrier dynamics and transport properties on the ultrafast timescale. Further, TDS was employed to unravel phonon modes.

5.3.2 THz time-domain spectroscopy:

Time-domain THz spectroscopy was performed on NPLs films which are spin-cast on HDPE substrate. The absorbance and dielectric constant as a function of THz frequency were obtained from time-domain THz electric fields passing through both HDPE (reference) and NPLs film (sample). Details of the analysis procedure are given in chapter 2. The THz absorption spectrum for 3-ML NPLs, shown in Figure 5.6.A, contains absorption features at 2.45 and 4.2 THz. These absorption features can easily be assigned to anisotropic lattice vibrations of the NPLs; vertical and horizontal directions, respectively (see the schematic at the inset of Figure 5.6.A). We assign the phonon feature at ~4.2 THz, which is independent of NPL thickness, to in-plane atomic vibrations. Since these lateral dimensions are not limited by the thickness of the NPLs, phonons are not confined in this direction. Hence, the phonon frequencies are not affected by the change in thickness of the NPLs. The most intense phonon feature (2.45

THz) which is associated with confinement direction changes with thickness. Most probably this is associated with vertical atomic vibrations. From 3-ML to 5-ML the phonon feature is blue shifted. In other words, as the confinement increases the phonon feature is redshifted. Figure 5.6.B shows the THz-TDS absorption spectra of 3-ML and 5-ML along with nanocubes (~11 nm) in colloidal form and film for comparison. Often, the phonon frequency is mainly affected by either lattice contraction or expansion.[39-41] Generally, expansion increases the interatomic distances and reduces the force constant, which in turn makes atoms vibrate at low energy (frequency). On the other hand, lattice contraction reduces the interatomic distances and increases the force constant which in turn increases the vibrational frequencies. Our PXRD data, see Figure 5.2., clearly shows that the 2θ value decreases going from 5-ML to 3-ML. Since 2θ is inversely proportional to interatomic distance, reduction in 2θ indicates the distance between atoms increases as well as it leads to lattice expansion. Further, we have calculated lattice parameters from the most intense peaks observed in PXRD, labeled as P1, P2, and P3, and are given in Table 2. It is difficult to distinguish the cubic lattice from the orthorhombic lattice; so we have calculated lattice parameters for both and compared with bulk single crystal.

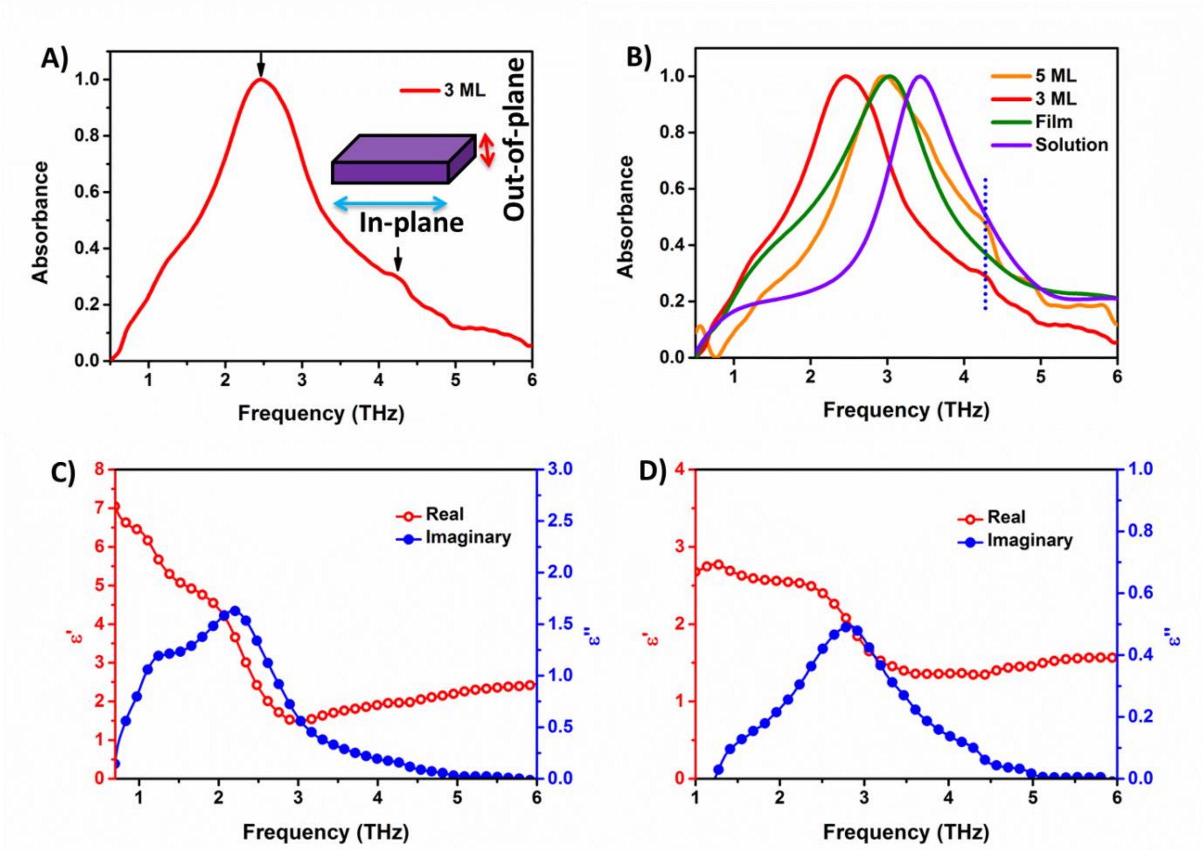

Figure 5.6. A) Normalized THz absorption spectrum of 3-ML CsPbBr$_3$ NPLs. B) Comparison of THz absorption spectra of 3-ML (Red) and 5-ML (Orange) along with cubic NCs (~11 nm) in colloidal (Olive) and drop-cast film (Violet) form, taken from our previous chapters. The dotted vertical line drawn at 4.2 THz indicates that the phonon feature of the NPL is independent of thickness. C) and D) are THz frequency dependent real (red open circles) and imaginary (blue solid circles) dielectric functions of 3-ML and 5-ML NPLs respectively.

Table 5.2. Lattice parameters obtained from powder X-ray diffraction pattern for both cubic and orthorhombic unit cell.

Crystal lattice	Lattice Parameters		
	a (Å)	B (Å)	C (Å)
Cubic (bulk)	5.83	--	--
Cubic (5-ML)	5.90 (P1) 5.86 (P2) 5.90 (P3)	--	--

Cubic (3-ML)	5.93 (P1) 5.91 (P2) 5.89 (P3)	--	--
Orthorhombic (bulk)	8.21	8.26	11.76
Orthorhombic (5-ML)	8.18	8.29	11.80
Orthorhombic (3-ML)	8.31	8.36	11.86

It is clearly evident from the peaks P1 and P2 that the lattice parameter increases while going from 5-ML to 3-ML, which indicates a clear expansion of lattice, although the P3 peak lattice parameter remains constant. Even if we consider an orthorhombic lattice, we can see a similar increase in lattice parameters on reducing the thickness of the NPLs from 5-ML to 3-ML. As discussed above, the lattice expansion leads to a redshift of the phonon modes. A Similar expansion was also observed in the earlier report where Akkerman et al. have given a possible explanation.[5] Cs$^+$ ions present on the top and bottom facets of the NPLs are replaced by protonated oleylamine ligands which slightly expand the lattice. This was further confirmed by the substantial deficiency of Cs from elemental analysis indicating the replacement by oleylammonium cations.[5] Therefore, we conclude that lattice expansion on reducing the thickness of the NPLs (5-ML to 3-ML) leads to the redshift of the phonon modes observed in the THz absorption spectrum. However, this is in contrary to the observations in CdSe Raman spectrum where redshift was attributed to lattice contraction.

Further, we have calculated the dielectric functions for NPLs, as drop casted film form, and are given in Figure 5.6.C and 5.6.D. The reduced dielectric constant (in THz frequency) compared to that in NCs can be one of the reason for high exciton binding energies observed in these NPLs.[12,23] From Coulomb's law one can understand that coulomb attraction (exciton binding energy) between electron-hole pair depends inversely on the square of the distance between them and is also inversely related to the dielectric constant. The high exciton binding energy indicates that either the distance or dielectric constant should decrease. Compared with the nanocubes (~11 nm edge length, Chapter 3 and 4), the size of the NPLs is certainly reduced below 3.5 nm in the confinement direction. Further, as shown in Figure 5.6.C and 5.6.D, the dielectric function has also been reduced compared to that in cubes, whose dielectric function varies between 9 to 5 with THz frequency.[12] Hence, the increased exciton binding energy can be a result of both effects. The change in dielectric function can be due to the dielectric environment present in the NPLs.[3,35,42] In the case of the 3-ML NPLs, one would expect a lower dielectric constant compared to that in 5-ML because the top and bottom facets of the 3-ML NPLs are covered mostly by organic capping ligands with a dielectric constant of ~ 2.5. However, due to the lower stability of the 3-ML NPLs, coalescence of monolayers takes place readily increasing the effective thickness. Hence, the dielectric environment in 3-ML NPLs is mainly affected by the inorganic layer (Octahedron layer) having a dielectric constant of >6. This leads to a higher effective dielectric function in 3-ML NPLs as observed here. Whereas in the case of 5-ML, no such coalescence of NPLs is observed. Hence, the dielectric environment is determined mainly by the capping ligands resulting in a low dielectric function in 5-ML NPLs.

5.3.3 Recombination dynamics: Optical pump-THz probe spectroscopy:

Charge transport properties, such as carrier mobility and diffusion length are governed by charge carrier recombination dynamics, which in turn determines the efficiency of optoelectronic and photovoltaic applications. Therefore, studying them in detail is of atmost importance. Given the bandgap of the NPLs is at 425 nm, and considering that the film contains stacked platelets along with 3-ML confined platelets, initial excitation of the film with 400 nm optical pump pulse primarily excites 3-ML platelets.[4] However, we cannot completely ignore the contribution from stacked/bulk-like NPLs with absorption and emission at 510 and 520 nm, respectively. Figure 5.7.A shows the THz transients at 400 nm pump as a function of pump-probe delay. The photoinduced change in THz transmission in TRTS is proportional to the THz conductivity, which is the product of carrier density and mobility. The initial fast decay indicates fast recombination of charge carriers. These charge carriers can be either excitons or free carriers. In confined systems, it is expected that excitons are the dominant species. Herein, we assume that the dominant carriers are excitons. The maximum carrier population (>85 %) decays within 130 ps and the decay profiles become flat thereafter. This is reflected in the lifetime parameters which are obtained by fitting the normalized THz transients to a multi-exponential function convoluted with a Gaussian function[43] of the form:

$$y = G(t\text{-}t_0) \otimes \sum_i a_i \exp\left[-\frac{t\text{-}t_0}{\tau_i}\right] \qquad (5.1)$$

where $G(t\text{-}t_0)$ is a Gaussian function centered at t_0 with FWHM of ~300 fs which represents the instrument response time of our OPTP experiment, and a_i is the coefficient of the i^{th} exponential decay channel with a time constant τ_i. As the temporal window in our OPTP experiment is up to 1.6 ns, the long decay times cannot be determined accurately from our measurement. Hence, we use the long decay time constants obtained from the time-resolved PL experiments as the time constant for the slowest recombination process. Since long decay tails at all fluences are parallel, we fix this to the constant value, obtained from TRPL, and derive other time constants at all fluences. We note that variation in long time decay constant can slightly affect the other time constants. The THz transients fitted to the multi-exponential function are shown in Figure 5.7.B and the corresponding fit parameters are given in Table 3. Two faster processes with time constants of 16 ps and ~ 160 ps contribute mostly (greater than 85 percent) to the overall carrier recombination dynamics. Although the dynamics are not strongly dependent on pump fluence, the fastest component contribution increases along with a concomitant decrease in the slow component contribution with increasing fluence. At low pump fluences (low carrier density) carriers fill up the trap-states first. These all-inorganic perovskites are known to be defect tolerant – emission properties are not affected by trap states. However, in the blue region, they can form midgap states that can trap charge carriers. Therefore, we observe low photoluminescence quantum yield. Even strained lattice in these low dimensional materials also contribute to additional trap states.[24] However, at higher fluences, these trap states being already filled with carriers cannot trap further, so the contribution to the fast decay component increases gradually.

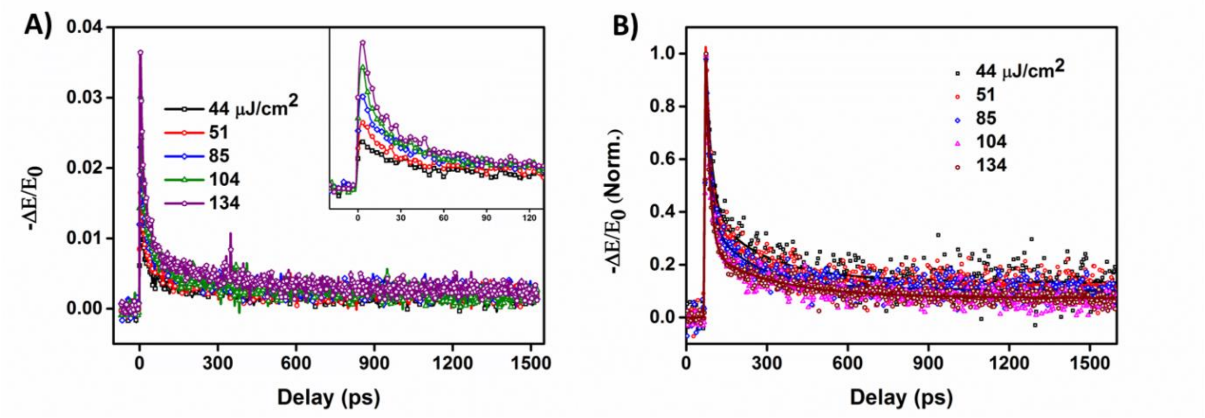

Figure 5.7. A) THz photoconductivity transients for 3-ML NPLs obtained with 400 nm pump light excitation at various fluences. The Inset shows that greater than 85 percent population decay within 130 ps. B) and their corresponding normalized transients fitted to tri-exponential function. The symbols are the experimental data points and the solid lines are the fit.

Table 5.3. Fitting parameters obtained when normalized THz transients were fitted to Gaussian convoluted multi-exponential function for 400 nm pump pulses.

Wavelength (nm)	**Fluence (μJ/cm²)**	**a_1**	**τ_1 (ps)**	**a_2**	**τ_2 (ps)**	**a_3**	**τ_3 (ps)**
400	44	0.61 (0.002)	20.5 (0.1)	0.28 (0.001)	192.2 (1.2)	0.15 (0.00)	15000
	51	0.65 (0.002)	16.0 (0.1)	0.28 (0.001)	157.5 (0.8)	0.13 (0.00)	15000
	85	0.67 (0.002)	16.6 (0.1)	0.26 (0.001)	164.1 (0.7)	0.11 (0.00)	15000
	104	0.75 (0.001)	16.1 (0.1)	0.20 (0.00)	199.6 (0.9)	0.08 (0.00)	15000
	134	0.79 (0.001)	16.5 (0.0)	0.17 (0.001)	241.5 (1.1)	0.08 (0.00)	15000

The steady-state PL of 3-ML NPLs film, as shown in Figure 5.4.B, contains emission peaks at 434 and 520 nm corresponding to 3-ML NPLs and stacking/bulk-like analog of NPLs, respectively. Photoexcitation with 480 and 510 nm primarily excites the stacked

NPLs, which are higher in order (>3 ML) but not completely bulk-like. The PL emission peak after TRTS is at 503 nm and kinetics are very fast at this emission wavelength, compared to 520 nm emission peak, see Figure 5.5.C and 5.4.C. However, excitation of confined 3-ML platelets can be completely ignored as the band gap of 3-ML NPLs is at 425 nm. Hence, the observed kinetics are mainly from higher order NPLs along with the contribution from the bulk-like components. THz transients obtained for 480 and 510 nm pump pulses are given in Figure 5.8. The normalized THz transients fit well to tri-exponential function. The fitting parameters are given in Table 4.

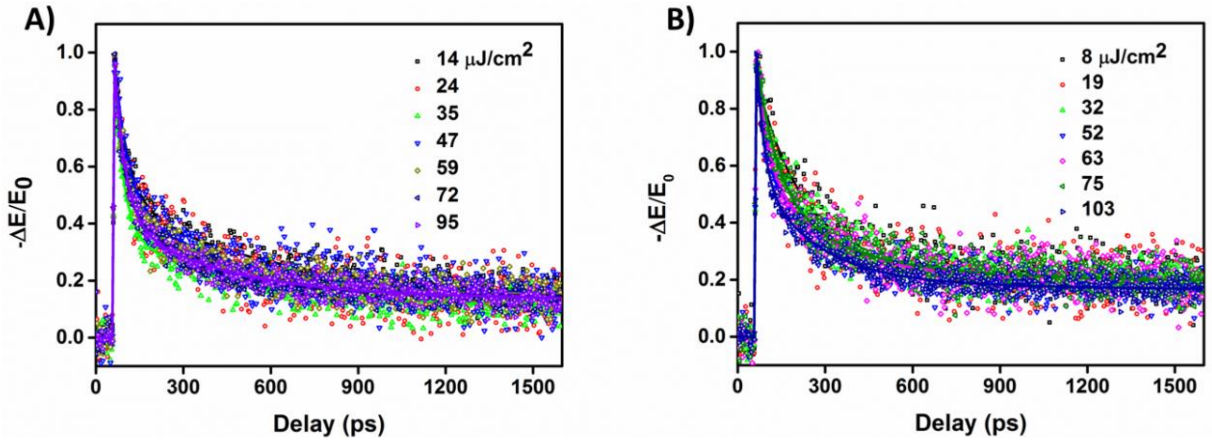

Figure 5.8. THz photoconductivity transients obtained for A) 480 nm pump and for B) 510 nm pump pulses at various excitation fluences. These normalized transients fit well to tri-exponential function.

Table 5.4. Fitting parameters obtained from the fits of the normalized THz transients to Gaussian convoluted multi-exponential function at 480 and 510 nm pump pulses, respectively.

Wavelength (nm)	Fluence (μJ/cm^2)	a$_1$	τ$_1$ (ps)	a$_2$	τ$_2$ (ps)	a$_3$	τ$_3$ (ps)
	14	0.47	30.0	0.38	363	0.18	14000
		(0.001)	(0.0)	(0.00)	(1.2)	(0.00)	
	24	0.49	27.2	0.38	324	0.15	14000
		(0.002)	(0.3)	(0.001)	(1.8)	(0.00)	
	35	0.56	31.0	0.26	338	0.13	14000
		(0.001)	(0.2)	(0.00)	(2.0)	(0.00)	

480	47	0.49 (0.002)	32.0 (0.0)	0.37 (0.001)	290 (1.3)	0.18 (0.00)	14000
	59	0.51 (0.001)	35.8 (0.2)	0.29 (0.001)	296 (1.7)	0.17 (0.00)	14000
	72	0.51 (0.001)	26.9 (0.2)	0.35 (0.001)	234 (0.9)	0.16 (0.00)	14000
	95	0.57 (0.001)	37.4 (0.2)	0.27 (0.00)	342 (1.8)	0.15 (0.00)	14000
510	8	0.36 (0.002)	40.0 (0.0)	0.44 (0.00)	280 (0.0)	0.22 (0.00)	14000
	19	0.32 (0.002)	37.0 (0.0)	0.42 (0.00)	240 (0.0)	0.21 (0.00)	14000
	32	0.32 (0.002)	36.6 (0.5)	0.45 (0.002)	225 (1.0)	0.22 (0.00)	14000
	52	0.35 (0.002)	32.8 (0.4)	0.42 (0.002)	199 (1.0)	0.21 (0.00)	14000
	63	0.38 (0.003)	32.5 (0.4)	0.42 (0.003)	205 (1.2)	0.22 (0.00)	14000
	75	0.33 (0.002)	30.0 (0.0)	0.50 (0.00)	204 (0.0)	0.22 (0.00)	14000
	103	0.47 (0.002)	26.2 (0.2)	0.38 (0.001)	205 (0.8)	0.19 (0.00)	14000

It is evident from the time constants that the fastest component (τ_1) timescale (~32 ps) doubled than the fastest component observed in the case of 400 nm pump, where it was 16 ps. It indicates when the platelets are stacked together, the probability of the electron and hole recombination reduces slightly since the wave functions are delocalized across the platelets. The second time constant (τ_2) also increases to 200 – 300 ps which also justifies the stacking nature of the NPLs. These results clearly indicate that the dynamics are very fast in the case of very strongly confined systems and as the confinement reduces the carrier lifetime increases. Further, most of the carrier population (>85 %) decays within a few hundred picoseconds (< 350 ps). TRTS can clearly distinguish the dynamics, occurring on ps timescale, in systems with a varied degree of confinement. On the other hand, TRPL data reported earlier cannot discriminate the dynamics which occur within few hundred ps since its time resolution is greater than 100 ps. This might have prompted the earlier researchers to conclude that the dynamics are independent of the degree of confinement present in the NPLs. This may be further clarified by femtosecond up-conversion study.

Further evidence of the dynamics being dependent on confinement can also be derived by probing 5-ML NPLs, which are also under confinement regime. These 5-ML NPLs are more stable compared to 3-ML and are free of the bulk-like component, see Figure 5.5.D. The THz transients obtained at 400 nm pump excitation for 5-ML are given in Figure 5. 9. A. Similar to 3-ML NPLs, the dynamics are very fast in 5-ML NPLs and greater than 85 % population decreases within a few hundred picoseconds. The fastest component (τ_1) is less than 10 ps, see the fitting parameters given in Table 5. However, dynamics are faster in case of 5-ML as compared to 3-ML. This is counter-intuitive. The carrier recombination dynamics is expected to be faster under stronger confinement. TRPL probes charge carriers from a particular electronic state by setting the emission wavelength. The film contains a distribution of different sizes of NPLs which exhibit different emission wavelengths. Dynamics from only specific sized NPLs can be probed by fixing the emission wavelength to that particular NPL's emission wavelength. However, in the case of TRTS, optical excitation with particular wavelength can excite distribution of NPLs (NPLs with various numbers of monolayers) and THz probe interacts with all charge carriers irrespective of the size of NPLs from which they are generated. Hence, THz probes the dynamics of the distribution of NPLs in the film. In the case of the 3-ML film, the observed dynamics have a contribution from both confined NPLs, stacked/bulk-like NPLs, which are higher in order (> 3 ML), and from the bulk form (PL peak at 520 nm). On the other hand, the 5-ML film does not contain any bulk component (absence of 520 nm emission peak in PL, see Figure 5.5.D). Hence, the observed dynamics are purely from confined NPLs and the dynamics are faster in case of 5-ML compared to that in 3-ML NPLs. The same can be justified by exciting 3-ML film with below bandgap pump light, where only the higher order stacked NPLs get excited. The dynamics observed is slow compared to that in strongly confined 3-ML and 5-ML NPLs, as shown in Figure 5.9.B.

The primary photo-excited species are excitons, as observed in the conductivity spectrum in Figure 5.9.C. The characteristic signature of excitons is a zero real conductivity and a negative but finite imaginary conductivity.[27,44] It is interesting to note that a similar THz transmission peak maxima (photoconductivity) were obtained at lower fluences with 480 and 510 nm pump compared with 400 nm pump, where higher pump fluences are required to get similar peak maxima. The discrepancy to get a similar change in THz transmission peak maxima at different pump wavelengths and at different fluences can be understood from the relation of polarizability of exciton with the size of the quantum dots (nanocrystals). In quantum dots, the polarizability increases sharply with quantum dot radius as $\sim R^4$.[44-46] It is known that in confined QD systems the energy gap between intra electron/hole states is few tens to 100 meV hence direct transitions with a THz (~4 meV) photon is not possible.[47] Hence, the observed THz response is due to the change in exciton polarizability on interaction with a THz photon. The polarizability of excitons is determined from the off-resonant transitions probabilities of electrons and holes comprising the exciton. In the case of $CsPbBr_3$ NPLs, the effective masses of electron and hole are similar;[5] both contribute equally to the exciton polarizability. Exciton response/polarizability primarily depends on two factors: the dielectric function and effective masses of the carriers. If the dielectric constant is high, there will be more screening of the electric field leading to less exciton response. If the effective mass of the carrier is high, the intraband transition energies are less; hence the exciton response is more. This is evident in the case of CdSe, InAs, and PbSe quantum dots. Since CdSe ($\varepsilon \approx 9.5$) and InAs ($\varepsilon \approx 12.4$) possess low dielectric constant values compared to PbSe ($\varepsilon \approx 215$), former quantum dots are more polarizable (excitons are more sensitive to THz) than the latter one.[45,46] Further, as the effective masses of holes are higher compared to electrons in CdSe and InAs quantum dots, holes contribute more to the exciton polarizabilities. Here, 400 nm pump primarily excites strongly quantum confined NPLs. The intra-band energy level spacing in pure quantum confined systems is more. So, the exciton response to off-resonant THz pulse is weak and hence higher pump fluences i.e. higher number of excitons are required to get similar peak maxima. However, 480 and 510 nm pumps excite stacked/bulk-like NPLs whose intra-band spacing is less. Hence, exciton response to THz is more, and a lower number of excitons (or low pump fluences) is enough to yield a similar THz peak. These results follow the formulations given for ground state (DC) polarizability as[45]

$$\alpha = \frac{|(\mathrm{e.r})|^2}{\Delta \mathrm{E}} \tag{5.2}$$

where (e. r) is the transition dipole moment for electronic transitions with energy level spacing ΔE, which is related to quantum dot radius (R) as $\Delta E \approx \frac{h^2}{mR^2}$; where h is the Planck's constant and *m* is the carrier mass.

Strong response to THz at lower fluences, slower recombination and high mobilities (see below) in stacked/bulk-like NPLs indicates that the excitons are formed across the NPLs, in line with the previous reports.[21] It is expected that polarizabilities in NPLs are high compared to above-mentioned quantum dots since the dielectric function is low ($\varepsilon < 7$) and effective masses are high ($m_e = m_h = 0.22$ and 0.21 for 3 and 5-MLs, respectively).[5]

Figure 5.9.D. display the complex conductivity spectrum of 3-ML NPLs excited with 400 nm pump wavelength with a fluence of 85 μJ/cm^2 at various pump-probe delays. The initial imaginary conductivity is maximum, due to more number of excitons, and decreases with pump-probe delay implying recombination of excitons. The initial amplitude of the phonon feature at ~2.2 THz in the real part of conductivity immediately after photoexcitation is maximum and diminishes within 30 ps. This most probably indicates hot excitons thermalize to band edge through the exciton-phonon coupling. Similar to what has been observed in NCs (in our previous study), the phonon feature is slightly redshifted on photoexcitation compared to the phonon resonance (2.4 THz) observed in non-photo excited samples. This may also be due to relatively strong exciton-phonon coupling with the softer modes observed along longitudinal and transverse directions in NPLs. Further understanding is required in this direction.

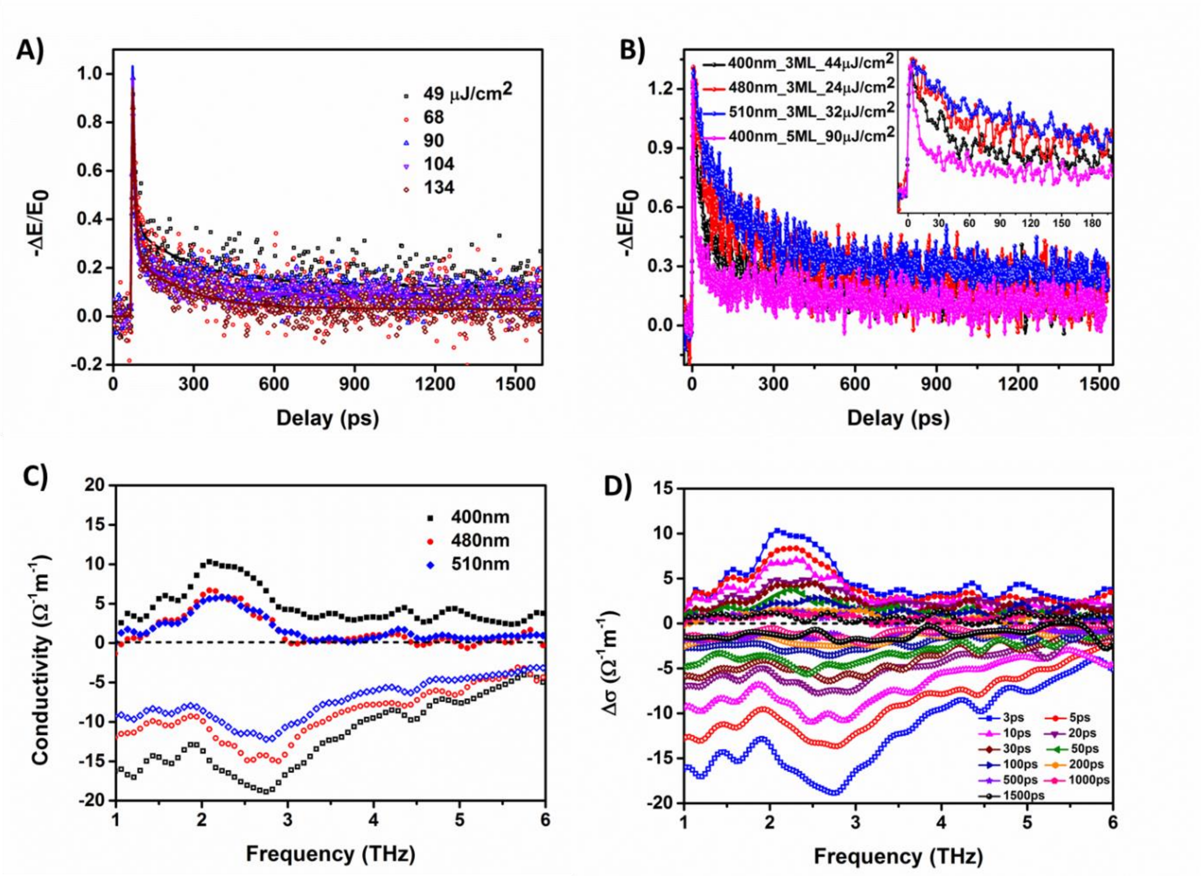

Figure 5.9. A) THz photoconductivity transients obtained for 400 nm pump light at various excitation fluences for 5-ML NPLs. B) Comparison of dynamics at similar peak maxima obtained from 3-ML and 5-ML. C) Photoconductivity spectra of 3-ML NPLs excited with 400, 480 and 510 nm pump wavelengths with fluences of 85, 47 and 75 μJ/cm^2, respectively, after 3 ps pump-probe delay. D) Photoconductivity spectra of 3-ML NPLs excited with 400 nm pump with a fluence of 85 μJ/cm^2 at different pump-probe delays. The real part of conductivity is zero and the imaginary part is negative and finite; excitons being the primary photo-excited species. The short dashed black line indicates zero conductivity.

Table 5.5. Fitting parameters obtained when normalized THz transients fit with Gaussian convoluted multi-exponential function at 400 nm pump pulses for 5-ML NPLs.

Wavelength (nm)	**Fluence (μJ/cm^2)**	**a$_1$**	**τ$_1$ (ps)**	**a$_2$**	**τ$_2$ (ps)**	**a$_3$**	**τ$_3$ (ps)**
	49	0.65 (0.004)	9.6 (0.1)	0.24 (0.001)	221.3 (1.7)	0.13 (0.00)	17000
	68	0.72 (0.003)	9.5 (0.0)	0.25 (0.001)	220.0 (0.0)	0.07 (0.00)	17000

400	90	0.87 (0.003)	8.0 (0.0)	0.15 (0.001)	210.0 (0.0)	0.09 (0.00)	17000
	104	0.80 (0.003)	7.3 (0.0)	0.16 (0.001)	157.9 (1.3)	0.09 (0.00)	17000
	134	0.73 (0.003)	9.8 (0.1)	0.22 (0.001)	183.6 (1.2)	0.03 (0.00)	17000

5.3.4 Peak mobility and diffusion lengths from time-resolved dynamics:

One of the most important parameters which decide the efficiency of the optoelectronic device and photovoltaic cell is the carrier mobility. The mobility can be calculated, from the peak photoconductivity ($\Delta\sigma$) and number of carriers (N) generated, as follows

$$\varphi\mu = {}^{\Delta\sigma}\!/_{\mathrm{Nq}} \qquad (5.3)$$

where q is the elementary charge and $\Delta\sigma$ is related to change in transmission of THz electric field as[48]

$$\Delta\sigma(t_p) = \frac{\varepsilon_0 c}{d}(n_a + n_b)\frac{-\Delta E(t_p)}{E_0(t_p)} \qquad (5.4)$$

where ε_0 is the permittivity of free space, c is the speed of light, d is the thickness of the sample and n_a and n_b are refractive indices of the media on either side of the sample. Here the sample was spin-cast on HDPE, hence n_a=1 (air refractive index) and n_b =1.48 (refractive index of HDPE, measured from our TDS). Finding the exact number of absorbed photons converting into electron-hole pairs is difficult. One would assume every absorbed photon results in one electron-hole pair and one would get number of carriers generated as $N = \varphi 2N_{Ph}$. Unlike cubic NCs, where we had assumed that the photon to free conversion ratio was equal to one ($\varphi = 1$), NPLs are under strong confinement and excitonic contribution may be significant. Hence, the obtained mobilities are effective mobilities ($\varphi\mu$). The number of absorbed photons can be calculated as $N_{Ph} = (F_l(1\text{-}10^{-OD_\lambda}))/\delta.h\nu$ where F_l is the fluence, $1\text{-}10^{-OD_\lambda}$ is the fraction of the pump light absorbed by the sample at a particular wavelength λ, δ is the penetration depth and $h\nu$ is the energy of a single photon of wavelength λ. Depending on the carrier density, varying from 1.4 x 10^{17} to 6.9 x 10^{17} for 400 nm and 5.0 x 10^{15} to 8.6 x 10^{16} for 480 and 510 nm, and initial conductivity, varying from 5.5 to 18.6 S/m for 400 nm and 4 to 12 S/m for 480 and 510 nm, the estimated effective mobilities are plotted in Figure 5.10. Here, the mobilities in case of-3 ML are twice than that of 5-ML, as shown in Figure 5.10.A, which is opposite to the trend expected in the quantum confined system. Similar arguments made above can be applicable here. Since TRTS is able to probe only excited state species generated, irrespective of the size of the NPLs from which they are generated, the higher order stacked NPLs also contribute to mobilities, hence the increased mobilities in 3-ML NPLs, whereas, 5-ML is free from higher order stacked NPLs, strong confinement reduces the mobilities. It is to be noted that the mobilities are one order high when 3-ML NPLs are excited with below band gap photon energies at very low carrier densities, as shown in Figure 5.10.C. Another crucial parameter, diffusion length, can be obtained from the given initial mobility and a weighted average lifetime as $L_D = \sqrt{(\langle\tau\rangle \mu k_B T/q)}$; where $\langle\tau\rangle$ is the average life time and given as $\langle\tau\rangle = \sum f_i \tau_i$, where f_i is the i^{th} decay channel population fraction, μ is the peak mobility obtained from the time-resolved experiments, k_B is the Boltzmann constant, T is temperature and q is the elementary charge.[12,49,50] It is important to have diffusion length greater than the film thickness and absorption depth of the incident photon to effectively collect the charge carriers at electrodes for better performance of the photovoltaic cell. The diffusion lengths, shown in Figure 5.10.B and 5.10.D, are in the range of typical optical absorption depths (few hundred nm in the visible range), which indicates that these NPLs can be used as prospective photovoltaic materials.

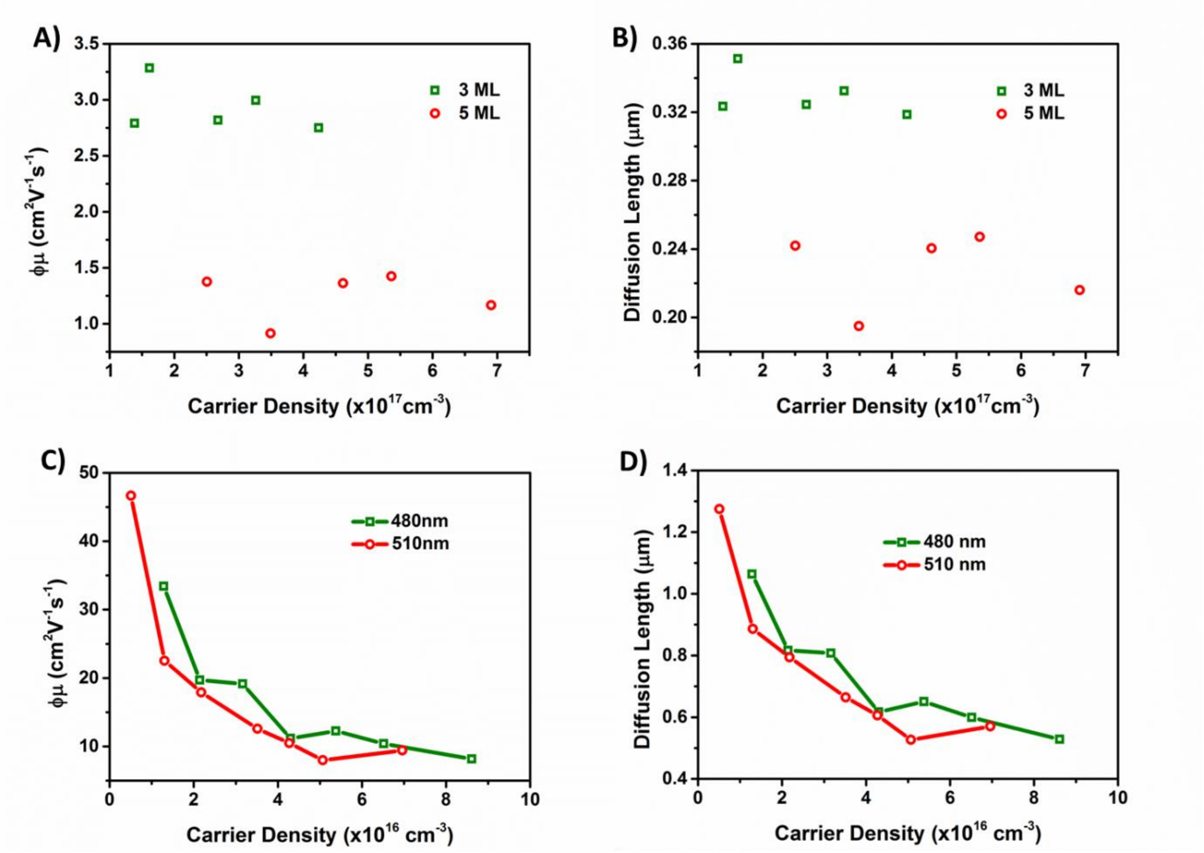

Figure 5.10: Effective mobility and diffusion length of 3-ML and 5-ML NPLs. A) and B) present a comparison of effective mobility and diffusion length of 3 and 5-ML NPLs excited at 400 nm pump pulse, respectively. C) and D) compare the effective mobility and diffusion length obtained when 3-ML film excited below band gap.

5.4 Conclusions:

In conclusions, we have employed time-domain and time-resolved THz spectroscopy along with time-resolved photoluminescence spectroscopy, to elucidate the effect of quantum confinement on phonon modes and carrier dynamics in CsPbBr$_3$ NPLs. The THz absorption spectrum has two peaks. One is independent of confinement and the second one is strongly dependent on confinement. We attribute the former to longitudinal (in-plane) optical phonons and latter to the transverse optical phonons (out-of-plane). The red-shift of the out-of-plane phonons with increasing confinement is due to lattice expansion. Dominant excited species being excitons on photoexcitation, the most of carrier population (>85 %) recombination occur within a few hundred picoseconds as evident from TRTS. Hence, we infer that TRPL could not resolve the dynamics and prompted previous researchers to conclude that the dynamics are independent of the degree of the confinement. Further, strong confinement in NPLs curtails mobilities (1.0-3.0 $cm^2V^{-1}s^{-1}$) and diffusion lengths (0.2-0.36 μm). However, when the NPLs are stacked, the mobilities (> 40 $cm^2V^{-1}s^{-1}$) and diffusion lengths (1 μm) increase drastically. Therefore, we anticipate that these quasi 2D nanoplatelets can serve as promising candidates for prospective light-emitting applications when they are confined and photovoltaic applications when they are stacked.

5.5 References:

(1) Tong, Y.; Ehrat, F.; Vanderlinden, W.; Cardenas-Daw, C.; Stolarczyk, J. K.; Polavarapu, L.; Urban, A. S. *ACS Nano* **2016**, *10*, 10936.
(2) Dou, L.; Wong, A. B.; Yu, Y.; Lai, M.; Kornienko, N.; Eaton, S. W.; Fu, A.; Bischak, C. G.; Ma, J.; Ding, T.; Ginsberg, N. S.; Wang, L.-W.; Alivisatos, A. P.; Yang, P. *Science* **2015**, *349*, 1518.
(3) Weidman, M. C.; Goodman, A. J.; Tisdale, W. A. *Chem. Mater.* **2017**, *29*, 5019.
(4) Bekenstein, Y.; Koscher, B. A.; Eaton, S. W.; Yang, P.; Alivisatos, A. P. *J. Am. Chem. Soc.* **2015**, *137*, 16008.
(5) Akkerman, Q. A.; Motti, S. G.; Srimath Kandada, A. R.; Mosconi, E.; D'Innocenzo, V.; Bertoni, G.; Marras, S.; Kamino, B. A.; Miranda, L.; De Angelis, F.; Petrozza, A.; Prato, M.; Manna, L. *J. Am. Chem. Soc.* **2016**, *138*, 1010.
(6) Si, J.; Liu, Y.; He, Z.; Du, H.; Du, K.; Chen, D.; Li, J.; Xu, M.; Tian, H.; He, H.; Di, D.; Lin, C.; Cheng, Y.; Wang, J.; Jin, Y. *ACS Nano* **2017**, *11*, 11100.
(7) Sichert, J. A.; Tong, Y.; Mutz, N.; Vollmer, M.; Fischer, S.; Milowska, K. Z.; García Cortadella, R.; Nickel, B.; Cardenas-Daw, C.; Stolarczyk, J. K.; Urban, A. S.; Feldmann, J. *Nano Lett.* **2015**, *15*, 6521.
(8) Weidman, M. C.; Seitz, M.; Stranks, S. D.; Tisdale, W. A. *ACS Nano* **2016**, *10*, 7830.
(9) Quan, L. N.; Yuan, M.; Comin, R.; Voznyy, O.; Beauregard, E. M.; Hoogland, S.; Buin, A.; Kirmani, A. R.; Zhao, K.; Amassian, A. *J. Am. Chem. Soc.* **2016**, *138*, 2649.
(10) Brandt, R. E.; Stevanović, V.; Ginley, D. S.; Buonassisi, T. *MRS Comm.* **2015**, *5*, 265.
(11) Huang, H.; Bodnarchuk, M. I.; Kershaw, S. V.; Kovalenko, M. V.; Rogach, A. L. *ACS Energy Lett.* **2017**, *2*, 2071.
(12) Yettapu, G. R.; Talukdar, D.; Sarkar, S.; Swarnkar, A.; Nag, A.; Ghosh, P.; Mandal, P. *Nano Lett.* **2016**, *16*, 4838.
(13) Swarnkar, A.; Chulliyil, R.; Ravi, V. K.; Irfanullah, M.; Chowdhury, A.; Nag, A. *Angew. Chem. Int. Ed.* **2015**, *54*, 15424.
(14) Yakunin, S.; Protesescu, L.; Krieg, F.; Bodnarchuk, M. I.; Nedelcu, G.; Humer, M.; De Luca, G.; Fiebig, M.; Heiss, W.; Kovalenko, M. V. *Nat. Commun.* **2015**, *6*.
(15) Protesescu, L.; Yakunin, S.; Bodnarchuk, M. I.; Krieg, F.; Caputo, R.; Hendon, C. H.; Yang, R. X.; Walsh, A.; Kovalenko, M. V. *Nano Lett.* **2015**, *15*, 3692.
(16) Koscher, B. A.; Swabeck, J. K.; Bronstein, N. D.; Alivisatos, A. P. *J. Am. Chem. Soc* **2017**, *139*, 6566.
(17) Fox, M. *Optical Properties of Solids; 2nd ed.* Oxford University Press: Oxford, UK, 2001.
(18) Zhang, Q.; Su, R.; Liu, X.; Xing, J.; Sum Tze, C.; Xiong, Q. *Adv. Funct. Mater.* **2016**, *26*, 6238.

(19) Han, C.; Li, C.; Zang, Z.; Wang, M.; Sun, K.; Tang, X.; Du, J. *Photon. Res.* **2017**, *5*, 473.
(20) Shamsi, J.; Rastogi, P.; Caligiuri, V.; Abdelhady, A. L.; Spirito, D.; Manna, L.; Krahne, R. *ACS Nano* **2017**, *11*, 10206.
(21) Yang, Z.; Wang, M.; Qiu, H.; Yao, X.; Lao, X.; Xu, S.; Lin, Z.; Sun, L.; Shao, J. *Adv. Funct. Mater.* **2018**, *28*, 1705908.
(22) Hu, X.; Wang, X.; Fan, P.; Li, Y.; Zhang, X.; Liu, Q.; Zheng, W.; Xu, G.; Wang, X.; Zhu, X.; Pan, A. *Nano Lett.* **2018**, *18*, 3024.
(23) Li, J.; Luo, L.; Huang, H.; Ma, C.; Ye, Z.; Zeng, J.; He, H. *J. Phys. Chem. Lett.***2017**, *8*, 1161.
(24) Zhao, J.; Liu, M.; Fang, L.; Jiang, S.; Zhou, J.; Ding, H.; Huang, H.; Wen, W.; Luo, Z.; Zhang, Q.; Wang, X.; Gao, C. *J. Phys. Chem. Lett.* **2017**, *8*, 3115.
(25) Němec, H.; Kužel, P.; Sundström, V. *J. Photochem. Photobiol. A: Chemistry* **2010**, *215*, 123.
(26) Sarkar, S.; Ravi, V. K.; Banerjee, S.; Yettapu, G. R.; Markad, G. B.; Nag, A.; Mandal, P. *Nano Lett.* **2017**, *17*, 5402.
(27) Ulbricht, R.; Hendry, E.; Shan, J.; Heinz, T. F.; Bonn, M. *Rev.Mod. Phys.* **2011**, *83*, 543.
(28) loyd-Hughes, J.; Jeon, T.-I. *J. Infrared Millim. Terahertz Waves* **2012**, *33*, 871.
(29) Johnston, M. B.; Herz, L. M. *Acc. Chem. Res.* **2016**, *49*, 146.
(30) Schmuttenmaer, C. A. *Chem. Rev.* **2004**, *104*, 1759.
(31) Wright, A. D.; Verdi, C.; Milot, R. L.; Eperon, G. E.; Pérez-Osorio, M. A.; Snaith, H. J.; Giustino, F.; Johnston, M. B.; Herz, L. M. *Nat. commun.* **2016**, *7*, 11755.
(32) Kim, H.; Hunger, J.; Cánovas, E.; Karakus, M.; Mics, Z.; Grechko, M.; Turchinovich, D.; Parekh, S. H.; Bonn, M. *Nat. Commun.* **2017**, *8*, 687.
(33) Wehrenfennig, C.; Liu, M.; Snaith, H. J.; Johnston, M. B.; Herz, L. M. *J. Phys. Chem. Lett.***2014**, *5*, 1300.
(34) Karakus, M.; Jensen, S. A.; D'Angelo, F.; Turchinovich, D.; Bonn, M.; Cánovas, E. *J. Phys. Chem. Lett.* **2015**, *6*, 4991.
(35) Di Stasio, F.; Imran, M.; Akkerman, Q. A.; Prato, M.; Manna, L.; Krahne, R. *J. Phys. Chem. Lett.* **2017**, *8*, 2725.
(36) De Roo, J.; Ibáñez, M.; Geiregat, P.; Nedelcu, G.; Walravens, W.; Maes, J.; Martins, J. C.; Van Driessche, I.; Kovalenko, M. V.; Hens, Z. *ACS Nano* **2016**, *10*, 2071.
(37) Wang, Y.; Li, X.; Sreejith, S.; Cao, F.; Wang, Z.; Stuparu Mihaiela, C.; Zeng, H.; Sun, H. *Adv. Mater.* **2016**, *28*, 10637.
(38) Mizusaki, J.; Arai, K.; Fueki, K. *Solid State Ion.* **1983**, *11*, 203.
(39) Hwang, Y.-N.; Park, S.-H.; Kim, D. *Phys. Rev. B* **1999**, *59*, 7285.
(40) Hwang, Y.-N.; Shin, S.; Park, H. L.; Park, S.-H.; Kim, U.; Jeong, H. S.; Shin, E.-j.; Kim, D. *Phys. Rev. B* **1996**, *54*, 15120.
(41) Sigle, D. O.; Hugall, J. T.; Ithurria, S.; Dubertret, B.; Baumberg, J. J. *Phys. Rev. Lett.* **2014**, *113*, 087402.
(42) Royo, M.; Climente, J. I.; Movilla, J. L.; Planelles, J. *J. Phys.Condens. Matter* **2010**, *23*, 015301.
(43) Beard, M. C.; Turner, G. M.; Schmuttenmaer, C. A. *Nano Lett.* **2002**, *2*, 983.
(44) Wang, F.; Shan, J.; Islam, M. A.; Herman, I. P.; Bonn, M.; Heinz, T. F. *Nat. Mater.***2006**, *5*, 861.
(45) Pijpers, J. J. H.; Milder, M. T. W.; Delerue, C.; Bonn, M. *J. Phys. Chem. C* **2010**, *114*, 6318.
(46) Dakovski, G. L.; Lan, S.; Xia, C.; Shan, J. *J. Phys. Chem. C* **2007**, *111*, 5904.
(47) Efros, A. L.; Rosen, M. *Ann. Rev. Mater. Sci.* **2000**, *30*, 475.
(48) Nienhuys, H.-K.; Sundström, V. *Phys. Rev. B* **2005**, *71*, 235110.

(49) Lakowicz, J. R. *Principles of Fluorescence Spectroscopy*; 3 ed.; Springer US, 2006.
(50) Guglietta, G. W.; Diroll, B. T.; Gaulding, E. A.; Fordham, J. L.; Li, S.; Murray, C. B.; Baxter, J. B. *ACS Nano* **2015**, *9*, 1820.

Chapter 6

Summary and Outlook

Ultra-broadband Time-domain and Time-resolved THz spectroscopic techniques were employed to probe the origin of phonon modes and the nature of the carrier dynamics with sub-picosecond temporal resolution in $CsPbBr_3$ perovskite cubic nanocrystals and nanoplatelets. We were able to determine the different transport properties, such as carrier mobilities and diffusion lengths in these systems. The broadband THz probe was generated by using air as an active medium and detected by air biased coherent detection (ABCD) method.

Using time-domain THz spectroscopy, we observed that the phonon absorption band has a peak at ~3.4 THz and assigned its origin from first principles DFT calculations. The major contribution comes from an anti-symmetric apical Pb-Br stretching mode and one in-plane Br-Pb-Br bending mode. Our Time-resolved THz spectroscopy study of the photoexcited carrier dynamics reveals that three-channel recombination mechanisms are present. Auger recombination, bimolecular electron-hole recombination, and monomolecular trap-assisted recombination with respective time constants of ~25 ps, 150-300 ps, and >15 ns, contribute to the overall carrier recombination. Inefficient trap-assisted recombination results in high charge carrier mobilities (~ 4500 $cm^2V^{-1}s^{-1}$) and larger diffusion lengths (> 9.2 μm). From early dynamics, we found the time constant for the dissociation of exciton to free carrier to be 5-6 ps. A strong exciton-phonon coupling with softer modes redshifts the phonon resonance in the photoexcited NCs. These studies clearly indicate that $CsPbBr_3$ NCs are a promising material for optoelectronic and photovoltaic applications.

We extended our study to probe dynamics in $CsPbBr_3$ NC film because many optoelectronic and photovoltaic devices use film as an active layer. In the film, carriers encounter grain boundaries, and thereby alter the dynamics and transport properties. Here, we studied kinetics under one-photon absorption (OPA) and two-photon absorption (TPA) pumping. Carrier recombination kinetics in TPA is slightly slower compared to that in OPA. We attribute this difference in carrier dynamics to the presence of different initial excited states. Further, we observe the presence of large to intermediate polaron formation. This explains the reduction in mobility and diffusion length across the film by more than an order compared to those within individual NCs. The observed transport properties are similar to those reported for other hybrid organic-inorganic lead halide perovskites (single crystal and polycrystalline film) used as active material in high-efficiency devices. This observation is certainly encouraging and indicates that these $CsPbBr_3$ nanocrystal films also can be a potential candidate in prospective photovoltaic and optoelectronic devices.

The size of our nanocubes was ~11 nm, which are in a weak confinement regime. Further, we extended our study to probe carrier dynamics in $CsPbBr_3$ nanoplatelets (NPLs), which are in strong quantum confinement regime due to their thickness being much smaller than the exciton Bohr radius. The primary photoexcited species being excitons, the carrier recombination is faster in NPLs compared to that in colloidal dispersion and film. The THz-TDS absorption spectrum has two prominent features and we attribute them to in-plane and out-of-plane lattice vibrations. The one at ~4.2 THz is independent of the thickness of the NPLs and is attributed to the in-plane vibrations. On the other hand, the peak at ~ 2.5 THz varies with the thickness of the NPLs, and we attribute this feature to the out-of-plane vibrations. The observed redshift of the phonon resonance with increasing confinement is due to the lattice expansion. Strong confinement present in these NPLs also curtails the carrier mobilities and diffusion lengths. However, these NPLs are prone to stacking (self-assembling) in a film. The stacked forms behave like bulk or larger (than exciton Bohr diameter) NCs and exhibit high mobilities and diffusion lengths. These studies clearly indicate that strongly confined NPLs can be used in light emitting applications in the blue region of the spectrum. However, by varying the distance between NPLs, one can tune the transport properties and hence may be suitable for optoelectronic applications.

Overall, the nanocubes whose size is in ~11 nm experience weak to no confinement, and hence exhibit bulk-like carrier dynamics. Strong confinement present in NPLs makes carriers undergo fast recombination. The transport properties in nanocubes film reduce more than an order. In the case of single nanocube, the polaron, whose size is 5-6 nm, is delocalized over a major portion of the NC leading to higher effective transport properties. On the contrary, in the film, the large and heavy polaron has to travel across the film overcoming the barrier arising from the grain boundaries, inter-NC contact and length of the capping ligand. The overall summary is given in table 6.1.

Although we have shown that trap-states play a minor role in impeding the transport properties, one needs to carry out the work further to understand the reduction in mobilities and diffusion lengths in the $CsPbBr_3$ NC film. One way to improve the efficiency is to replace the insulating organic capping ligands with shorter chain capping ligands. Further studies are required to look at the dynamics at low temperature, where lattice vibrations are frozen and the electron-phonon scattering is reduced. It will be interesting to look at the dynamics in doped NCs, where doping may alter the soft ionic nature of the lattice. The reduced intraband energy gap also indicates that these NCs can be potential candidates for intraband photodetectors in the far infrared region.

Table 6.1. Comparison of carrier dynamics, effect of confinement, nature of the charge carriers, mobilities and diffusion lengths for the three systems ($CsPbBr_3$ colloidal NCs, film and nanoplatelets) studied in this thesis.

System	**Dynamics**	**Effect of confinement**	**Nature of the primary charge carriers**	**Mobility ($cm^2V^{-1}s^{-1}$)**	**Diffusion length (μm)**
Colloidal $CsPbBr_3$ NCs	Slow	Weak	Mostly free carriers	~4500	9.2
$CsPbBr_3$ Film	Relatively fast compared to colloidal NCs	No	Free carriers in the form of polarons	~ 55-180	1
$CsPbBr_3$ Nanoplatelets	Very fast	Strong	Excitons	1-3	0.2-0.36

IISER PUNE

Y G Reddy <ygreddy@students.iiserpune.ac.in>

Request #9131-7978184 Resolved (Reusing the figure in my Thesis)

1 message

---

support@services.acs.org <support@services.acs.org> Sat, Jan 13, 2018 at 1:46 AM
Reply-To: support@services.acs.org
To: "ygreddy@students.iiserpune.ac.in" <ygreddy@students.iiserpune.ac.in>

ACS
Chemistry for Life®

Click here if you have difficulty reading this email >>

Dear Dr.Reddy,

Thank you for contacting ACS Publications Support.

Your permission request is granted and there is no fee for this reuse. In your planned reuse, you must cite the ACS article as the source, add this direct link http://pubs.acs.org/doi/full/10.1021/nl5048779?src=recsys and include a notice to readers that further permissions related to the material excerpted should be directed to the ACS.

I hope this is helpful and if you need further assistance, please feel free to contact me.

Sincerely,

Ashley Gibson

ACS Publications

Customer Services & Information

Website: https://help.acs.org

Your help request has been resolved. If you have further issues regarding this matter, please let us know by responding to this email. Please note that this request will auto-close in 14 days. If you need to contact us after 14 days regarding this matter please submit a new help request and refer to this help request number.

How are we doing? Let us know!
Please click on your selection below to begin our two-question survey.

Based on this support interaction, how satisfied were you with the help provided?

Not at all satisfied *Completely satisfied*

0	1	2	3	4	5	6	7	8	9	10
○	○	○	○	○	○	○	○	○	○	○

E-mail Information:

Attachments

cc

Request Information:

Request # 9131-7978184
Date Created 1/12/2018 11:28 AM EST
Summary Reusing the figure in my Thesis

Details

Dear ACS,

I want to use one of the figure from the paper titled as "Nanocrystals of Cesium Lead Halide Perovskites (CsPbX3, X = Cl, Br, and I): Novel Optoelectronic Materials Showing Bright Emission with Wide Color Gamut"
Regarding the figure which I want to use in my thesis given as follows

Link to the Paper:
"http://pubs.acs.org/doi/full/10.1021/nl5048779?src=recsys "

Figure Details:
No. of figures : 1
Figure number in the paper: Figure 2

Description where to use the figure:

I want to use the figure in my thesis introduction chapter, where I want write why perovskites are important?. In that context I want to mention that Perovskite ,especially CsPbX3, is highly luminiscent and PL QY yield is >50% and narrow bandwidth. Further, PL can be tuned across visible range hence CsPbBr3 NCs are more suitable for applications such as light emitting diodes and lasers and so on.

Further, this is important because I exclusively worked on CsPbBr3 Nanocrystals during my Ph.D. and relevant paper I published recently in ACS journals and the link given to my paper as "http://pubs.acs.org/doi/abs/10.1021/acs.nanolett.6b01168".

In this regard I want to take figure to tell the importance of CsPbBr3 NCs. However, I am unable to get copyrights and permissions instead it is directing me to other page where it is suggesting that whether the article is editor's or author's choice. I found it as Editor's choice and mentioned that one can use its content for non-commercial use. So I would be expecting that I can use the figure in my thesis without taking any special copyrights. However, please clarify me at the earliest whether I can use figure without any special copyrights and permissions, otherwise suggest me what kind of permissions should I take.

Thanking you,

Yettapu Gurivi Reddy,
IISER-Pune,
India-411008.

--
Y G Reddy,
C/O Dr. Pankaj k. Mandal,
IISER Pune,
Pune,
Maharashtra. Pin-411008.

To update or check the status of this request:
Click here to access this request online.

Copyright Clearance Center RightsLink®

Home Account Info Help

SPRINGER NATURE

Title: Exciton polarizability in semiconductor nanocrystals
Author: Feng Wang, Jie Shan, Mohammad A. Islam, Irving P. Herman, Mischa Bonn et al.
Publication: Nature Materials
Publisher: Springer Nature
Date: Oct 8, 2006

Logged in as:
Gurivi Reddy Yettapu
IISER-Pune
Account #:
3001235695

LOGOUT

Review Order

Please review the order details and the associated terms and conditions.

No royalties will be charged for this reuse request although you are required to obtain a license and comply with the license terms and conditions. To obtain the license, click the Accept button below.

Licensed Content Publisher	Springer Nature
Licensed Content Publication	Nature Materials
Licensed Content Title	Exciton polarizability in semiconductor nanocrystals
Licensed Content Author	Feng Wang, Jie Shan, Mohammad A. Islam, Irving P. Herman, Mischa Bonn et al.
Licensed Content Date	Oct 8, 2006
Licensed Content Volume	5
Licensed Content Issue	11
Type of Use	Thesis/Dissertation
Requestor type	non-commercial (non-profit)
Format	print and electronic
Portion	figures/tables/illustrations
Number of figures/tables/illustrations	1
High-res required	no
Will you be translating?	no
Circulation/distribution	<501
Author of this Springer Nature content	no
Title	Ultrafast Carrier Dynamics in CsPbBr3 Perovskite Nano-cubes-n-platelets: Time-resolved TeraHertz Spectroscopy Study
Instructor name	Dr. Pankaj Mandal
Institution name	IISER-Pune
Expected presentation date	Aug 2018
Portions	Figure 2 Spectral dependence of the change in the real (χ s) and imaginary part (χ s) of the photoinduced sheet susceptibility of the sample.
Requestor Location	IISER-Pune IISER-Pune Dr. Homi Bhabha Road, Pashan Maharashtra Pune, 411008 India Attn: IISER-Pune
Total	0.00 USD

Edit Order Details
Edit Your Work Details
Edit Requestor Location This location may be used to determine your tax liability.

☑ I agree to these terms and conditions.

☐ I understand this license is for reuse only and that no content is provided.

Customer Code (if supplied) ☐ APPLY

BACK DECLINE ACCEPT

Please click accept only once.

Copyright Clearance Center RightsLink®

Home Account Info Help

SPRINGER NATURE

Title: The surface science of nanocrystals
Author: Michael A. Boles, Daishun Ling, Taeghwan Hyeon, Dmitri V. Talapin
Publication: Nature Materials
Publisher: Springer Nature
Date: Jan 22, 2016

Logged in as:
Gurivi Reddy Yettapu
IISER-Pune
Account #:
3001235695

LOGOUT

Review Order

Please review the order details and the associated terms and conditions.

No royalties will be charged for this reuse request although you are required to obtain a license and comply with the license terms and conditions. To obtain the license, click the Accept button below.

Licensed Content Publisher	Springer Nature
Licensed Content Publication	Nature Materials
Licensed Content Title	The surface science of nanocrystals
Licensed Content Author	Michael A. Boles, Daishun Ling, Taeghwan Hyeon, Dmitri V. Talapin
Licensed Content Date	Jan 22, 2016
Licensed Content Volume	15
Licensed Content Issue	2
Type of Use	Thesis/Dissertation
Requestor type	non-commercial (non-profit)
Format	print and electronic
Portion	figures/tables/illustrations
Number of figures/tables/illustrations	1
High-res required	no
Will you be translating?	no
Circulation/distribution	<501
Author of this Springer Nature content	no
Title	Ultrafast Carrier Dynamics in CsPbBr3 Perovskite Nano-cubes-n-platelets: Time-resolved TeraHertz Spectroscopy Study
Instructor name	Dr. Pankaj Mandal
Institution name	IISER-Pune
Expected presentation date	Aug 2018
Portions	Figure 3: Effect of ligands on nanocrystal surface states
Requestor Location	IISER-Pune IISER-Pune Dr. Homi Bhabha Road, Pashan Maharashtra Pune, 411008 India Attn: IISER-Pune
Total	0.00 USD

Edit Order Details
Edit Your Work Details
Edit Requestor Location This location may be used to determine your tax liability.

☑ I agree to these terms and conditions.

☐ I understand this license is for reuse only and that no content is provided.

Customer Code (if supplied)	☐	APPLY

BACK DECLINE ACCEPT

Please click accept only once.

Copyright Clearance Center RightsLink®

Home | Create Account | Help

ACS Publications
Most Trusted. Most Cited. Most Read.

Title: Terahertz Conductivity within Colloidal CsPbBr3 Perovskite Nanocrystals: Remarkably High Carrier Mobilities and Large Diffusion Lengths

Author: Gurivi Reddy Yettapu, Debnath Talukdar, Sohini Sarkar, et al

Publication: Nano Letters

Publisher: American Chemical Society

Date: Aug 1, 2016

LOGIN

If you're a copyright.com user, you can login to RightsLink using your copyright.com credentials. Already **a RightsLink user** or want to learn more?

PERMISSION/LICENSE IS GRANTED FOR YOUR ORDER AT NO CHARGE

This type of permission/license, instead of the standard Terms & Conditions, is sent to you because no fee is being charged for your order. Please note the following:

- Permission is granted for your request in both print and electronic formats, and translations.
- If figures and/or tables were requested, they may be adapted or used in part.
- Please print this page for your records and send a copy of it to your publisher/graduate school.
- Appropriate credit for the requested material should be given as follows: "Reprinted (adapted) with permission from (COMPLETE REFERENCE CITATION). Copyright (YEAR) American Chemical Society." Insert appropriate information in place of the capitalized words.
- One-time permission is granted only for the use specified in your request. No additional uses are granted (such as derivative works or other editions). For any other uses, please submit a new request.

BACK | CLOSE WINDOW